1

PM-1 3½"x4" PHOTOGRAPHIC MICROCOPY TARGET
NBS 1010a ANSI/ISO #2 EQUIVALENT
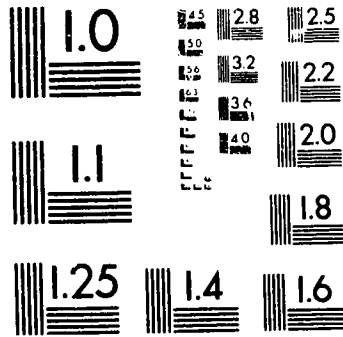
1.0

1.1

1.25

2.8   2.5

3.2   2.2

3.6

4.0   2.0

1.8

1.4   1.6

NOTICE

The quality of this microform is heavily dependent upon the quality of the original thesis submitted for microfilming. Every effort has been made to ensure the highest quality of reproduction possible.

If pages are missing, contact the university which granted the degree.

Some pages may have indistinct print especially if the original pages were typed with a poor typewriter ribbon or if the university sent us an inferior photocopy.

Reproduction in full or in part of this microform is governed by the Canadian Copyright Act, R.S.C. 1970, c. C-30, and subsequent amendments.

AVIS

La qualite de cette microforme dépend grandement de la qualité de la thèse soumise au microfilmage. Nous avons tout fait pour assurer une qualité supérieure de reproduction.

S'il manque des pages, veuillez communiquer avec l'université qui a conféré le grade.

La qualité d'impression de certaines pages peut laisser à désirer, surtout si les pages originales ont été dactylographiées à l'aide d'un ruban usé ou si l'université nous a fait parvenir une photocopie de qualité inférieure.

La reproduction, même partielle, de cette microforme est soumise à la Loi canadienne sur le droit d'auteur, SRC 1970, c. C-30, et ses amendements subséquents.

Canada

UNIVERSITY OF ALBERTA

Multi-Proton Emission in Photon Induced Reactions on ^{12}C

BY

EVAN D. J. HACKETT

©

A thesis
submitted to the Faculty of Graduate Studies and Research
in partial fulfillment of the requirements for the degree of

DOCTOR OF PHILOSOPHY

IN

NUCLEAR PHYSICS

DEPARTMENT OF PHYSICS

EDMONTON, ALBERTA

SPRING 1995

Your file   Votre référence

Our file   Notre référence

ISBN   0-612-01698-6

Canadä

UNIVERSITY OF ALBERTA

RELEASE FORM

NAME OF THE AUTHOR : Evan David Joseph Hackett

TITLE OF THE THESIS : Multi-Proton Emission in Photon Induced Reactions on ^{12}C

DEGREE : Doctor of Philosophy

YEAR THIS DEGREE GRANTED : 1995

Permission is hereby granted to the University of Alberta Library to reproduce single copies of this thesis and to lend or sell such copies for private, scholary or scientific research purposes only.

The author reserves all other publication and other rights in association with the copyright in the thesis, and except as hereinbefore provided neither the thesis nor any substantial portion thereof may be printed or otherwise reproduced in any material from whatever without the author's prior written permission.
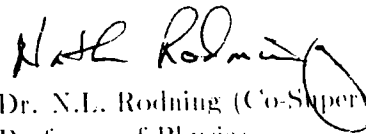
Centre for Subatomic Research,
University of Alberta,
Edmonton, Alberta.
T6G 2N5

Date : April 20th, 199э
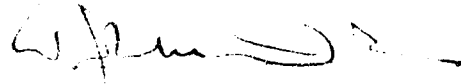
UNIVERSITY OF ALBERTA

FACULTY OF GRADUATE STUDIES AND RESEARCH
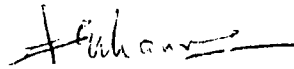
The undersigned certify that they have read, and recommend to the Faculty of Graduate Studies and Research for acceptance, a thesis entitled *Multi-Proton Emission in Photon Induced Reactions on* ^{12}C submitted by Evan D. J. Hackett in partial fulfillment of the requirements for the degree of DOCTOR OF PHILOSOPHY in nuclear physics.
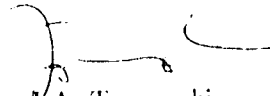
Dr. N.L. Rodning (Co-Supervisor)
Professor of Physics
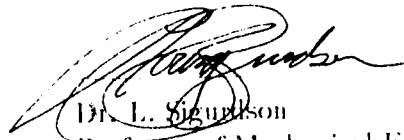
Dr. W.J. McDonald (Co-Supervisor)
Professor of Physics
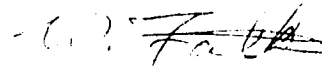
Dr. F.C. Khanna
Professor of Physics

Dr. J.A. Tuszynski
Professor of Physics

Dr. L. Sigurdson
Professor of Mechanical Engineering

Dr. W.R. Falk (External Examiner)
Professor of Physics
University of Manitoba

Date : April 5, '95

Abstract

Differential and total cross sections for inclusive $^{12}C(\gamma,pp)X$ reactions have been measured for tagged photons in the range $187\,\text{MeV} < E_\gamma < 227\,\text{MeV}$, using the Saskatchewan-Alberta Large Acceptance Detector. The large angular acceptance of the detector allowed the first measurement of non-coplanar pp emission. The minimum proton energy detectable was 28 MeV at $\theta = 90°$. The cross sections obtained are compared to the calculation of Carrasco et al. [Ca94]. Reasonable agreement is obtained for the shapes of the cross sections but the calculated total cross section is 3.9 times larger than the data. Cuts are applied in an attempt to isolate the different mechanisms contributing to the inclusive $^{12}C(\gamma,pp)X$ cross section. The expected contribution from quasi-free p-p absorption is found to be suppressed.

ACKNOWLEDGEMENTS

Contents

List of Tables

List of Figures

Chapter 1

Introduction

1.1 Motivation

The photon is well suited to the investigation of nuclear structure. The theory of electro-magnetic interactions is well understood. Compared to hadronic interactions, photonuclear reaction cross sections are small, approximately 1/100 of similar hadronic reactions. Although this makes photonuclear reactions difficult to observe, it can also be an advantage. Whereas a 160 MeV pion would have a mean free path of $\lambda \simeq 0.5$ fermi in nuclear matter [EK80], a 300 MeV photon has $\lambda \simeq 150$ fermi [Jo93] . The pion is therefore absorbed quickly near the surface of a typical nucleus while photons illuminate the nuclear volume uniformly even for the largest nuclei (9 fermi in radius). The photon can therefore probe deeply into the nucleus but produces very small reaction cross sections. Recent advances in accelerators and detectors have greatly increased the possibility for the study of photonuclear cross sections.

A new generation of high duty factor accelerators has begun to come on line which greatly increase the usable photon flux. Pulse stretcher rings can be used to boost the typical 1% duty factor of an electron Linac up to almost 100%. Random background and detector dead times are thereby reduced by spreading the photon flux over time. Early photonuclear experiments using bremsstrahlung beams suffered from both the difficulty of determining the beam flux and the lack of a well defined beam energy. The advent of photon taggers in the late 1970's provided a precise energy for the incident

1

photon beam as well as a reliable flux measurement for normalization. Finally, the last few years has seen the emergence of large solid angle detectors with close to 4π coverage. The Saskatchewan-Alberta Large Acceptance Detector (SALAD) used in this experiment provides a geometric acceptance of 95% with reasonable detector thresholds. It is described in detail in section 2.4. Cross sections as small as a few μb can be measured for a large range of angles. Large acceptance detectors also make possible coincidence experiments which provide the exclusive data needed to constrain theoretical models of photonuclear interactions.

Since the 1950's, theorists have tried to extract information on nuclear structure and interactions inside the nucleus from inclusive (γ,N) and (γ,π) experiments. Unfortunately it is difficult to separate contributions from different reaction mechanisms and the distortions of final state interactions without more experimental information. Coincidence measurements of $(\gamma,2N)$ and $(\gamma,\pi N)$ reactions on nuclei would help separate these reaction channels and determine their theoretical importance.

Early on, the photoemission of nucleons was recognized as a potential probe of the short range nucleon-nucleon potential. If a single nucleon absorbs a photon, the energy momentum mismatch places the nucleon far off-shell. Consequently the off-shell nucleon must interact with other nucleons quickly to share the photon's energy. For a 200 MeV photon incident on a nucleon at rest, the momentum mismatch is roughly 450 MeV/c. The uncertainty principle gives $\Delta x \simeq 2\hbar/\Delta p = 0.9$ fermi as the range of the off-shell nucleon. This matches the typical inter-nucleon spacing in nuclear matter; hence only neighbouring nucleons at very short distances are selected. These correlated nucleon pairs provide information on the short range N-N potential which is not understood as well as the long range, one pion exchange potential (OPE). Only with the recent advances in accelerators and detectors can such $(\gamma,2N)$ experiments be performed with reasonable statistical accuracy.

1.2 Early Work on Photon Absorption in Nuclei

Early interest in photon induced reactions on nuclei centred around the description of the collective nuclear excitations of the giant dipole resonance. As beam energies in-

creased nucleon photoemission and photopion production became tools to study nuclear structure.

1.2.1 Nucleon Photoemission

The deuteron, as the only two-nucleon bound state, has long been used as a testing ground for nucleon-nucleon potential models. As data at higher photon energies become available, theorists adapted their simple models to include contributions from meson exchange currents and nucleon resonances such as the $\Delta(1232)$ [Ar90]. Due to its small binding energy, the average nucleon-nucleon separation in the deuteron is roughly twice the mean N-N separation in larger nuclei. To probe the short range N-N potential then, it is necessary to abandon the simplicity of the deuteron f : more complex nuclei.

Building on their knowledge of deuteron photodisintegration, theorists attempted to describe photon absorption in heavier nuclei as a sum of quasi-free two nucleon absorption. The quasi - deuteron model of Levinger [Le51] works surprisingly well given the difference in nucleon densities for deuterium compared to nuclear matter. Only neutron- proton pairs are considered since p-p and n-n pairs have no electric dipole moment. The total cross section for $A(\gamma,pn)A - 2$ is calculated as,

$$\sigma(\gamma,pn) = L \frac{NZ}{A} \sigma_d, \tag{1.1}$$

where σ_d is the deuteron cross section and the Levinger constant, L, is a parameter which accounts for differences in nuclear density. Typical values for medium nuclei range from $L = 3$ to $L = 4$. The quasi-deuteron model gives a good description of photoemission of protons for a wide range of A and photon energy, including the region of the Δ resonance. This success is in some sense disappointing. The strength of the quasi-free dipole absorption swamps weaker processes which are more sensitive to nuclear structure effects.
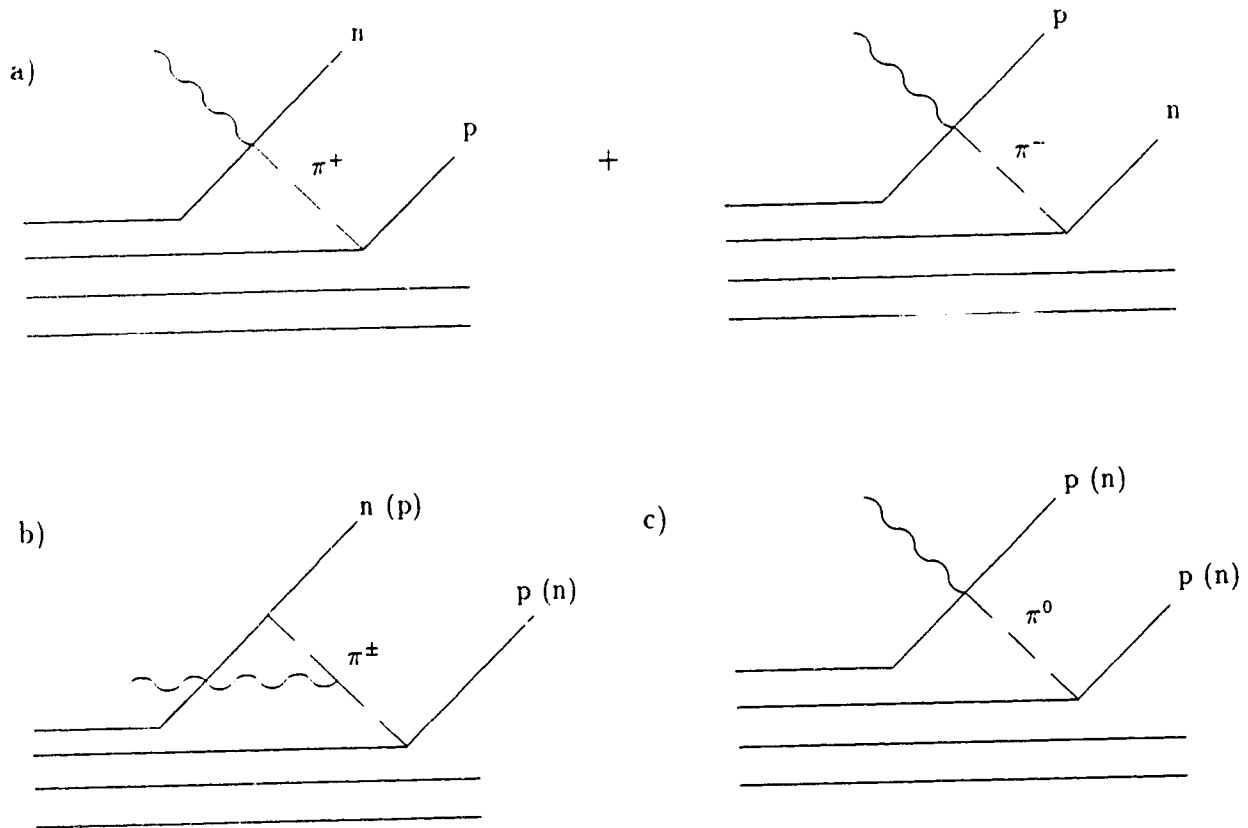
Figure 1.1: Contributions to photon absorption on N-N pairs.

1.3 Current Status

1.3.1 Multi-Nucleon Photoemission

Most $A(\gamma,NN)X$ experiments have concentrated on $A(\gamma,np)X$ pairs and a quasi-deuteron model description. Cross sections for $A(\gamma,pp)X$ are roughly an order of magnitude smaller. This is explained in the quasi-deuteron framework by the fact that a proton-proton pair has no electric dipole moment. Therefore, absorption of the photon must proceed via weaker quadrupole absorption or some more complex mechanism.

An equivalent explanation is given in terms of meson exchange currents. All the diagrams of figure 1.1 contribute to the absorption of photons on n-p pairs but only the weaker neutral pion exchange diagrams (c), contribute to photon absorption by p-p or n-n pairs.

Little data exist for $A(\gamma,pp)X$ reactions near the Δ resonance. Kanazawa [Ka87],

4

measured $A(\gamma, px)X$ w' $x = \pi$, p, n for ^1H, ^2H, ^9Be, ^{12}C and ^{16}O targets. Tagged photons in the range $\vdots$ MeV $< E_\gamma < 420$ MeV were used. Arends [Ar80] also measured $A(\gamma, px)X$ with $x = \pi$, p, n but only for ^{12}C. Tagged photons in the range 135 MeV $< E_\gamma < 455$ MeV, were used.

Since dipole absorption is not allowed for $A(\gamma, pp)X$, the following mechanisms may be evident:

1. Quadrupole and higher order multipole absorption,

2. $A(\gamma, np)X$ followed by nucleon-nucleon rescattering,

3. Real pion production followed by π absorption on a 2N pair.

The first of these, quadrupole absorption, should be at least an order of magnitude weaker than the electric dipole strength. Estimates of the ratio of $\sigma(pp)/\sigma(np)$ in coplanar kinematics run from 0.04 to 0.15 in the Δ region [Ar80, Ka87] hence quadrupole absorption may provide at least some of the needed p-p strength. Angular correlation information should aid in identifying quadrupole absorption.

Rescattering is a serious concern. Both the pion and nucleon interact strongly with nucleons. N-N scattering data predict a mean free path of $\lambda_N \simeq 1$ fermi for nucleons inside a nucleus. This has long been a concern for $A(\pi, NN)X$ reactions [We90], but recent experiments [Sc80, Na81, Fa81] have established that nucleon rescattering effects are much smaller than expected. A mean free path of $\lambda_N \simeq 5$ fermi fits the data best. This value is supported by recent (e,e'p) measurements [Ga92]. The effect of Pauli blocking in nuclei accounts for this suppression of rescattering by limiting nucleon final states. The same effect is seen in experiments on $A(\pi, NN)X$ reactions. Calculations including nucleon re-scattering reproduce the data well. These results can be applied to calculating the effect of rescattering in γ induced reactions as well. Indications are that the 'n-p absorption + rescattering' and 'pion production + reabsorption' processes contribute significantly but do not dominate the $A(\gamma, pp)X$ cross sections. An important exception are the Migdal - Watson type final state interactions between two emitted nucleons with small relative momentum (soft FSI). These produce strong enhancements in all nucleon emission processes but are limited to small regions of phase space.

5

These first three mechanisms may not account for the complete $A(\gamma, NN)X$ cross section, in which case other more interesting mechanisms may contribute significantly. These include.

4. Short-range N-N correlations,

5. Δ-N interactions,

6. three-body forces.

All three of these mechanisms represent a significant refinement or departure from the presently accepted models of N-N interactions. A review of such existing models may be found in any reasonably recent text on nuclear physics [FH74].

Short-range N-N correlations and the Δ-N interaction are really aspects of the same mechanism. The long range part of the N-N interaction is adequately described by a one pion exchange (OPE) model. Starting from a simple pseudoscalar-isovector field describing pions, many of the features of the N-N potential emerge naturally [FH74]. At short range OPE 's fail to describe the N-N potential and it is necessary to modify the nuclear wave function by adding nucleon-nucleon correlation functions to restore agreement with data. This phenomenological approach lumps together all parts of the N-N potential which are not generated by OPE. Due to its large influence in the region of the Δ resonance, the Δ-N interaction is often singled out from other short range interactions.

Gottfried [Go58] factorized the $A(\gamma, NN)X$ cross section into two parts,

$$\sigma(2N) = F(p_F)\, G(Q,\omega),$$
(1.2)

where F depends only on the initial momentum distribution of the N-N pair in the nucleus and G contains all the information about correlations. A recent paper shows that equation 1.2 is still valid in the presence of meson exchange currents [Bo89] so that even in the Δ resonance region, $A(\gamma, NN)X$ data should provide information about N-N correlations.

The topic of three-body forces in nuclei has gathered much interest lately. The definition of a three-body force can vary somewhat in different theoretical approaches

6
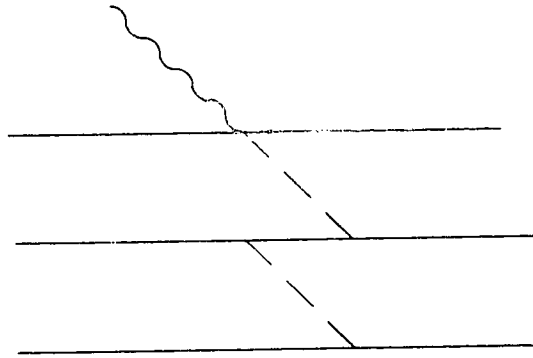
Figure 1.2: Example of a three-body nuclear force.

but it refers basically to processes like those in figure 1.2, which are not included in the traditional single particle potential well or pairwise N-N interactions of the shell model. These are small effects and require precise calculations of competing processes. Recent π absorption reactions on $^{3-4}$He [Ba88, Ba89] have been interpreted as demonstrating three-body force contributions but the results are not definitive. Verification awaits higher statistics experiments with 4π detectors.

The large number of competing processes make detailed theoretical calculations intractable. Qualitative agreement has been obtained with intra-nuclear cascade models (INC), which use a Monte Carlo technique to simulate all the interactions in the nucleus [Car92]. Detailed microscopic calculations of both $A(\gamma, \pi N)X$ and $A(\gamma, NN)X$ interactions are at an early stage. There is a need for coincidence experiments with complete angular distributions, to disentangle the many possible reaction mechanisms. Final state interactions of π's and N's can be calculated quite accurately. Experiments to date have not yet found clear signatures of electric quadrupole absorption or strong FSI contributions.

The combination of SALAD's large acceptance and a tagged photon beam make it possible for the first time to measure $^{12}C(\gamma, pp)X$ with complete energy and angular distributions; including previously unmeasured out of plane p-p coincidences. These data should provide a much more stringent test of theoretical models of multi-nucleon

7

en.ission than previous, inclusive $A(\gamma,N)X$ experiments. The aim is to clearly identify the mechanisms responsible for multi-nucleon emission in nuclei. With an increase in yield of three orders of magnitude, we can go beyond the simple mechanisms of nucleon absorption and pion production to search for subtler and more interesting physics in the short range interaction of nucleons within the nucleus.

Chapter 2

Experimental Set-up

2.1 The Experiment

This chapter describes an experiment performed at the Saskatchewan Accelerator Laboratory on the campus of the University of Saskatchewan in Saskatoon. The data was taken in June 1992 using the Saskatchewan-Alberta Large Acceptance Detector (SALAD). The experiment used tagged photons in the range 187 MeV $< E_\gamma <$ 227 MeV to measure inclusive $^{12}C(\gamma, pp)X$ cross sections. The equipment used to perform this experiment is described in the following sections.

2.2 Photon Beam and SAL Tagger

2.2.1 Electron Beam and Pulse Stretcher Ring

The source of the beam for this experiment was the Saskatchewan Accelerator Laboratory's (SAL) electron Linear Accelerator (linac). It accelerates electrons through six radio-frequency cavities to energies of up to 300 MeV. The beam is pulsed with a duty factor of 0.03% . The electron flux is packed into pulses of 2.5 μs duration, limiting its usefulness, for coincidence experiments. If the same flux of electrons could be spread more evenly over time, detector dead time would be reduced. The rate of real tagged events to random coincidences would also be improved as described in section 2.2.2 At

9

SAL this increase in duty factor is achieved by injecting the linac beam into the EROS (Electron Ring Of Saskatchewan) [Da89] pulse stretcher. The energy of the electron beam is maintained in the ring by radio frequency cavities. The beam can then be slowly extracted from the ring with theoretical duty factors near 100%. During the experiment described here EROS delivered an electron beam of 290 MeV with an average duty factor of approximately 45% over 11 days.

2.2.2 Photon Tagger

Upon extraction from the pulse stretcher ring, the electron beam passes through a 115 μm aluminum radiator producing bremsstrahlung photons. The beam enters the field of the tagger magnet shown in figure 2.1. This dipole magnet momentum momentum analyzes the interacting electrons at the tagger focal plane. The focal plane detector consists of 63 thin plastic scintillators (3.2 mm thick) arranged in two overlapping rows. A coincidence between a front row scintillator and a back row scintillator defines an electron hit in the tagger focal plane. This reduces backgrounds and photomultiplier dark current. The two rows of scintillators are offset by half a scintillator width such that 62 tagger channels are defined by front-back coincidences.

The tagger magnet field is set such that only electrons which have undergone bremsstrahlung in the radiator are steered into the focal plane detector. Electrons which preserve their full energy are steered to a shielded beam dump using a secondary dump magnet (see figure 2.1).

The bremsstrahlung photons continue in the beam direction passing through a series of collimators, a sweeping magnet and into the SALAD to initiate photonuclear reactions. The coincidence of hits in the SALAD scintillators (an X-trigger) with a valid hit in any tagger channel defines an event trigger. This 'tags' the photon's energy which is simply

$$E_\gamma = E_{beam} - E_{e-},$$ (2.1)

where E_{beam} is the original electron beam energy and E_{e-} is the energy determined in the focal plane. This is a great advantage over older experiments which used the entire bremsstrahlung spectrum with an unknown photon energy. To normalize the yield of

Experimental Arrangement

dump magnet for
unconverted e-

beam dump
shielding walls

tagger focal plane
detector

wire chambers
(inner & outer)

bremsstrahlung
radiator

gas cell

ΔE·E calorimeter

shielding & collimators

Tagging Spectrometer   SALAD
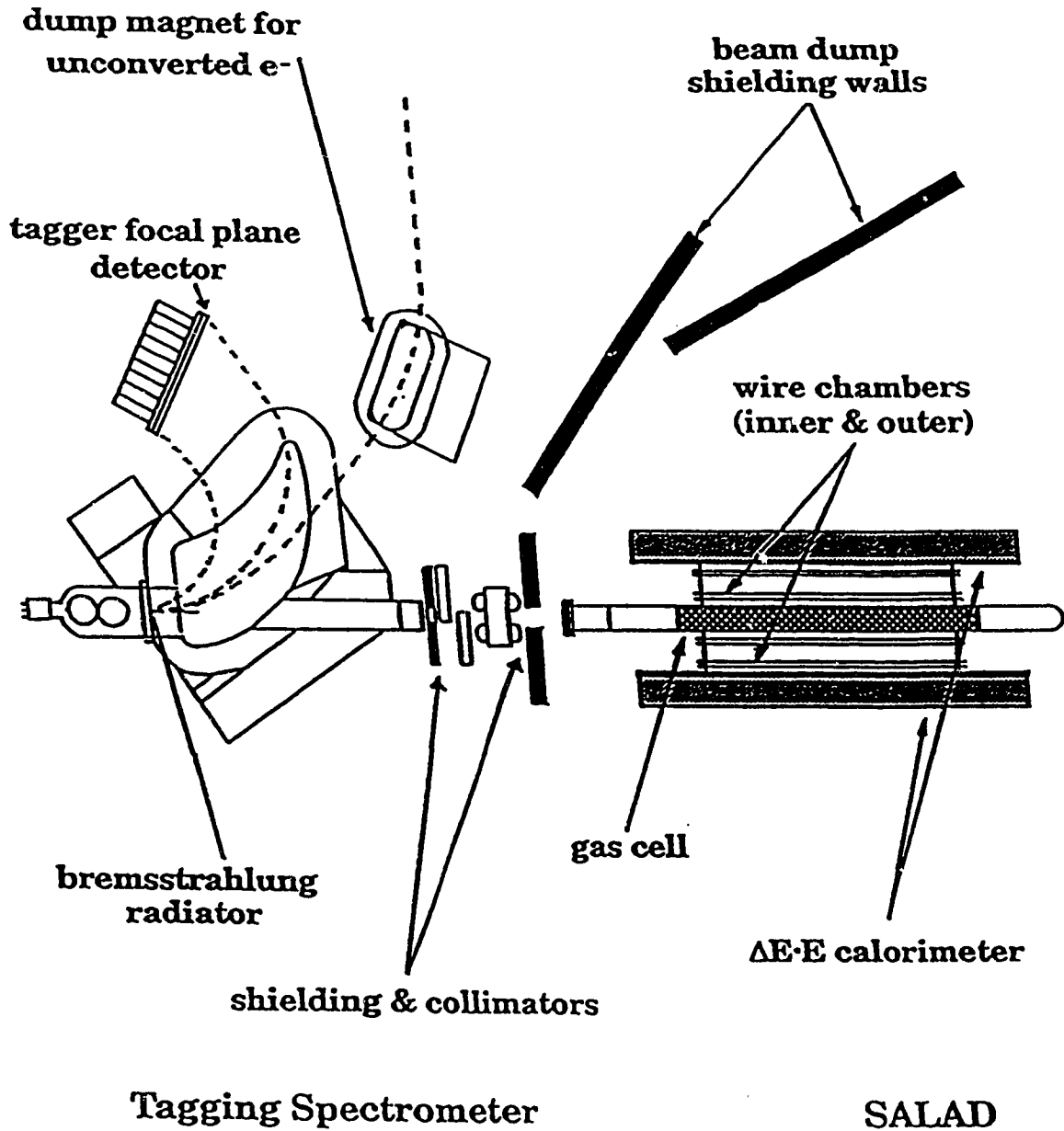
Figure 2.1: The SAL Photon Tagger and SALAD detector.

11

such an experiment and calculate a cross section requires a precise measurement of the complete photon flux and an accurate knowledge of the shape of the bremsstrahlung spectrum. In a tagged photon experiment the normalization is simpler. Only photons in the tagged range are used to trigger events. The sum of electron hits in the tagger focal plane corrected for the the tagging efficiency provides the normalization. The tagging efficiency is simply the number of tagged photons in the detector over the number of electrons detected in the focal plane with a background correction. The tagging efficiency is measured using a lead glass Cerenkov detector to detect photons in coincidence with electrons in the focal plane. The Cerenkov detector has been checked with an electromagnetic interactions simulation and found to be very near 100% efficient. A background run is done with no radiator in the electron beam. The tagging efficiency is simply

$$\epsilon_{tag} = \frac{N_\gamma - N_\gamma'}{N_e - N_e'} \tag{2.2}$$

where N_γ is the number of coincidences between the Cerenkov counter and the tagger focal plane and N_e is the total number of electrons detected in the focal plane. N_γ' and N_e' are the same totals with no radiator present (background). The principal loss of photons is due to collimation of the photon beam. These efficiency measurements use very low intensity photon beams to avoid damaging the Cerenkov counter but the tagging efficiency should have no dependence on the beam current. Tagging efficiency measurements were made approximately every 24 hours during this experiment.

The tagged events will always include some fraction of accidental coincidences which occur when an uncorrelated electron is detected in coincidence with a trigger in the X-arm. Figure 2.2 shows a typical timing spectrum. The time to digital converter (TDC) starts on a valid SALAD trigger and stops on a hit in the tagger focal plane. The spectrum shows a sharp peak of true coincidences with an approximately flat background of random coincidences. A random coincidence arises when a trigger in SALAD is detected in coincidence with an uncorrelated electron in the tagger focal plane. Both these events are proportional to the instantaneous electron beam flux hence the rate of random coincidence events is proportional to the square of the primary electron beam flux. In a true coincidence, both the photon and the associated electron are produced by

12
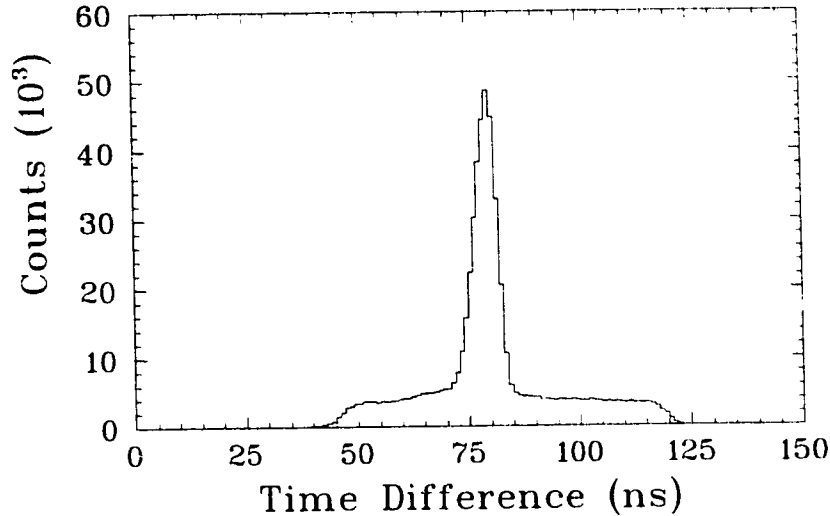
Figure 2.2: Typical time difference between SAL tagger and SALAD detector.

the same incident electron therefore the rate of true coincidences is directly proportional to the primary electron beam flux. Therefore the ratio of true to accidental coincidences increases in proportion to the duty factor for a given average flux.

During this experiment, the average beam flux was $2 \times 10^6 \gamma$ / s for photons in the tagged range 187 MeV $< E_\gamma <$ 227 MeV. The SAL photon tagger is described in detail by Vogt et al. [Vo93].

2.2.3 Collimators and Shielding

As it leaves the tagger magnet, the photon beam emerges from the vacuum of the beam pipe into air (see fig 2.1). The exit window consists of 0.5 mm Al and 125 μm of kapton. The primary collimators are tapered lead blocks, 12.6 cm in length. The first collimator, which defines the beam, had a diameter of 1.5 cm. It was positioned 187 cm downstream of the radiator which gives a maximum beam divergence of approximately 0.0040 rad. The photon beam then passes through a 2.0 cm diameter cleanup collimator, a dipole sweeping magnet, a second cleanup collimator 3.0 cm in diameter and finally enters the SALAD target. The diameter of the two cleanup collimators was chosen large enough that it does not intercept the beam defined by the first collimator. The sweeping magnet

13

was intended to deflect stray electrons from pair production or Compton scattering. Tests with a field of 3.0 kG showed no reduction in background rates and the sweeping magnet was not used during data taking.

Electrons from pair production by the primary photon beam cause considerable background in the SALAD detector. This background originates from locations such as the beam-pipe exit-window, the edges of the collimators or target entry and exit windows, where the photon beam passes through a dense material. In order to shield the detector from such photon beam related backgrounds, the the beam passes through a small hole in two fixed lead walls which bracket the primary collimators and sweeping magnet (see figure 2.1).

Further downstream, electrons produced at the SALAD target entry window are outside the tracking acceptance of the wire chambers but can still cause scintillator triggers and raise leakage currents in the inner wire chambers. In order to stop these electrons, a shielding collar was mounted on the target window flange (see fig 2.3). It consisted of two concentric cylinders, each 26 cm in length. Both cylinders were 3.2 mm thick with the inner being made of aluminum while the outer was lead. The shield was short enough to remain outside the tracking acceptance of the wire chambers.

A potentially large source of background is the primary electron beam with a flux approximately 10^3 times larger than the secondary photon beam. Two large lead shielding walls (see figure 2.1) were placed to shield the SALAD detector from the primary electron beam dump as well as any scattered electrons from the dump magnet.

2.3 The Target

A long thin-walled cylindrical gas target cell was designed specifically for use with the SALAD detector, shown in figure 2.1. The beam travels down the axis of the cylinder which corresponds to the Z axis of the SALAD coordinate system. For experiments requiring gas targets, the cell provides a large areal density which boosts the event rate. At the same time particles produced in the target pass through a minimal amount of material before passing into the detector, hence energy thresholds are kept low.

The wall of the target cell within the tracking acceptance is a light but strong tube
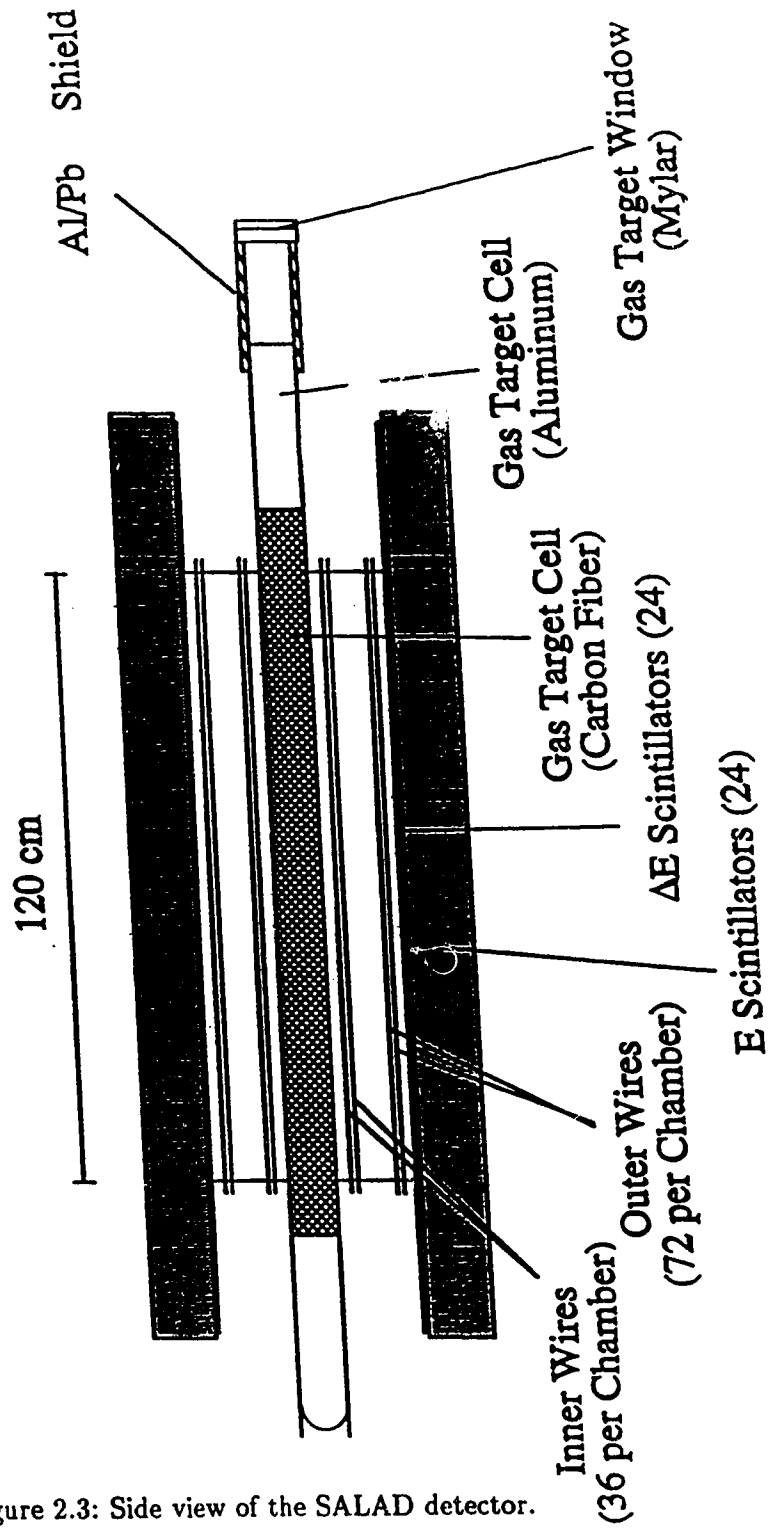
Figure 2.3: Side view of the SALAD detector.

of epoxy impregnated carbon fibers with a thickness of only 0.51 mm. A mylar liner on the inner surface provides the pressure seal. Sections of aluminum tubing are epoxied to both ends of the carbon fiber. The aluminum tubes are threaded so that they can be attached to end fittings; an aluminum dome at the downstream end and aluminum flange at the upstream end. The beam enters the target through a 0.71 mm thick mylar window mounted in the upstream flange.

Data for ^{4}He(γ,pD) and ^{4}He(γ,pp) were taken simultaneously with the ^{12}C data. At the beginning of the run the target was filled with ^{4}He gas at 714 KPa pressure. Diffusion and small leaks decreased the pressure to 657 kPa after 9 days of running. The target temperature and pressure were continually monitored during data taking.

In addition to the helium gas, three solid polyethylene targets were mounted inside the target cell. The three polyethylene disks had an average thickness of 1.58 $\pm$ 0.01 mm and a radius of approximately 30 mm. They were suspended, perpendicular to the beam, near the centre of the detector approximately at Z = 0. $\pm$ 300 mm. The polyethylene was JAYTREX 1000 which [Jo84] has a density of 0.944 $\pm$0.001 $\frac{g}{cm^3}$ and is 85.6% carbon by weight.

2.4   SALAD Detector

2.4.1   Overview

SALAD was designed and built at the University of Alberta for use in photonuclear physics experiments. Its design and calibration are described by Cairns et al. [Cai92]. Figure 2.3 shows a side view of SALAD while figure 2.4 shows a cross sectional end view. At the centre of SALAD sits the target cell, described in the previous section. As charged particles leave the target they pass through four concentric cylindrical wire chambers which track them. Finally a calorimeter of plastic scintillators measures both dE/dX and the total energy of the charged particles. SALAD's large acceptance makes it ideal for coincidence measurements.

16
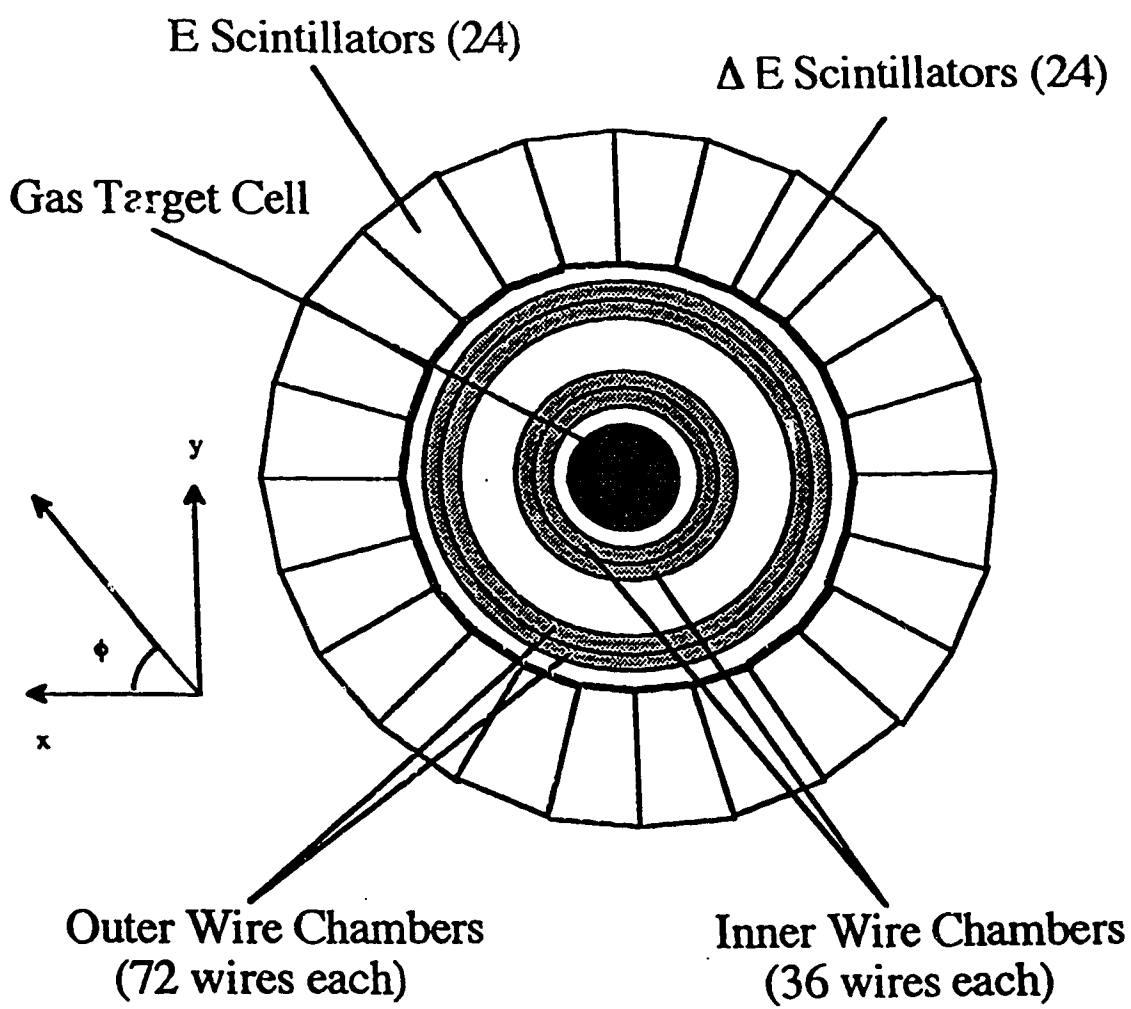
Figure 2.4: End view of the SALAD detector.

2.4.2 The Wire Chambers

The SALAD wire chambers consist of four concentric cylinders with their common axis along the beam direction. Each cylinder is subdivided into individual cells containing one sense wire which is also parallel to the beam direction. Chambers 1 and 2 contain 36 cells each while chambers 3 and 4 have 72 cells each. Figure 2.5 shows the basic construction of the chambers. The cylindrical walls which divide the wire chambers provide the structural strength. They are made of polyurethane foam to reduce energy loss. This design avoids the use of support rods which would introduce gaps in the tracking acceptance. The foam is covered by a layer of graphite-coated kapton. The dividing walls between cells are made of graphite-coated kapton. The wires are 50 μm diameter Stabilohm 650 [Ca86]. The cells in adjacent wire chambers are offset by half a cell width (see fig 2.5). This results in a standard deviation of 2.6° in azimuthal tracking angle (ϕ).

During operation the wire chambers are filled with a mixture of 70% isobutane and 30% argon and a voltage of - 3.5 to -3.8 kV is applied to the chamber cell walls. Under these conditions the chamber operates in self-quenching-streamer mode [Br75, Al80, Ma88] which produces large gain with little proportionality while maintaining good position resolution. The anode signal from each end of each wire is fed to a separate amplifier and ADC.

The Z position along a wire is determined by charge division. If the amplifier gains and input impedances at the two ends of the wire were exactly matched, the Z position would be directly proportional to the charge difference / sum, defined by

$$\Delta Q = \frac{A_u - A_d}{A_u + A_d}.$$
(2.3)

where A_u and A_d are the ADC values for the upstream and downstream ends of the wire, respectively. Small differences in gain lead to a small correction proportional to ΔQ^2, while variations in input impedance lead to an offset. Hence in SALAD, we calculate the position of a hit along a wire as

$$Z = L_0 + L_1 \times \Delta Q + L_2 \times \Delta Q^2.$$
(2.4)

18
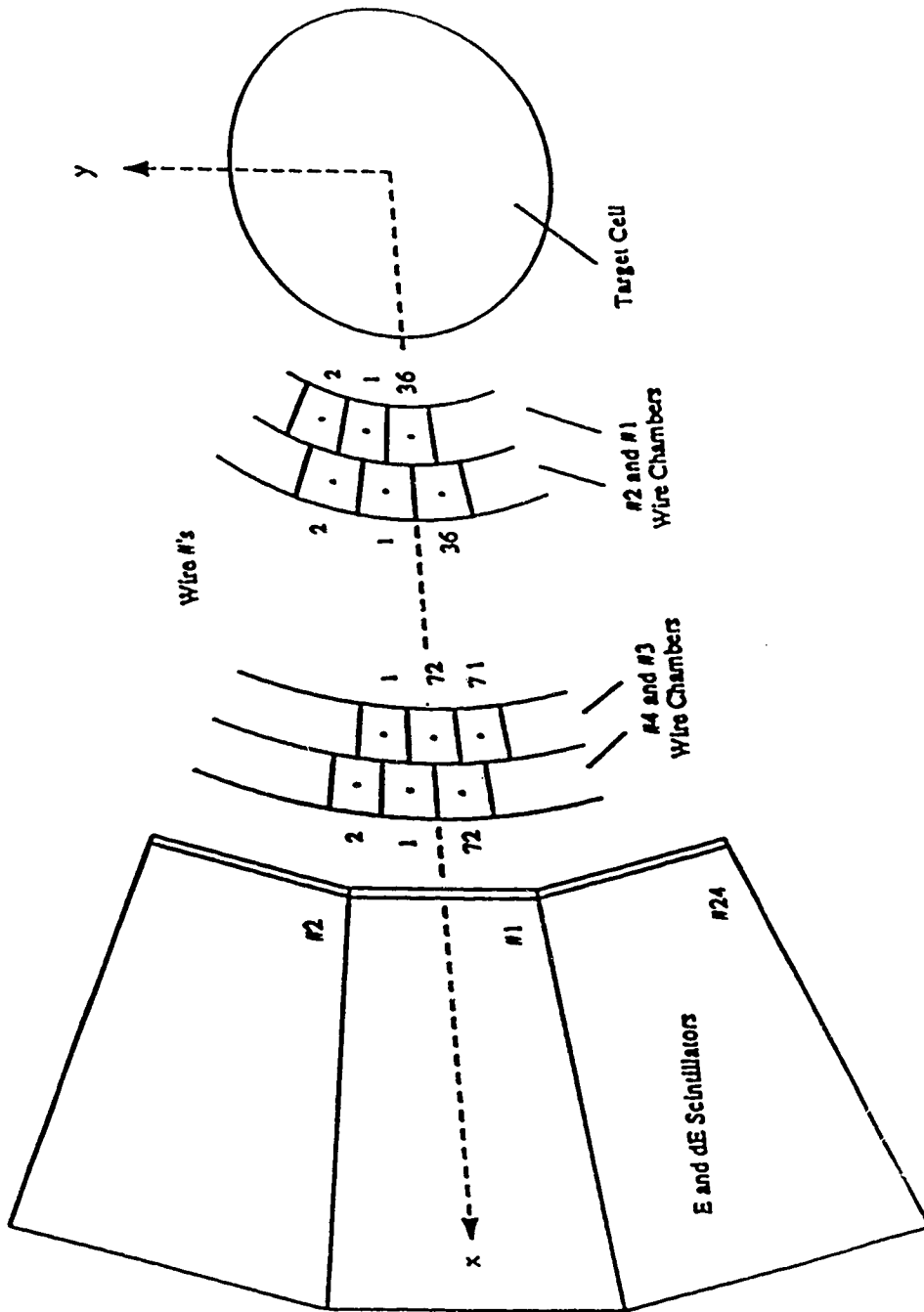
Figure 2.5: SALAD Wire Chamber Construction.

19
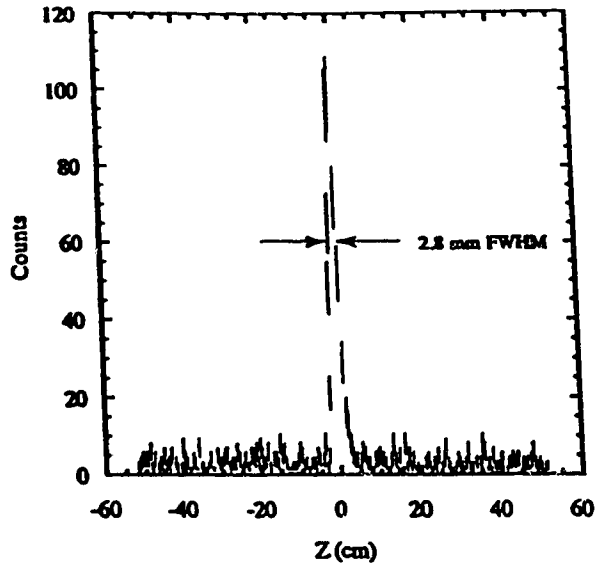
Figure 2.6: Source Calibration spectrum for Wire Chamber Z position.

The wire chambers are calibrated using the two ^{55}Fe sources. The sources emit x-rays collimated to a 1 mm spot size; one pointing inward toward chambers 1 and 2, the other outward toward chambers 3 and 4. The chambers register the electrons produced by photoabsorption and Compton scattering. Data is generally taken with the sources at seven known Z positions and the parameters L_0, L_1 and L_2 are determined by fitting the ΔQ values. The upstream and downstream preamplifiers are carefully matched so that L_0 and L_2 are small. Before data taking the wire chamber high voltage is optimized to give large charge deposition while maintaining resonable leakage currents (≤ 100 μA). The procedure is repeated at intervals during data taking to ensure the consistency of the calibration.

Figure 2.6 shows a typical calibration spectrum with the source at the centre of the wire ($Z = 0$). The peak has a full width at half maximum (FWHM) of 2.8 mm which includes the position resolution plus approximately 1.0 mm due to collimation of the source. The width of the peak broadens toward the ends of the wire ($Z = \pm 450$ mm) as the signal is attenuated for the end furthest from the hit. Overall the standard deviation for Z position determination varies from 1.2 mm to 2.5 mm near the wire ends. Wire chamber information is combined to calculate the scattering angle (θ) of a particle track. The polar tracking resolution of SALAD is plotted in figure 2.7.

20
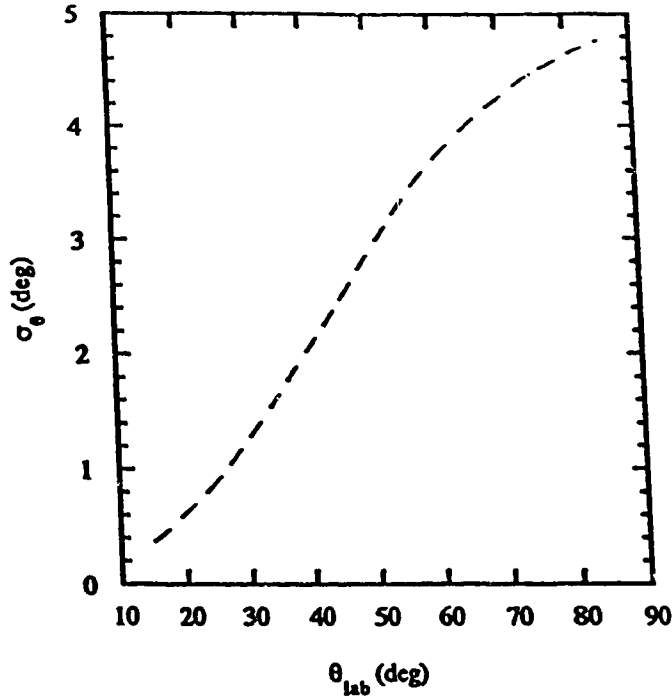
Figure 2.7: Theta resolution of SALAD tracking.

2.4.3 The Calorimeter

The calorimeter as shown in figure 2.4 consists of 24 ΔE - E scintillator telescopes. Each pair is made up of a 3.2 mm thick ΔE scintillator and a 12.8 cm thick E scintillator. The telescopes are tapered to fit together to form a barrel calorimeter which covers 360° in ϕ. The scintillator bars are 1.83 m long with a photomultiplier tube at both ends. During an experiment, the calorimeter information provides the trigger for SALAD. The details of the trigger electronics are discussed in section 2.5. The segmentation of the calorimeter allows SALAD to trigger on multi-body final states.

2.4.3.1 Energy measurement

The scintillator tube gains were originally determined during the SALAD calibration run at TRIUMF [La89, Cai92], using p-p scattering data. During the same experiment, cosmic ray data were collected with the proton beam off. Using the known gains, the stopping power distribution for cosmic rays was determined. This allows SALAD to be re-calibrated at any time using cosmic ray data without the need for a proton beam.

At the beginning of an experiment the scintillator gains are determined from cosmic

data. The photomultiplier tube voltages are then adjusted and more cosmic data acquired. The iterations continue until the scintillator gains are approximately matched. In the analysis of data, a separate gain value is used for each individual phototube; hence variations in gain among the 24 E - Δ E telescopes are corrected. Likewise in the Monte Carlo simulation of SALAD, variations in individual scintillator thresholds are correctly modeled by using separate gain values for each scintillator. Therefore, exact gain matching is not required. Measuring a kinematically overdetermined reaction, such as $D(\gamma,p)n$ or $^3He(\gamma,pd)$, allows an independent check on the gains calculated from cosmics. Cosmic data is acquired at regular intervals during an experiment to determine the variation of the scintillator gains.

The energy resolution of the SALAD scintillators as a function of particle energy was determined in a previous SALAD experiment. Data for the kinematically overdetermined reaction $^3He(\gamma,pd)$ were used to produce figure 2.8, which shows the variation of energy resolution with particle energy for both E and ΔE scintillators. Data for both protons and deuterons are plotted together and fit to the form $\sigma(E) = A + B\sqrt{E}$. The agreement is excellent and the fit was used to model the energy resolution in the SALAD Monte Carlo. Once the Monte Carlo simulation can correctly reproduce the resolutions of the E and ΔE scintillators, we can combine these effects to model the overall resolution in reconstructed particle vertex energy. The error in proton vertex energy is histogrammed in figure 2.9 as calculated by taking the difference between the exact vertex energy of the generated Monte Carlo event and the energy reconstructed by analyzing the simulated data.

As a particle stops in a scintillator, its stopping power becomes large which can cause saturation of the scintillator. The scintillator light outputs are corrected for this saturation effect using the parameterization of Wright [Wr53].

Another correction to particle energies results from nuclear reaction losses in the scintillators. Particles which are absorbed by nuclei before stopping do not deposit their full energy in the scintillator which can lead to misidentification of the particle type or reaction kinematics. The loss of such events must be included in the calculation of detector efficiency. The GEANT hadronic interactions package, GHEISHA [Ca87],

22
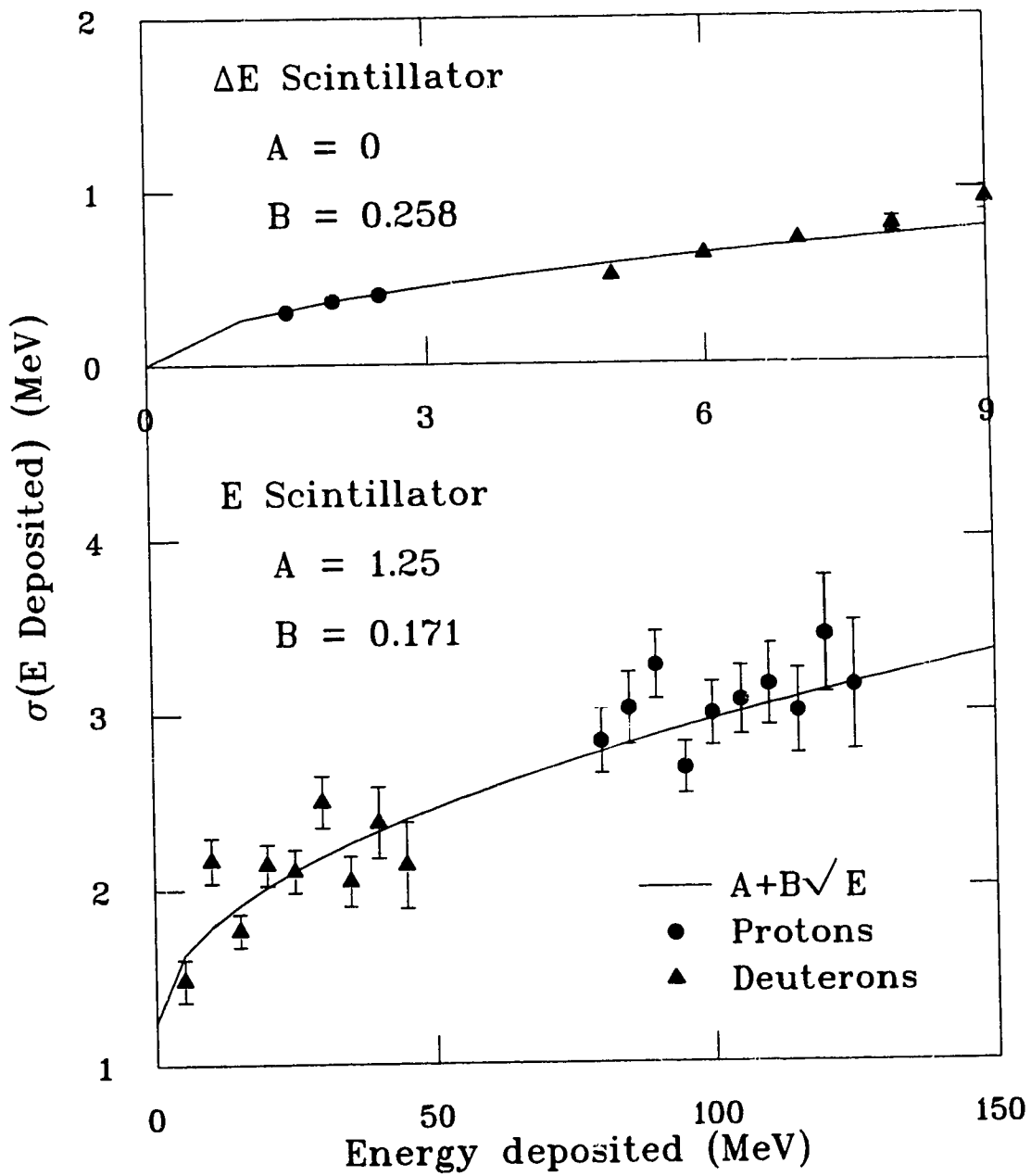
Figure 2.8: Energy Resolution of SALAD scintillators.
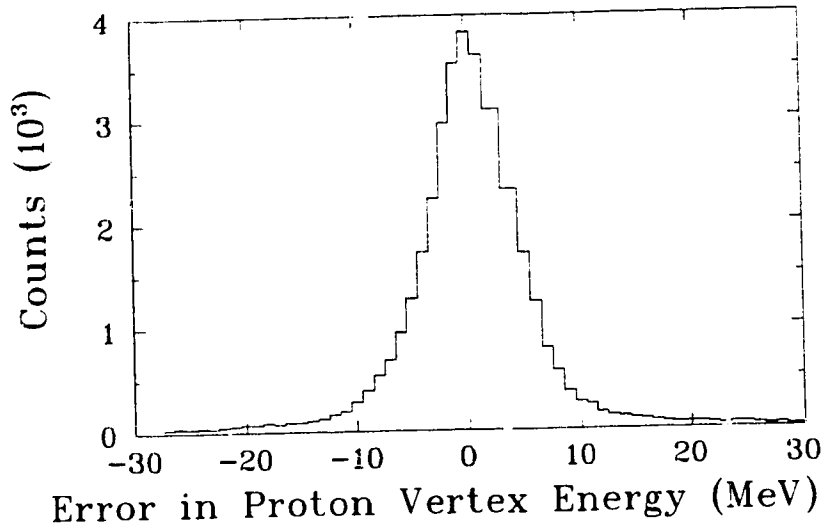
Figure 2.9: The error in proton vertex energy as modeled by the Monte Carlo simulation of SALAD. Data for 35,153 protons with the phase space distribution described in section 3.3.3.1, are displayed.The standard deviation is $\sigma = 6.3$ MeV.

was used to model these processes and calculate the observed energy as a function of the actual incident proton energy. The effect of scintillator reaction losses was included in the Monte Carlo simulation used to determine the efficiency of the SALAD detector (see section 3.3.3).

If a proton with vertex energy exceeding 136 MeV strikes the scintillators at normal incidence, it will pass through the E scintillator without stopping and 'punch through'. This upper limit on kinetic energy varies with particle type and the angle of the track through SALAD. For the kinematic conditions of the $^{12}C(\gamma,pp)X$ experiment, punch through cannot occur. Figure 2.10 summarizes the upper and lower detection thresholds for protons in SALAD.

Energy losses suffered in passing through the target and wire chambers mean that some low energy particles fall below the detection threshold in the E and ΔE scintillators and are lost. The following section gives the details of how these thresholds are applied and how they are used in forming event triggers.

24

**Proton Energies Detectable
in SALAD**
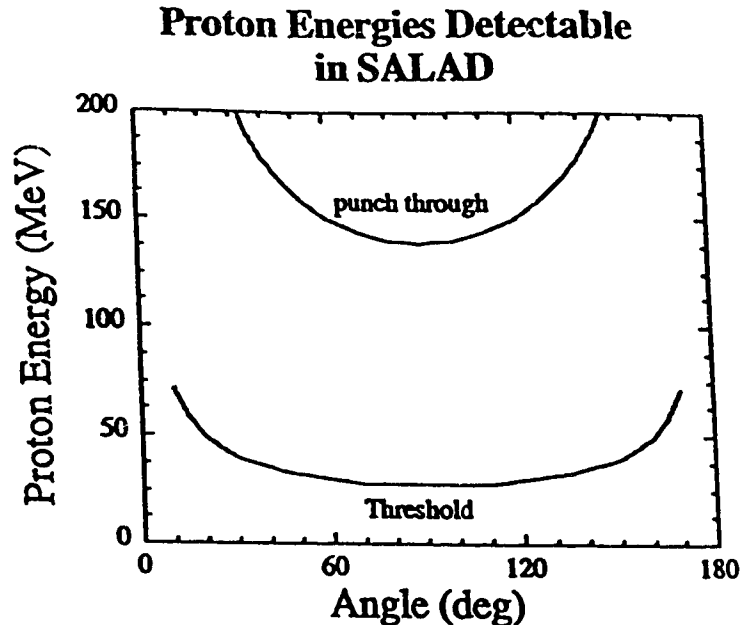
Figure 2.10: Limits on proton energies detectable in SALAD as a function of energy and tracking angle.

2.5 Trigger Electronics and Thresholds

A schematic of the SALAD trigger electronics is shown in figure 2.11. For data taking, the trigger is determined solely from the calorimeter output with the wire chamber information being ignored. Each of the 96 scintillator photomultiplier tubes has three analog outputs. The first is sent through a delay to a LeCroy 1882 Fastbus ADC. The remaining two are used in the trigger logic. Two independent trigger circuits are available and can be used alone or in coincidence. One circuit takes the analog PMT output and converts all 96 outputs to an individual timing signal with a rise time compensated (RTC) discriminator. The 96 discriminator outputs are fed into 24 four-fold coincidence units. Each unit receives the four signals from a single ΔE - E telescope. Any combination of the four signals, upstream E, downstream E, upstream ΔE, and downstream ΔE may be selected with the coincidence unit to give flexibility in forming the trigger. The energy threshold is effectively lowered by not requiring energy deposition in the E scintillators. The simple ΔE threshold rejects electrons with their lower stopping power, but alone it cannot cleanly separate protons and electrons.

The discriminator output is also fed to scalers, a TDC, and a pattern generator.
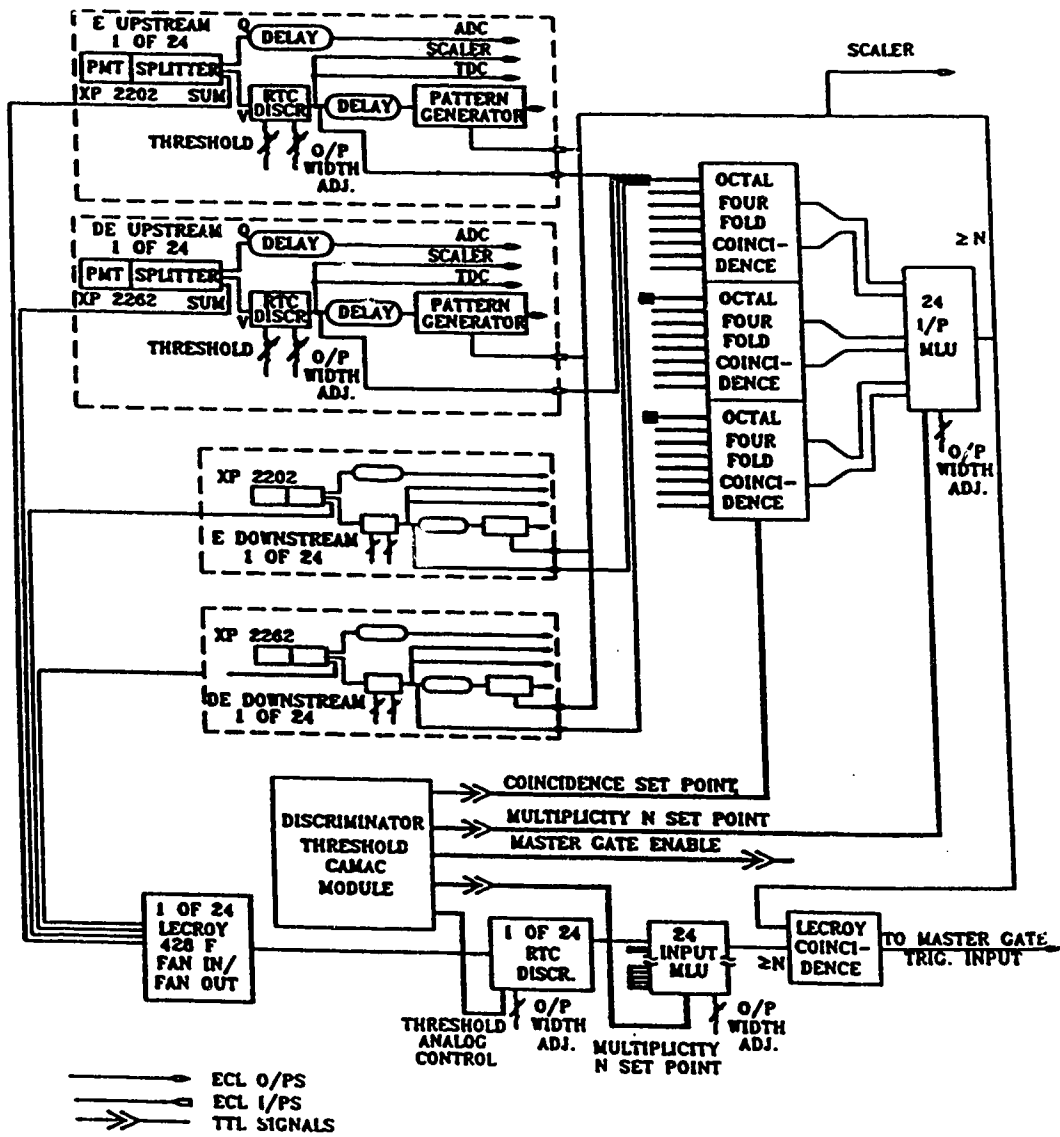
Figure 2.11: Scintillator circuitry and trigger logic.

The TDC's give limited Z position information on scintillator hits while the pattern generator records which scintillators satisfied the thresholds in a valid trigger.

The second trigger circuit, referred to as the sum threshold trigger, rejects background electrons by cutting on the sum of E and ΔE ADC's. The condition is

$$\Delta E_s + (-m) \times E_s > b. \tag{2.5}$$

where ΔE_s is the sum of up and downstream ΔE ADC's and E_s is the E scintillator sum. The slope (-m) is fixed by the ratio of E to ΔE gains and by the relative attenuation in the phototube signal splitters. The sum is accomplished by feeding the PMT outputs into 24 LeCroy 428F Fan in/Fan out modules which sum the four analog signals from upstream and downstream E and ΔE PMT's on a single telescope. This analog sum output is then fed to one of 24 RTC discriminators which output a logic pulse. The discriminator threshold can be varied to adjust the 'b' parameter in equation 2.5.

For particles at normal incidence this would eliminate all electrons which populate the bottom corner of a dE/dx vs E plot. In SALAD, particles enter the scintillators at a wide range of angles. This leads to a large variation in their path length through the ΔE scintillator. Figure 2.12 a) shows a plot of E ADC sum versus Δ E ADC sum. The sum threshold is clearly visible. Using tracking information from the wire chambers we can determine the different path lengths through the ΔE scintillators to produce the proper dE/dx vs E plot shown in 2.12 b). The sum threshold is no longer sharp in the stopping power plot due to the variation in ΔE path length. In analyzing the data, stopping power information is used in conjunction with other measured quantities to identify pions, protons and deuterons.

Once discriminator thresholds have been applied to both the ΔE and sum threshold signals, the two trigger circuits follow parallel but identical paths. The 24 logic pulses enter a multiplicity logic unit (MLU) with a selectable multiplicity of 1 to 4 telescopes. When the number of telescopes meets or exceeds the requested multiplicity the MLU output signifies a valid trigger. In the present experiment, both trigger circuits were used in coincidence. A coincidence was formed between the MLU outputs for the two trigger circuits and the output sent to the Master Gate module. Upon receiving a valid trigger signal the Master Gate sends a gate signal to the ADC's and a start signal to the

27
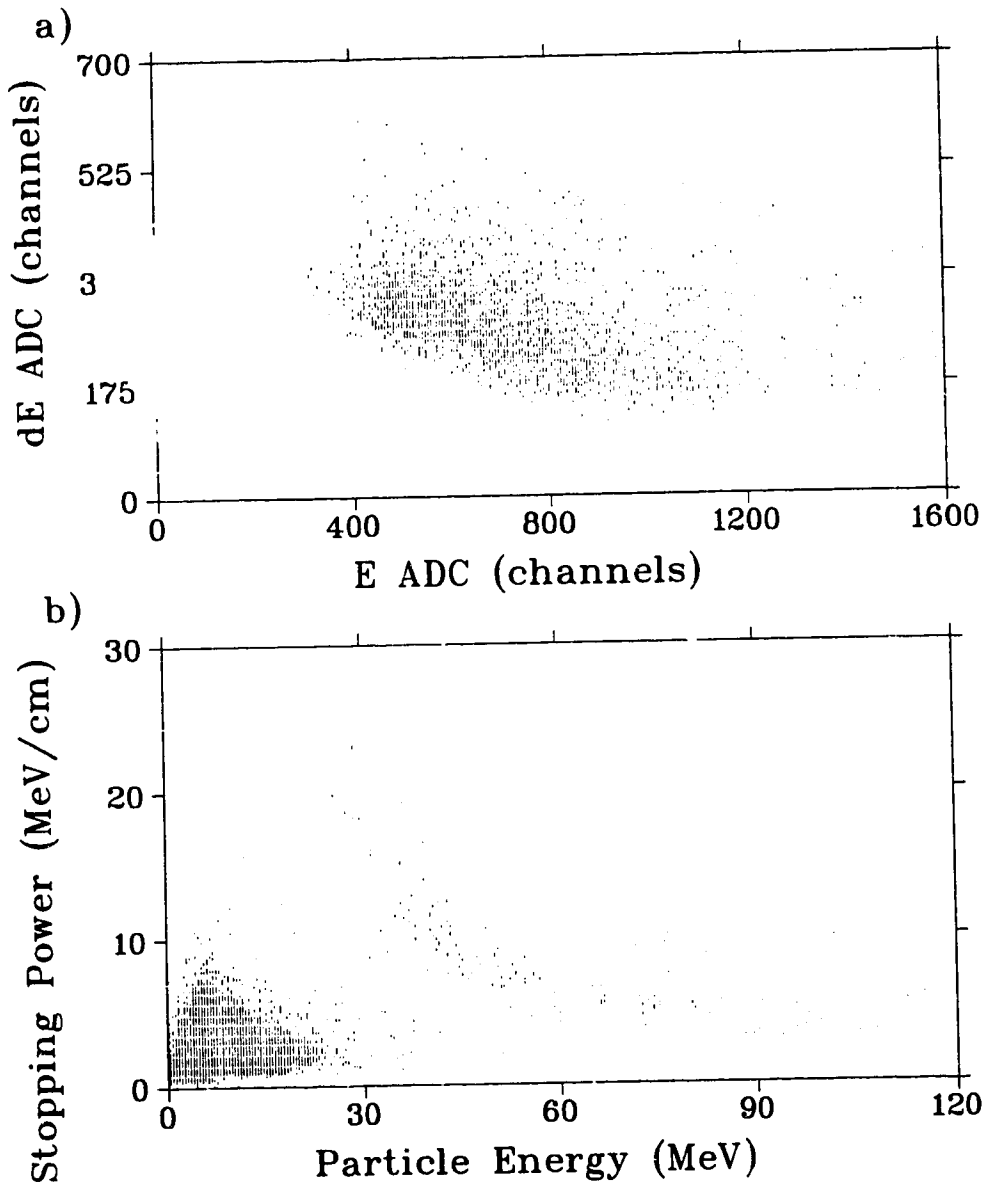
Figure 2.12: a) A plot of E scintillator ADC value versus ΔE ADC value clearly shows the sum threshold. b) A plot of dE/dx vs E for the same data. The plots were generated by analyzing 392,688 events with ≥ 2 tracks from a vertex and ≥ 2 ΔE-E telescope hits.

TDC's to begin conversion. It also interrogates the tagger electronics to see if a photon has been tagged in coincidence. If no photon coincidence exists the event processing is stopped with a fast clear and new triggers may be accepted by the Master Gate.

The resulting trigger requirement in the present experiment was ≥ 2 ΔE signals above and ≥ 2 telescopes for which the sum of the E and ΔE signals is above another threshold. The effect of the trigger is demonstrated in figure 2.12. Valid events were written to tape by a VME processor under the control of the LUCID [Lu91] data acquisition system.

In addition the Master Gate accepts valid triggers for pedestal type and target status type events. These are triggered by the data acquisition software at regular intervals and used to monitor the ADC pedestal values and the SALAD target temperature and pressure, respectively.

Chapter 3

Data Analysis

3.1 Calibrations

3.1.1 ADC Pedestals

SALAD's 528 Fastbus ADC's have 4096 channels each. Even with no input signal they produce a small output signal or pedestal. Before any data taking run an estimate of these ADC pedestals is downloaded to the acquisition computer so that they can be subtracted from the ADC value during readout. In this way output can be compressed by storing only ADC values which exceed a small threshold (30 channels above pedestal for the present run). Variations in the ADC pedestals could cause small errors in the ADC values recorded. For the wire chamber ADC's, this could lead to serious errors in track reconstruction when the data are analyzed. The ADC pedestals are monitored to check their stability.

The ADC pedestal values can be measured by simply reading out all ADC's several thousand times with no beam on and pedestal subtraction disabled. Such a pedestal data run determines the downloaded pedestals to use during a subsequent data taking run. In addition, during data taking runs, pedestal events are recorded to check for variations of the pedestal over time. Pedestal shifts are less than one channel over a 24 hour period. Over a period of three weeks, shifts of 2 to 10 channels are observed. The effect of this shift on wire chamber tracking is difficult to quantify. A test was conducted

ADC pedestal used	2 or more tracks from a vertex $\sqrt{N} = 247$	12C(γ,pX) candidates X = p, π $\sqrt{N} = 45$
online	61,149	2022
offline	61,024	2005

Table 3.1: Effect of ADC pedestal variations on event reconstruction.

in which a single data run (approx. 1 million events) was analyzed with the two different sets of ADC pedestal values. The results, in table 3.1, show that the analysis is not very sensitive to small variations in the pedestal values. The offline pedestals were therefore used for all runs up to this level of skimming. The crucial test is that an appreciable number of candidate events is not lost in making this approximation. Table 3.1 shows that the systematic error is small compared to the statistical error. The misidentification is more significant, when we try to separate the A(γ,pp)X and A(γ,pπ)X events using stopping power information. Hence when making this separation in the third skim pass, the more accurate online pedestal values are used. The details of the cuts made in each skim pass are discussed in section 3.2.

3.1.2 Wire Chamber Calibration

The calculation of z position from charge division along the wires was described in section 2.4.2. The position of the calibration source is verified by feedback. The source is collimated to a width of 1 mm at the wire positions.

Analysis of wire chamber source data yields a histogram of

$$\Delta Q = \frac{Q_{up} - Q_{down}}{Q_{up} + Q_{down}} \tag{3.1}$$

for each of the 216 wires. A single such histogram is shown in figure 2.6. A simple program then sorts through these histograms and determines the centroid and the width of the ΔQ peak. The error in the centroid is taken to be $\delta(\Delta Q) = \sigma/\sqrt{N}$ where σ is the standard deviation of the peak and N is the number of counts it contains.

Occasionally, a ΔQ spectrum contains a second peak in addition to the true peak

Wire Chamber	Wires
1	13
2	15, 19, 23
3	5, 27, 39, 40, 61
4	9, 23, 24, 40, 41, 42, 59, 71

Table 3.2: Wires excluded from analysis of SALAD data due to spurious hits.

corresponding to the source position. The false second peak is caused by hits close to one end of a wire where the charge from the near end overflowed the ADC. These false peaks are eliminated when a limit on maximum charge at a wire end is imposed. Unfortunately this was not discovered until after the initial data reduction passes were complete. In order to avoid the spurious wire chamber hits, the affected wires were excluded from the analysis. Table 3.2 lists the 17 wires which were omitted from this analysis. This produces a small decrease in the geometrical acceptance of SALAD. The decrease is easily determined by turning the same wires off in the Monte Carlo simulation used to calculate SALAD's efficiency.

Figure 3.1 shows a plot of the known Z position of the radioactive source versus ΔQ, for a typical wire. The plot actually shows data from two different source calibration runs, taken 4 days apart. We see that they agree well, confirming that the calibrations did not vary greatly over time. The wire chamber calibration parameters, L_0, L_1 and L_2, used to analyze the present data were determined by averaging these two calibration runs (calibration A). The function

$$Z = L_0 + L_1 \times \Delta Q + L_2 \times \Delta Q^2,\qquad(3.2)$$

was fit to the data using a chi-squared minimization technique. The errors $\delta(\Delta Q)$ in the centroid positions were used to weight the fit. The resulting fit is the solid curve in figure 3.1.

A third calibration run was taken 5 days after the end of the $^{12}C/^4He$ data taking. This run was fit separately (calibration B) and compared to calibration A to determine the systematic error in finding tracks, due to error in the calibration parameters. The

32
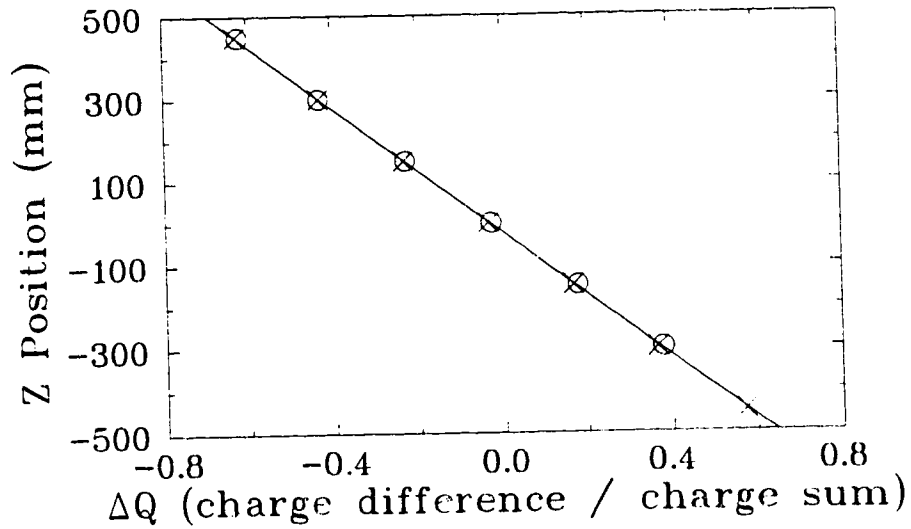
Figure 3.1: Quadratic fit to wire chamber calibration data. Data for two separate calibration runs (X and O) are plotted. The errors in both Z and ΔQ are too small to plot. The distribution of χ^2 values for the 199 wires calibrated peaked at 1.0 with an average value of 3.6

WC Calibration used	12C(γ,pp) candidates $\sqrt{N} = 53$
A	2842
B	2804

Table 3.3: Effect of WC calibration parameters on event reconstruction.

critical test of the wire calibrations is the ability to reconstruct the tracks from candidate events. In order to test the sensitivity of the data analysis to the wire calibration parameters, a single data run was analyzed from tape first using calibration A and then B. The difference in the number of candidate events identified by these two analyses is given in table 3.3 .

3.1.3 Scintillator Gain Determination

The photomultiplier tube gains for the SALAD scintillators can be determined by analyzing the passage of cosmic rays through SALAD, as described in section 2.4.3.1. The cosmic events are collected with the beam off and no coincidence with the tagger required. The trigger is satisfied if two of the large E scintillators are above threshold as a single cosmic ray will deposit energy both as it enters and leaves SALAD.

When the data is analyzed, the SALAD track reconstruction algorithm looks for tracks which pass through the gas target cell. A single cosmic ray then creates two collinear tracks as it enters and exits target cell. After eliminating events with fewer than two distinct tracks, three cuts are made to isolate true cosmic ray tracks.

In SALAD's polar coordinate system, the difference in ϕ angle of the two tracks must be 180° with a small distribution due to finite resolution. Figure 3.2 a) shows a histogram of (ϕ difference - 180°) for events with two tracks and the cut, $| \Delta(\phi) - 180° | < 15°$, applied.

The opening angle is the angle between the two tracks, for coplanar tracks it is approximately $\theta_1 + \theta_2$. Figure 3.2 b) plots ($\theta_1 + \theta_2 - 180°$) and shows the cut applied to select good cosmic events.

Finally the two tracks will not meet exactly due to tracking resolutions but the closest approach of the two tracks (minimum distance between tracks) should be close to zero. Figure 3.2 c) shows the minimum distance distribution and the cut placed at 30 mm. Events passing these three cuts are taken as good cosmic ray events.

The phototube gains were determined during the SALAD commissioning run at TRIUMF by measuring the angles of p-p scattering events. Using these gains the effective energy deposition of cosmic rays was calculated to be 2.10 MeV/cm. Using

34
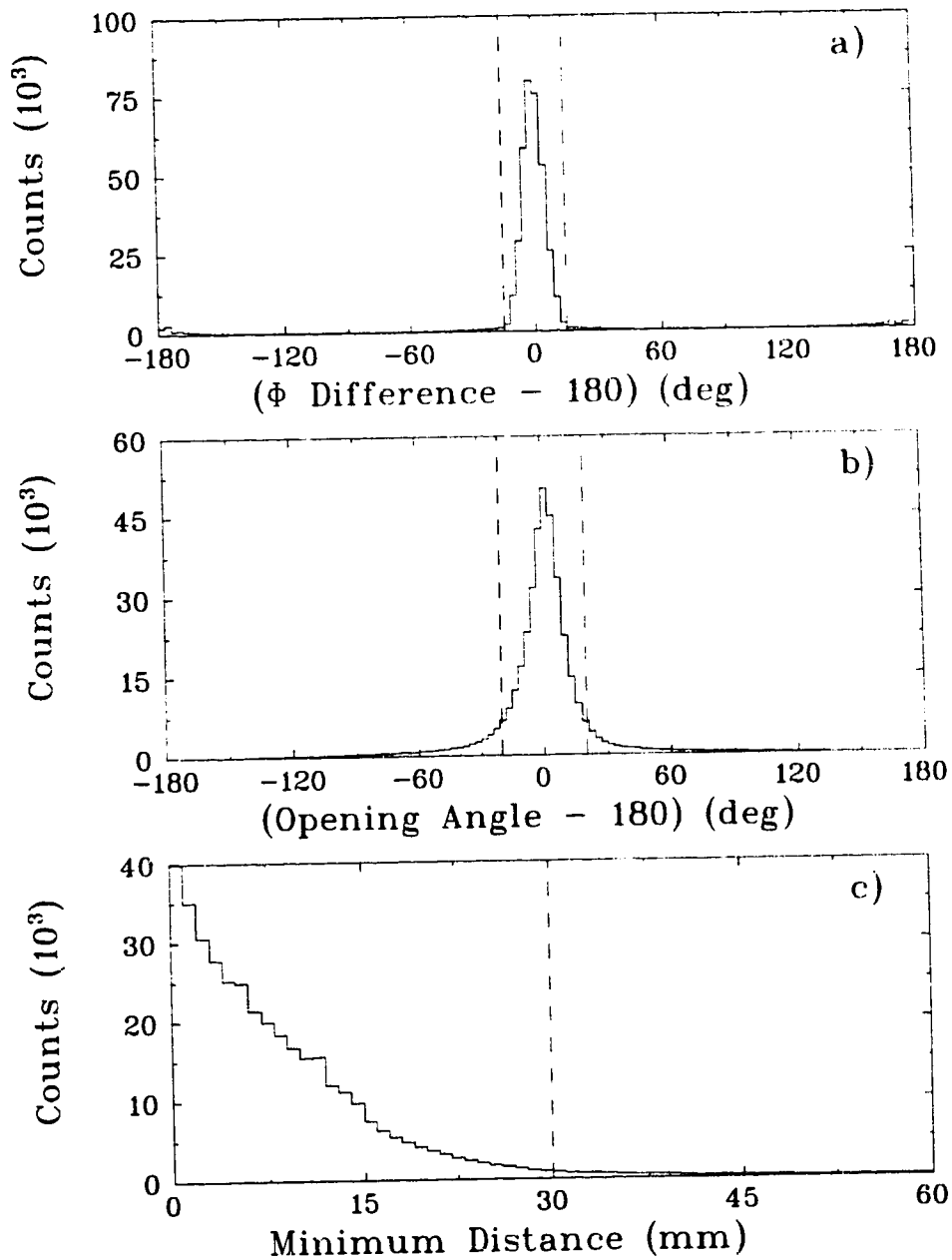
Figure 3.2: Figure a) shows the distribution of ($\Delta\phi$ - 180o) for two-track (one entering, one leaving) cosmic ray events. In b) the distribution of (opening angle - 180o) is shown for the same events. In c) the minimum distance of approach between the two tracks is histogrammed. In all three plots, the dashed line shows the cut used to select cosmic ray events. A total of 385,620 events are displayed.

this known dE/dx value, the phototube gains can be determined for any future SALAD experiment. SALAD's tracking information allows us to calculate the path length of cosmic rays through the E and ΔE scintillators. Combining this with the known dE/dx value, we can calculate the energy deposited in the E and ΔE scintillators. The tube gain is then:

$$gain = \frac{ADC}{E} \times \exp[Z/\lambda],$$

(3.3)

where the factor $\exp[Z/\lambda]$ accounts for attenuation in the scintillator material. This dependence of the gain on the attenuation length λ can be eliminated by combining information from the upstream and downstream phototubes on a single scintillator bar. If we calculate the geometric mean of upstream and downstream phototube gains as $gain_{mean} = \sqrt{gain_{up} \times gain_{dn}}$. Then, $gain_{mean}$ contains an exponential factor $\exp[(Z_{up} + Z_{dn})/\lambda]$ which is a constant since $Z_{up} + Z_{dn} = L$, the length of the scintillator bar. This constant can then be absorbed into the $gain_{mean}$ value and the energy deposited in a scintillator is simply,

$$E_{deposited} = \sqrt{\frac{ADC_{up} \times ADC_{dn}}{gain_{mean}^2}}.$$

(3.4)

The gain for a scintillator is calculated for each cosmic event and shown in the histogram of figure 3.3. The large E scintillator bars give a fairly gaussian distribution of energy loss with a well defined mean to use as the gain. The flat background of events with gains smaller than the peak value is not well understood. It may be due to particles which strike a corner of the large E scintillator and deposit less than their full energy. The thinner ΔE scintillators display a Landau distribution of energy loss which skews the most probable energy loss to lower values. Figure 3.3 b) demonstrates how this skews the ΔE gain distribution as well. Using the mean value of the gain distribution rather than the most probable gives the best estimate of the ΔE gain.

Six separate cosmic data runs were taken over the four week run. Scintillator gains have been determined from each of these calibration runs to check the consistency of the gain values. Figure 3.4 shows a plot of gain versus time for two typical scintillators. A steady decrease in gain value over time is immediately apparent. The phototube voltages were kept constant over this time. The rate of decrease varies from scintillator
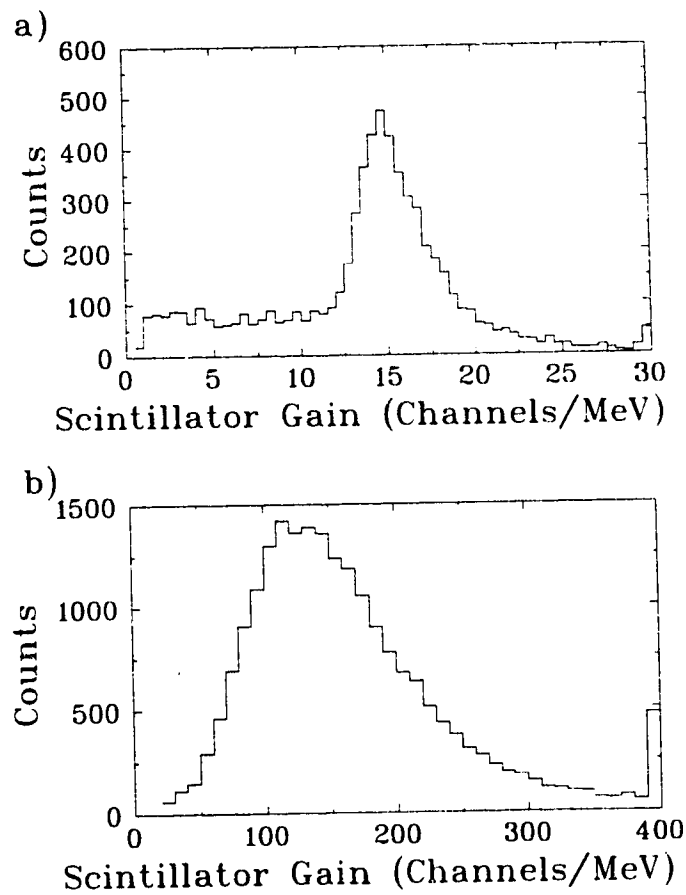
Figure 3.3: Histogram of scintillator detector gain calculated from cosmic ray data. Figure (a) shows an E scintillator spectrum with 6,212 counts. Figure (b) shows a ΔE scintillator spectrum with 20,827 counts.
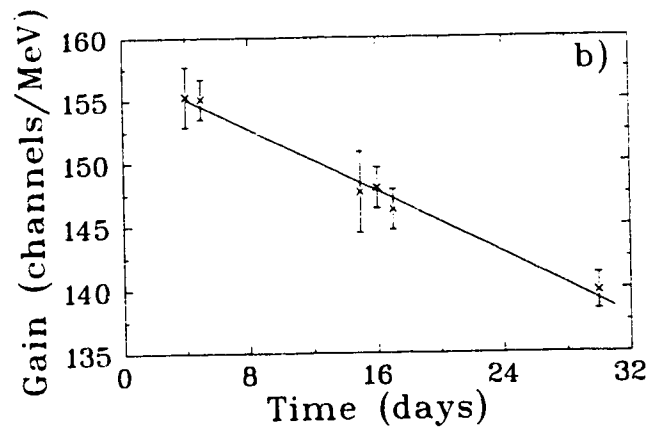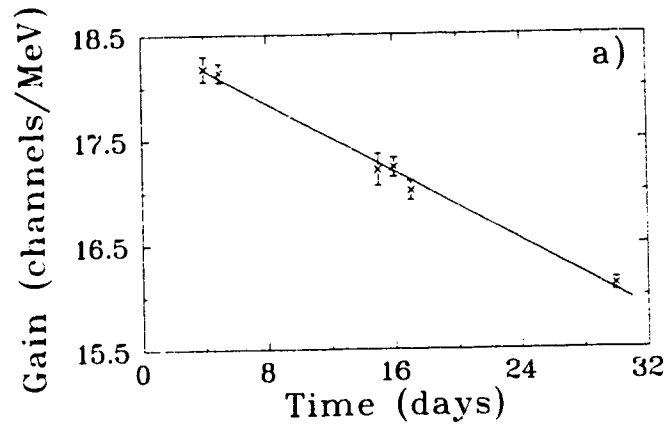
Figure 3.4: Plot of scintillator gain versus time for a) a typical E scintillator and b) a typical ΔE scintillator. The data points are calibration runs, the solid line is the linear fit.

Analysis Pass	Percentage of raw Events Passing Cut
PASS 1: ≥ 2 tracks	29%
PASS 2: ≥ 2 tracks from a vertex	2.9%

Table 3.4: Fraction of events satisfying each analysis pass.

to scintillator with some gains almost constant with time. The change seems to affect E and ΔE scintillators equally. Over the period of ^{12}C/^{4}He data taking (day 15 to day 26 of figure 3.4), the cumulative gain change is typically 5 to 8% and therefore cannot be ignored.

The gain of each scintillator was fit by a function,

$$gain = g_0 + g_1 \, t,\qquad (3.5)$$

with t the time in days. Figure 3.4 shows the excellent agreement between the calibration points and the linear fit. When data are analyzed, the 48 g_0 and g_1 values are used to calculate the gain at the beginning of each run. Over a 100 minute run the gain variation is negligible.

3.2 Cuts Applied

3.2.1 Tracking and Vertex Identification

In the first analysis pass of the ^{12}C/^{4}He data set, only wire chamber information was used in selecting good events. Events in which two or more tracks originate from the target, were kept at this level of the analysis. Table 3.4 shows the fraction of events which satisfied this condition.

The track reconstruction algorithm first looks for hits in the wire chambers. A valid hit requires a non-zero ADC value at both ends of a wire and also requires that the sum of these ADC values (after pedestal subtraction) satisfy a minimum threshold. If hits are present in both inner (chambers 1 or 2) and outer (chambers 3 or 4) wire chambers track reconstruction is attempted.

The track finding algorithm starts the search for hits in the outermost chambers, which have the lowest count rate. When a hit is found in chamber 3 or chamber 4, the nearby cells in the other three chambers are searched. Only nearby cells could produce tracks which pass through or near the target. If two hits in adjacent chambers are separated by more than 200 mm in Z position, they are considered uncorrelated and the search for hits continues. If two or more correlated hits are found with at least one inner chamber hit and one outer chamber hit, a track is fit through the hit positions and a residual is calculated. The residual is the average distance of closest approach between the track and the hit positions. For two hit tracks, a residual cannot be calculated hence a large residual value is arbitrarily assigned ensuring that three and four hit tracks are given higher priority.

When the search is complete all possible tracks through the wire chamber hits have been constructed and sorted by the residual. At this stage tracks may share the same wire hit. The final step is to sort through the candidate tracks starting with the smallest residual value. As good tracks are selected, any candidate tracks which share wire hits with a good track are removed. In this way a large number of candidate tracks is reduced to a few good tracks. For example, two adjacent cells fired in the same chamber, a candidate track would be constructed through each of them (provided sufficient hits were present in other chambers). The candidate with the smallest residual value is kept as a good track and the other track is rejected.

Table 3.4 shows the distribution of track multiplicities for a typical data run. A little over one third of events have no tracks. Since the scintillator bars are longer than the wire chambers, it is sensible that many events satisfy the trigger requirement of two scintillator hits but show one or zero tracks in the wire chambers. Two thirds of the raw data are eliminated by keeping only those events with two or more tracks. Still, many events may contain two unrelated tracks which are widely separated. In the second step of the analysis (PASS 2), these events are cut by requiring that at least two tracks share a common origin or *vertex*, within the SALAD target.

Tracking resolution effects mean that two correlated tracks may not meet at a point. Instead, we calculate the minimum distance of approach for the tracks. For a two track

Track Multiplicity	Number of events
0	355,594
1	346,576
2	288,777
3	5,357
4 or more	237

Table 3.5: Track multiplicity for first analysis pass. This run contained 996,541 events in total.

event, the shortest line segment connecting the two tracks defines the *minimum distance* and the midpoint of this segment is taken to be the vertex position. The minimum distance must be less than 40 mm to pass the vertex requirement.

If more than two tracks are present the analysis code finds the minimum distance for all possible pairs of tracks. The two closest tracks define a temporary vertex and all other tracks within 40 mm of this vertex are assigned to the vertex. The minimum distance for the event is the average minimum distance for every pair combination of tracks assigned to the vertex. The position of the vertex is the average of the midpoints of all the minimum distance line segments.

An event with a valid vertex is defined as one in which

1. The minimum distance for the event is < 40 mm,

2. The radial position of the event vertex is < 60 mm.

Figure 3.5 shows the minimum distance distribution for events with $\geq$ 2 tracks and the cut applied in PASS 2. With no cuts on particle type, electron contamination produces a tail at large values of minimum distance. Multiple scattering of electrons leads to poorly defined track directions and hence poor vertex reconstruction. Figure 3.6 shows the radial position of the vertex distribution and the the cut applied. Both cuts are conservative, to avoid losing good events. As in figure 3.5, electron contamination produces a large number of events with unreasonably large R_{vtx} values. As the candidate $^{12}C(\gamma,pp)X$ events are isolated with further cuts, the electron tail is eliminated from the

41
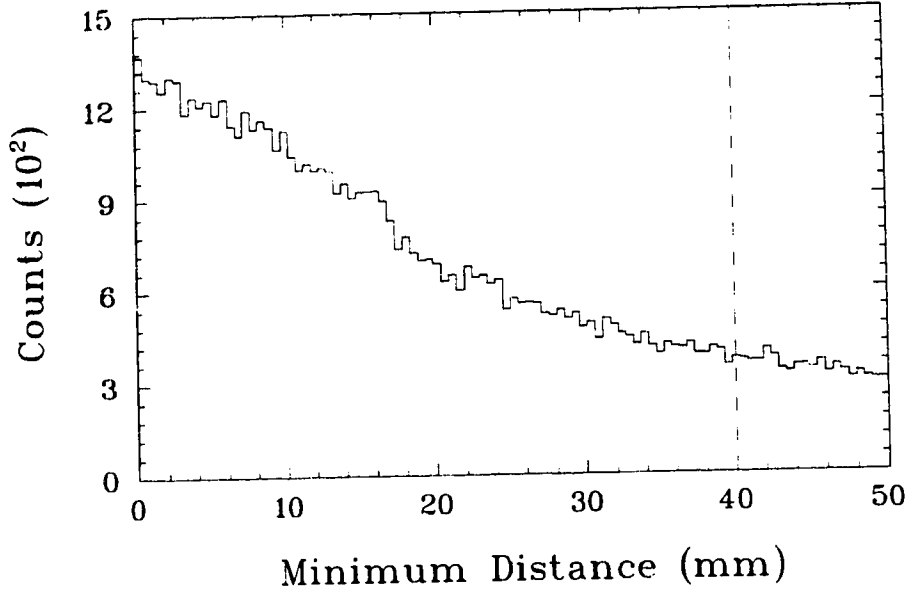
Figure 3.5: Minimum Distance between tracks for events with ≥ 2 tracks and $R_{vtx} < 60mm$. The dashed horizontal line shows the cut made on minimum distance. 67,400 counts are displayed; overflows have been suppressed.

R_{vtx} distribution (see figure 3.22).

As the opening angle between two tracks becomes large, the position of the vertex becomes poorly defined. This is demonstrated in figure 3.7 where Monte Carlo simulated $^{12}C(\gamma,pp)X$ were analyzed and the error in the radial position of the vertex determined. The error, $\delta(R_{vtx})$, is plotted as a function of the proton opening angle. Note how $\delta(R_{vtx})$ increases greatly for opening angles exceeding 150°. For this reason events with opening angles greater than 150° were were excluded from the analysis. The same cut is applied to the Monte Carlo simulated data in calculating the detector efficiency.

3.2.2 Particle Identification

Thus far we have only used the tracking information in the analysis. In the next step, PASS 3, the energy deposition in the calorimeter is used to identify different particle types. Plotting the rate of energy loss, dE/dx, versus the kinetic energy, E, gives

42
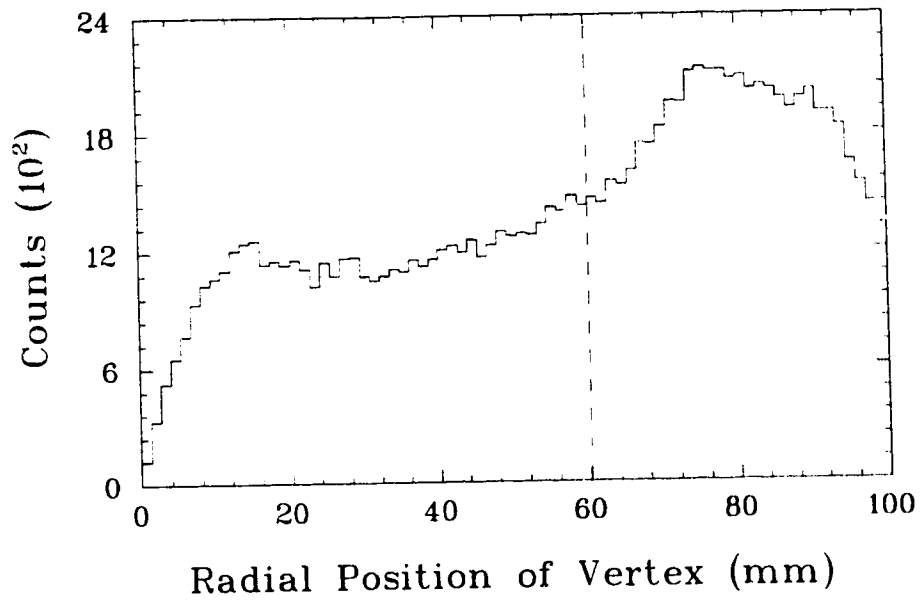
Figure 3.6: Radial position of vertex for events with $\geq$ 2 tracks and minimum distance < 40 mm. The dashed horizontal line shows the cut made on R_{vtr}. 103,365 counts are displayed; overflows have been suppressed.

43
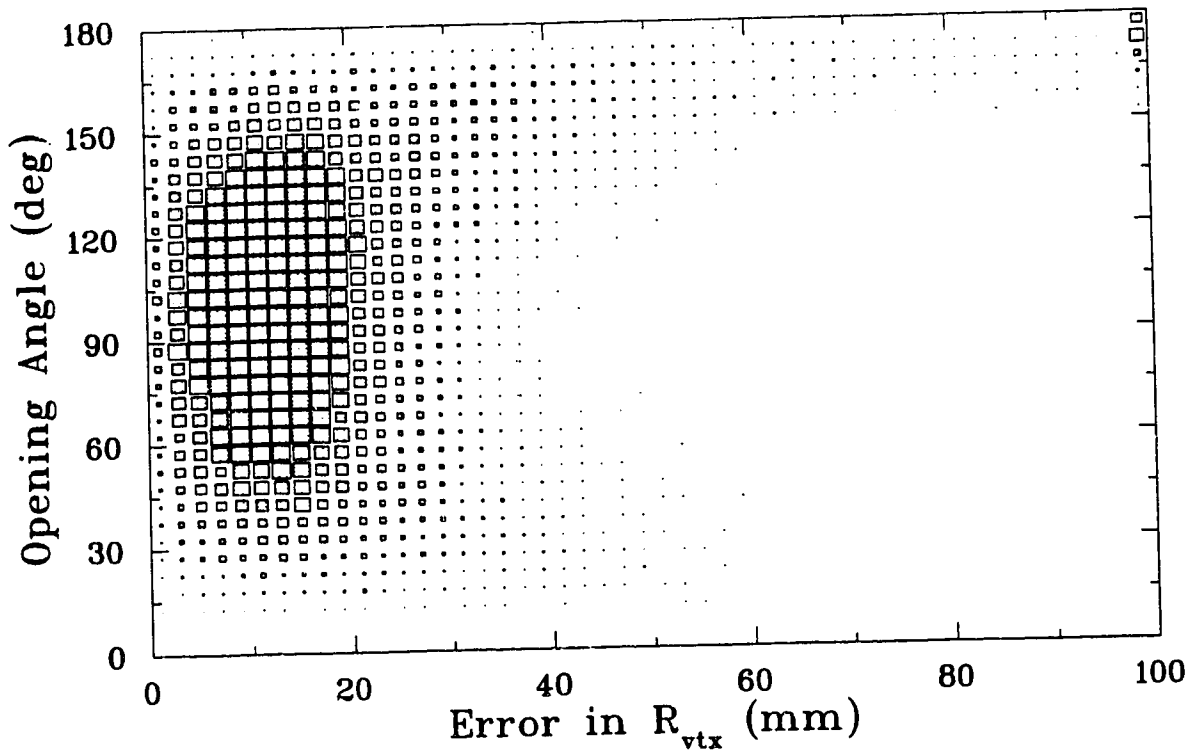
Figure 3.7: Error in Radial position of Vertex versus opening angle for Monte Carlo simulated data. 33,464 events which produced identically two protons from a good vertex are displayed.
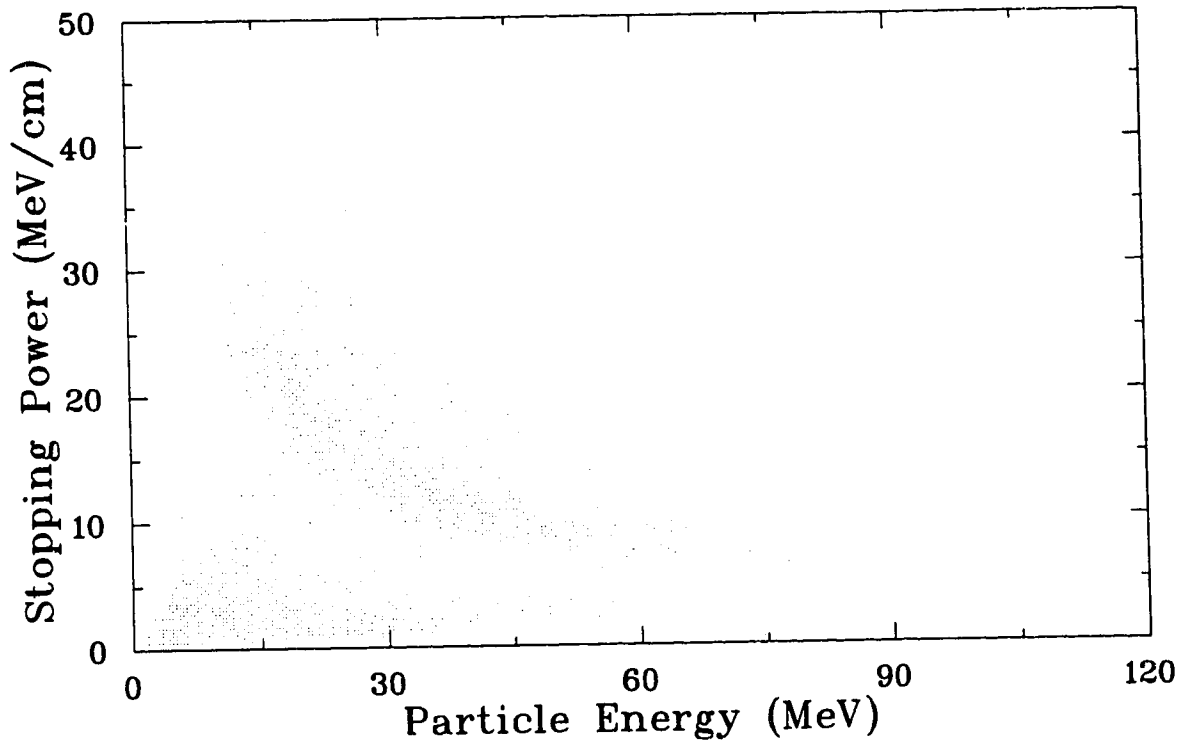
Figure 3.8: Stopping Power plot for events with two or more tracks from a vertex. Data for 685,158 particles is displayed.

distinct loci for particles with different masses. Figure 3.8 is a stopping power plot for SALAD events with two or more tracks coming from a vertex. It clearly shows the separation of electrons in the bottom left corner and protons in the band above. dE/dx is actually approximated by $\Delta E/\Delta x$ where ΔE is the energy deposited in the path length Δx through the ΔE scintillator. E is the total energy deposited in the E and ΔE scintillators.

In order to simplify the cut separating particle types, we define a new variable, PID, which linearizes the stopping power plot. The rate of energy loss of a particle can be approximated by

$$\frac{dE}{dx} \simeq \frac{D\,z^2 A}{E^{\alpha-1}}, \tag{3.6}$$

where E is the kinetic energy of the particle, z and A are its charge and atomic mass
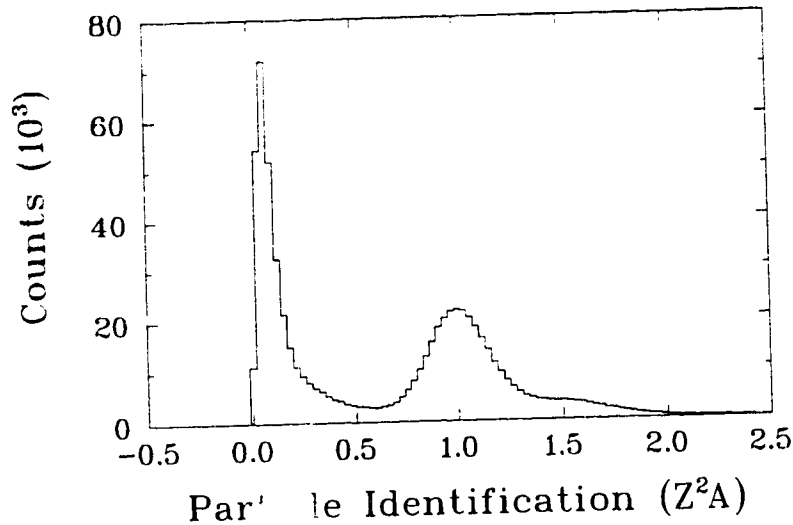
Figure 3.9: Histogram of part identification variable for events with two or more tracks from a vertex. 680,137 counts are displayed; overflows have been suppressed.

number. D and α are constants. Rearranging and integrating equation 3.6, we obtain

$$PID \equiv \frac{[(E + \Delta E)^\alpha - E^\alpha]}{\alpha \, D \, \Delta x} \simeq z^2 A, \tag{3.7}$$

which defines the variable PID. Here, Δx is the path length through the ΔE scintillator and the constants D and α in equation 3.7 are fixed by analyzing a file which contains only protons. Since equation 3.6 is an approximation, PID is only roughly equal to $z^2 A$ and we add a scaling factor such that PID $= 1.0$ for protons. The usefulness of PID is that it linearizes the bands of a stopping power plot so that it can be displayed in a one dimensional plot. Figure 3.9 shows a PID spectrum for events with $\geq$ 2 tracks from a vertex. Unfortunately, the bremsstrahlung photon beam is accompanied by a large number of unwanted electrons. The high energy photons undergo pair production and make e^+e^- pairs which are in coincidence with the tagger. These electrons swamp the pions which would peak around PID $= 0.35$ in figure 3.9. We are fortunate to have coincidence data which helps separate out the electron background.

For any event with two or more tracks coming from a vertex, we have a value of PID for each particle. Figure 3.10 is a two dimensional plot of the PID of one particle versus the PID of the other, for two track events. They are sorted such that the larger

46
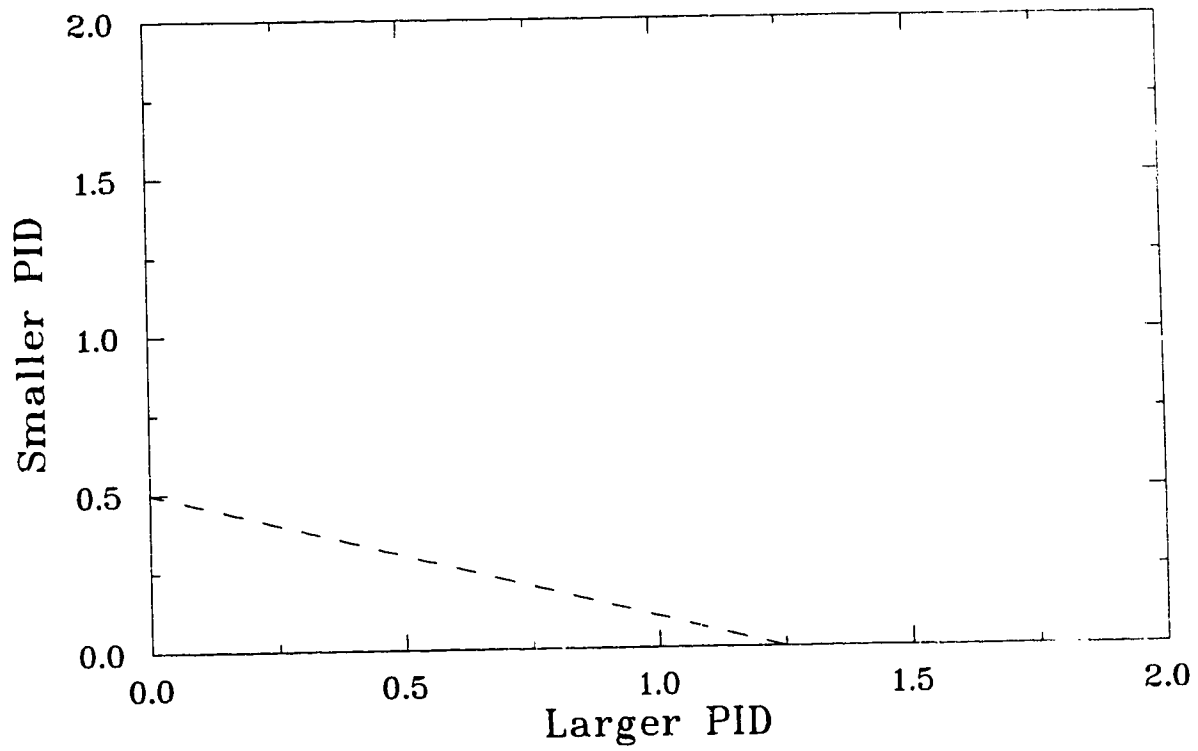
Figure 3.10: Two dimensional histogram of PID$_{lesser}$ versus PID$_{greater}$ for events with exactly two tracks from a vertex. 323,204 events are displayed. Overflows have been suppressed.
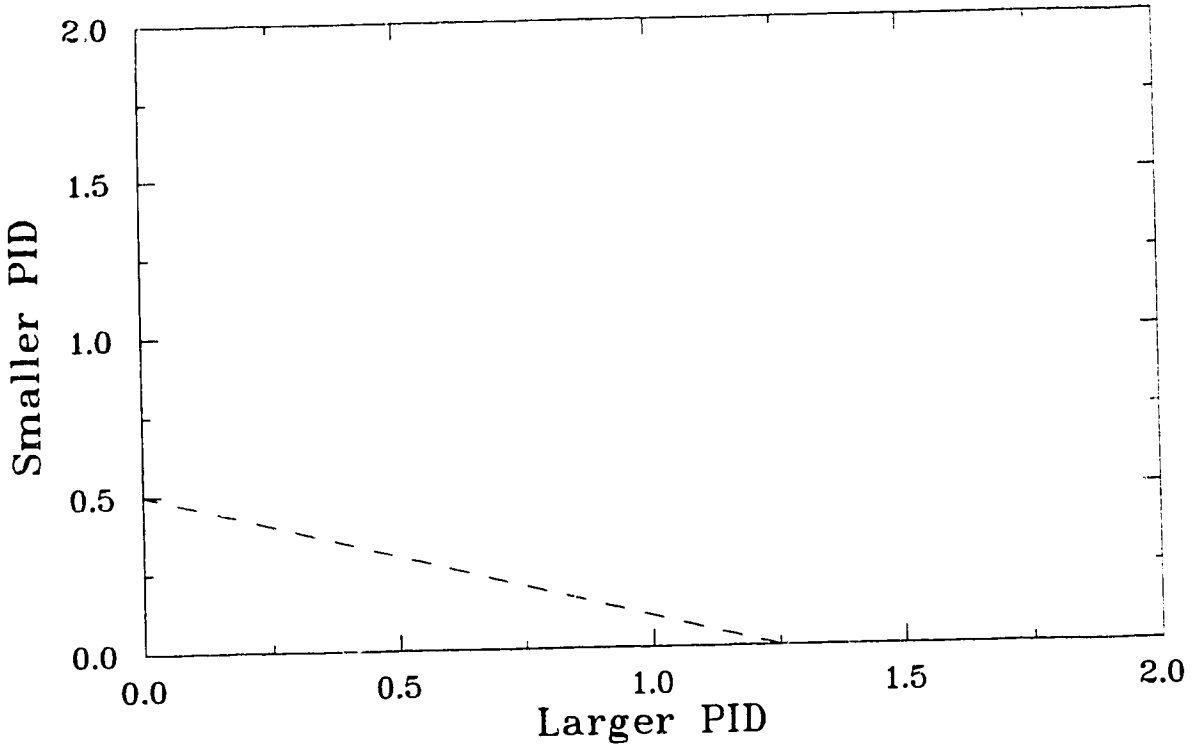
Figure 3.11: Two dimensional histogram of $PID_{greater}$ versus PID_{lesser} after electron events have been cut from the lower left corner. 187,495 events are displayed. Overflows have been suppressed.

PID value appears on the x axis and the smaller PID value on the y axis. Note the large number of e-e coincidences in the bottom left corner. This is a powerful means of rejecting unwanted electrons. The majority of electron tracks occur in coincidence with other electron tracks.

The cut shown in figure 3.10 rejects these electrons leaving only heavier particles such as protons,pions and deuterons. Figure 3.11 shows the same data after the electron cut. We can clearly distinguish three lobes: a large number of proton-proton events centred at (1.0,1.0), proton-pion coincidences centred at (1.0,0.35) and proton-deuteron events at approximately (1.6, 1.0). We see that the pion peak is not truncated by the electron rejection cut.

It is now straightforward to separate the data into the various possible final states

48
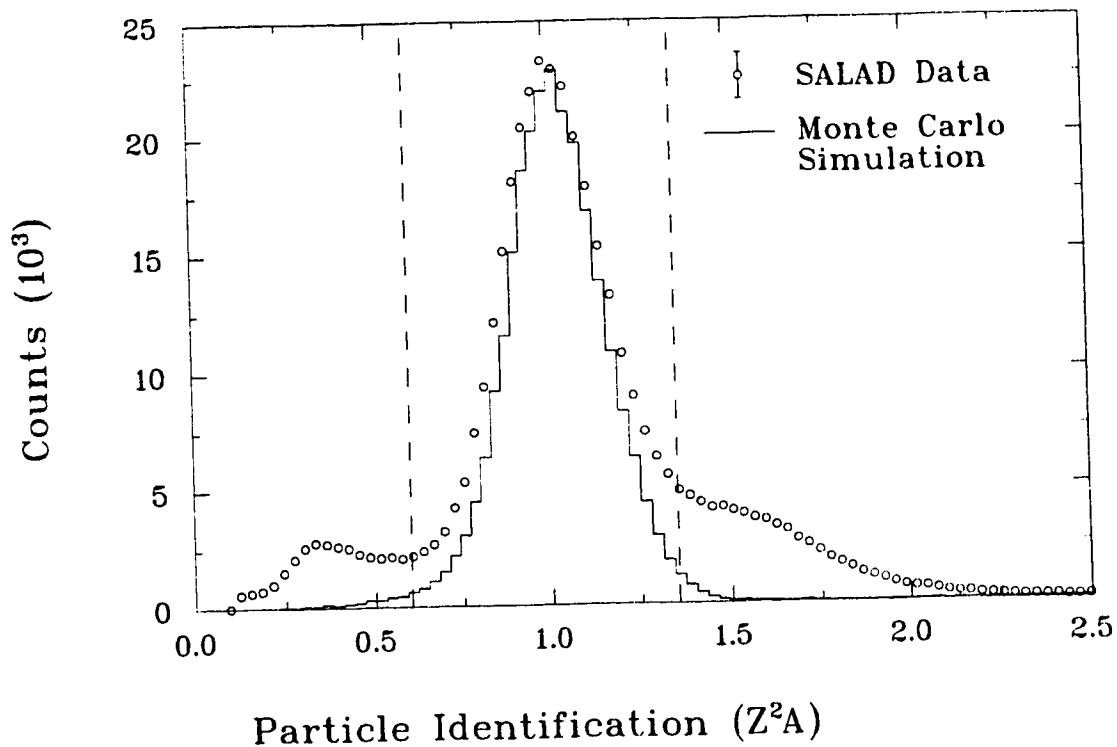
Figure 3.12: Comparison of Particle Identification spectrum for Monte Carlo simulation (solid line) and real data (circles). The real data consists of 395,782 particles from events having identically 2 tracks from a vertex. The horizontal dashed lines show the PID cut for protons.

$A(\gamma,pp)X$, $A(\gamma,p\pi)X$ and $A(\gamma,pd)X$. This is accomplished in the third analysis pass. The separation of particle type is not perfectly clean. A significant contamination of protons may be misidentified as pions or vice-versa. One type of misidentification occurs when protons which are outside the proton PID cut are lost. Figure 3.12 shows the one dimensional PID spectrum of the data of figure 3.11. In addition, the solid histogram shows the PID distribution of simulated protons in the Monte Carlo. The simulation seems to reproduce the width and shape of the proton PID peak quite accurately. Hence the Monte Carlo simulation reproduces the loss of protons beyond the PID cut $(0.60 < PID < 1.35)$ and the calculated efficiency corrects for this loss.

A second correction must be applied for pions and deuterons which are mistakenly
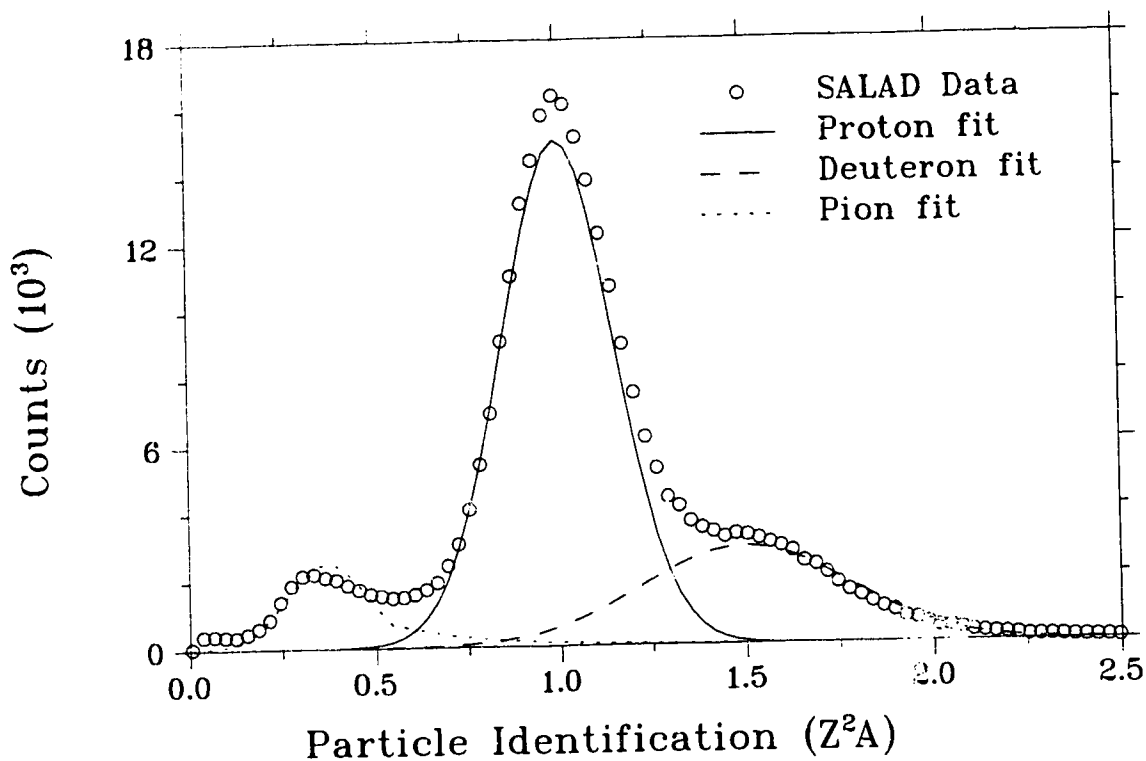
Figure 3.13: Fit of particle identification data for events with two or more tracks from a vertex, after e-e coincidence cut and opening angle < 150° cut. 287,972 particles are histogrammed.

identified as protons. Figure 3.13 demonstrates how this contamin: ion was estimated. It shows a PID plot for the events of figure 3.11 as well as a fit to the data using three gaussian peaks plus an exponential tail for electrons/pion stars. Each function can then be integrated to find the fraction of events misidentified by the PID cuts. The fit gives a 10.7% background from pions and deuterons, inside the proton cut. When identifying two protons in coincidence, the combined probability that either is misidentified is 20.0%. Then 20.0% of events within the proton-proton PID cut are misidentified p-D or p-π events. A correction factor of 0.80 is applied to the number of events identified as 12C(γ,pp)X. The systematic uncertainty in applying this correction is 2.5%.

3.2.3 Tagger TDC and Target cuts

Events from the ^{4}He gas target and the ^{12}C solid targets have been treated equally up to this point. The final step in the analysis is to separate the ^{12}C and ^{4}He data. The Z position of the event vertex (the photon beam defines the Z direction) is shown in the histogram of figure 3.14 for the p-p candidate events of PASS 3. The more dense solid targets are readily visible at Z $\simeq$ 0 and ± 300 mm. Tight cuts were placed on all three peaks to select the events originating in solid targets. Photons reacting with the hydrogen in the polyethylene cannot produce two charged tracks and therefore contribute no background. Though the solid targets have a thickness of 1.58 mm the detector resolutions broaden the peaks in figure 3.14 to $\sigma = 12$ mm. Any loss of candidate events due to the target separation cuts is simulated in the Monte Carlo calculation of detector efficiency as described in section 3.3.3.3. Conversely, a background of ^{4}He(γ,pp) events is present in the ^{12}C data. The contamination can be calculated by assuming a flat background of ^{4}He events underneath the sharp peak of of ^{12}C events. Averaging over the three solid targets, we expect 10% of p-p coincidence events in the solid target region to be background from the of ^{4}He gas. The angular distribution of ^{4}He(γ,pp) events is very similar to the ^{12}C(γ,pp) shape, except for a slight peaking in phi difference at 180° in the helium. A full background subtraction was not made and the final ^{12}C cross sections were corrected by a constant (x 0.91) factor to account for the He background. The systematic error involved in this correction is discussed in section 3.4.

The final step in any tagged photon experiment is a subtraction of random coincidence background. Figure 3.15 shows the time difference spectrum between SALAD triggers and tagger hits.

We see a sharp peak of true coincidences superimposed on a flat background of accidental tagger-SALAD coincidences. These are caused by random hits in the focal plane which happen to coincide with a SALAD trigger as explained in section 2.2.2. This spectrum has been corrected for timing variations in the tagger electronics, for photon time of flight differences along the target and for light propagation time in the scintillator bars.

First a cut is made to select only the events in the prompt peak. Then, an equal area

51
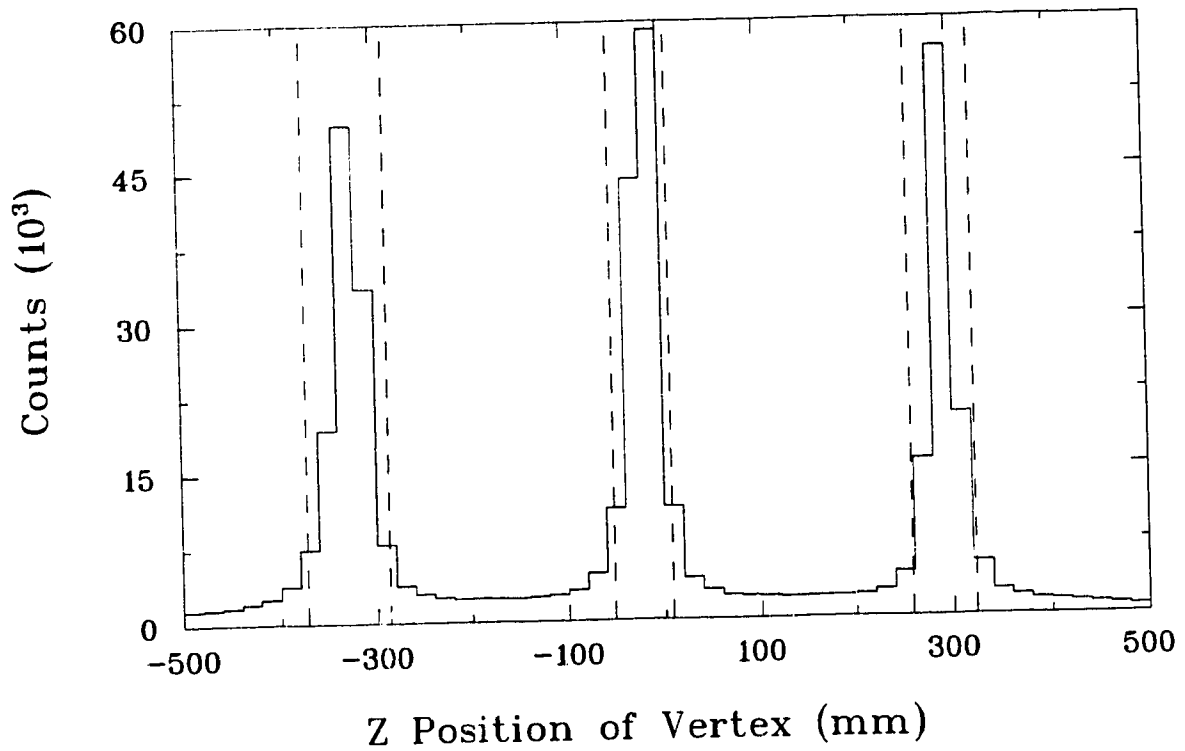
Figure 3.14: Histogram of vertex Z position for events with identically two protons from a vertex. The dashed lines show the cuts used to isolate the 12C targets. 430,015 events are displayed; overflows have been suppressed.

52
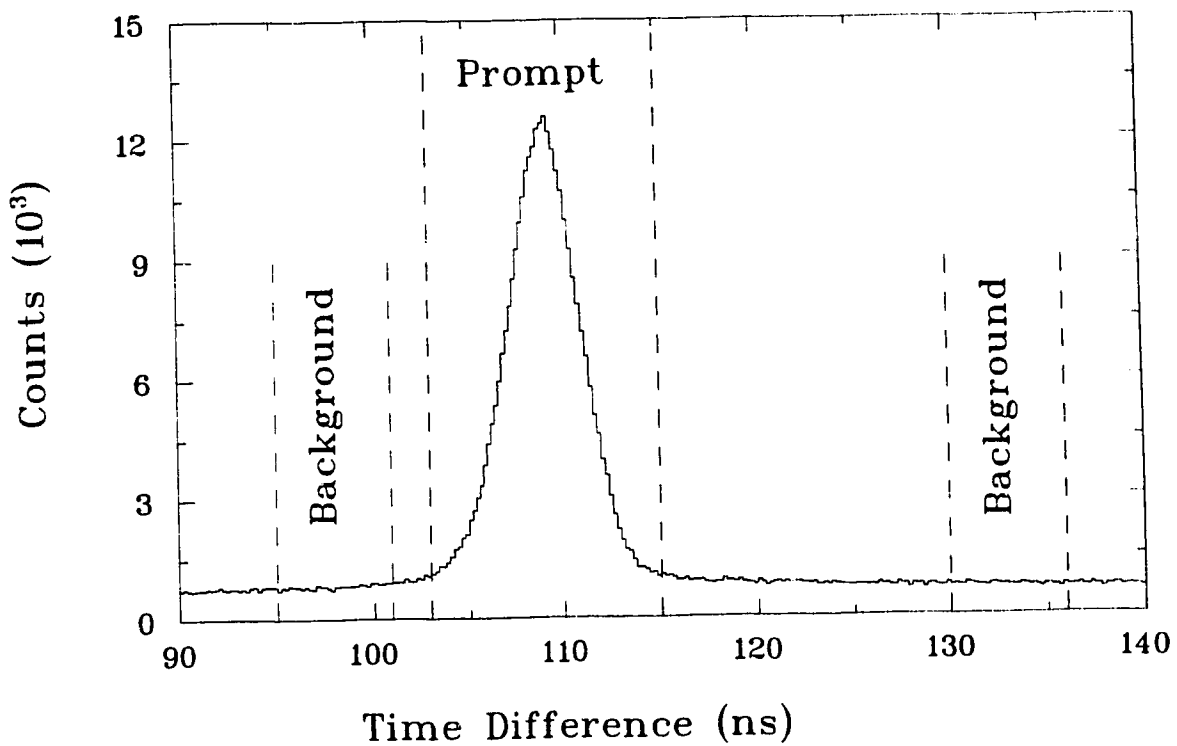
Figure 3.15: TDC time difference for SALAD-tagger coincidences. Events must have identically 2 protons from a vertex located in the 12C target region. 552,160 counts are displayed; overflows have been suppressed. The dashed lines show the prompt TDC cut as well as the two background regions which were subtracted.
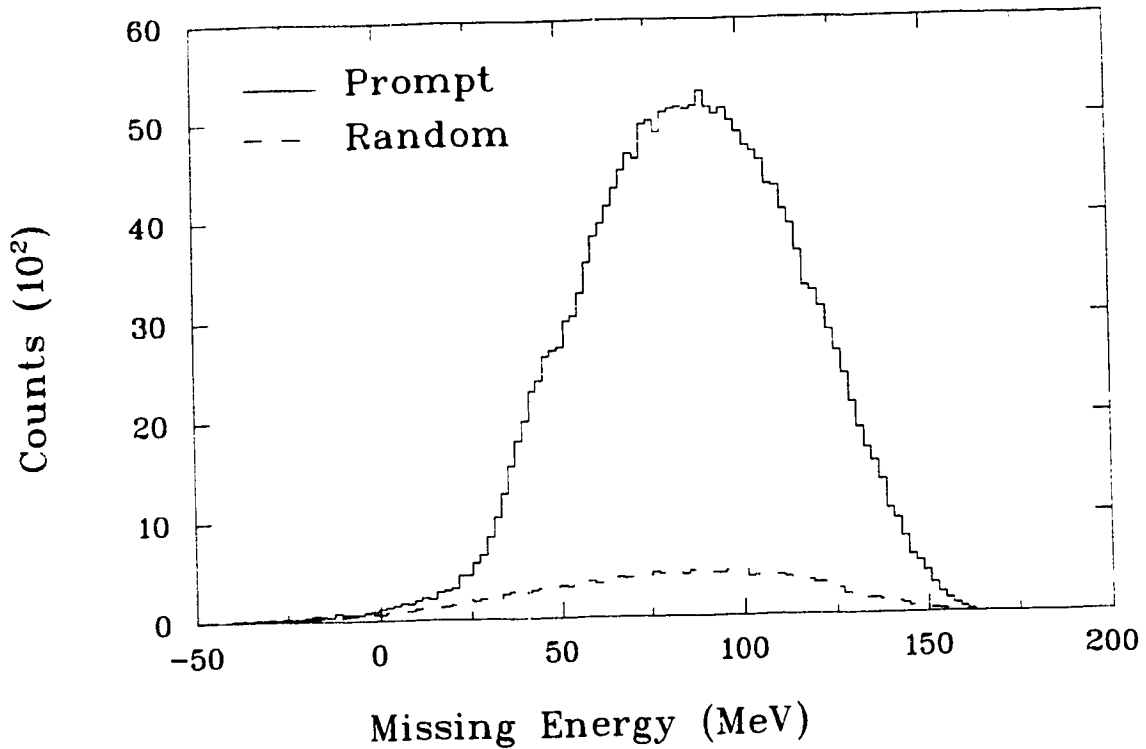
Figure 3.16: Missing Energy spectrum for $^{12}C(\gamma,pp)X$ events (solid line) and random background subtracted (dashed line). The background subtracted yield is 183,212.

of background events are selected from two regions on either side of the prompt peak. These random events are subtracted, bin by bin from the prompt events to produce the final yield histograms. For example, figure 3.16 shows the missing energy distribution of prompt $^{12}C(\gamma,pp)X$ events and the background of random events subtracted.

3.3 Normalization

Once the yield of events for a specific reaction , $N(q_i)$, is known, we can calculate the differential cross section for the reaction with respect to any selected variable, q_j, as

$$\frac{d\sigma}{dq_j}(q_i) = \frac{N(q_i)}{N_I\,N_T\,\epsilon(q_i)\,dq_j}. \tag{3.8}$$

Here, N_I and N_T are the number of incident photons and the number of target nuclei. respectively. The factor $\epsilon(q_i)$ contains the detector acceptance folded with the detector efficiency. The yield, cross section and efficiency are all functions of the kinematic variables, q_i which specify the reaction kinematics.

3.3.1 Photon Flux and Tagging efficiency

The average tagged photon flux through the SALAD detector was $\sim 8.0 \times 10^5$ photons/s. The integrated flux is given by

$$N_I = N_{e^-} \times \epsilon_{tag}, \tag{3.9}$$

where N_{e^-} is the total number of electrons striking the tagger focal plane during the experiment and ϵ_{tag} is the average tagging efficiency (see section 2.2.2) over that period. No correction is required for computer dead time as the scalers which count the focal plane hits are inhibited during dead time. The tagging efficiency can vary slightly over the course of an experiment due to changes in the steering or shape of the electron beam. These variations were accommodated by dividing the data into six periods shown in figure 3.17. A small amount of data collected during period number three was rejected due to poor beam alignment. The photon flux was calculated for the remaining five periods separately and summed together to give the total photon flux for the experiment; $N_I = 4.674 \times 10^{11}$ photons.

In figure 3.18 a), ϵ_{tag} is calculated separately for individual channels in the tagger focal plane, a serious problem becomes apparent. The efficiency for odd channels is systematically higher than that for even numbered channels. This indicates the presence of a background on the tagger focal plane. Any background which is not perpendicular to the focal plane will subtend different solid angles for odd and even channels, giving rise to this asymmetry. This background is present in the tagger channel scalers both during data taking and during tagging efficiency measurements. Provided that the rate of background counts scales with the electron beam current, the asymmetry of the tagging efficiency for odd and even channels will be cancelled by the opposite even-odd asymmetry in the focal plane scalers.

55
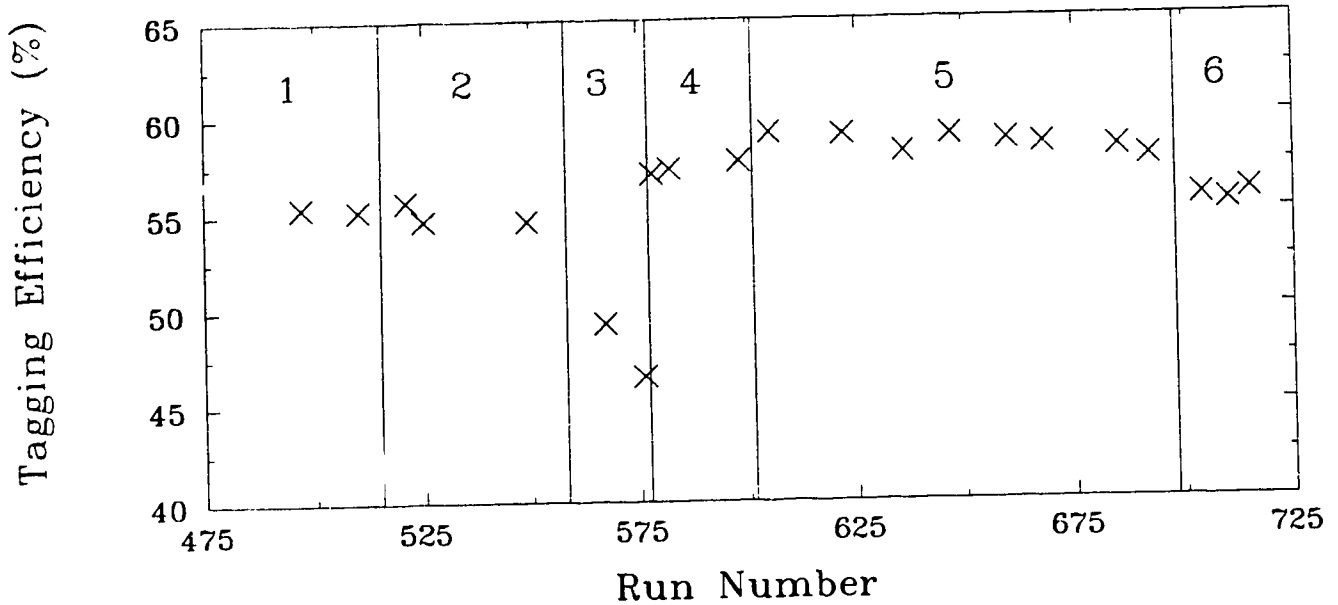
Figure 3.17: Tagging efficiency measurements made during ^{12}C/^{4}He data taking. Errors in tagging efficiency are too small to plot.

Figure 3.18 b) shows a fully normalized differential cross section binned by tagger channel. Here the experimental yield has been divided by the photon flux as well as other factors as given in equation 3.8. We see that the odd-even asymmetry does indeed cancel leaving the cross section a smooth function of channel number (and hence photon energy) as it must be.

The tagging efficiency used for one channel during a given period is the weighted average of the efficiency measurements taken during that period. The efficiency values are weighted according to their statistical errors. The error in the average tagging efficiency values is the standard deviation of the measurements which were averaged. The error in tagger focal plane scalers is negligible hence the error in photon flux (for one channel) is

$$\delta(N_I) = N_I \times \frac{\sigma(\epsilon_{tag})}{\epsilon_{tag}}. \tag{3.10}$$

56
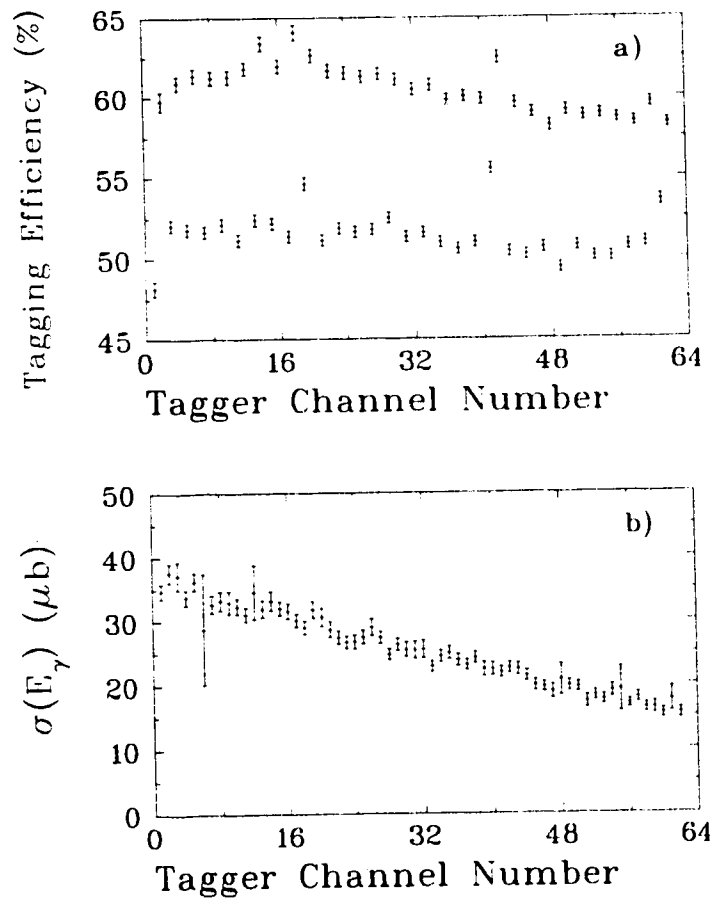
Figure 3.18: The tagging efficiency (a) and cross section (b) as a function of tagger channel.

57

3.3.2 Target Density

The solid targets are made of ultra-high molecular weight polyethylene. They have an average thickness of 1.58 ± 0.01mm and a density of 0.944 ± 0.001 g/cm^3. This gives a carbon target density of

$$N_T^C = 1.92 \times 10^{22} \ \ ^{12}C \ atoms/cm^2. \tag{3.11}$$

The error in target density is dominated by the accuracy of the target thickness and is less than 1% .

3.3.3 Detector Efficiency - The SALAD Monte Carlo Simulation

To obtain a normalized cross section, the observed yield is corrected for both the geometric acceptance and the intrinsic efficiency of the detector. In an experiment using discrete detectors, these two factors can be determined independently. The geometric acceptance is simply the solid angle subtended by the detector. The intrinsic efficiency can be measured as a function of particle type and energy.

In a large acceptance detector like SALAD, geometric acceptance and intrinsic efficiency are fundamentally linked. The angular acceptance of SALAD is fixed by the length of the wire chambers. This acceptance then depends on the Z position of the event vertex in the target. Identical particles with the same kinetic energy deposit very different amounts of energy in the calorimeter at different θ angles. The detection threshold must then be calculated as a function of particle type, energy and θ angle. Even the more subtle effect of detector resolutions on efficiency is strongly dependent on the energy and angle of the particle. An analytic calculation of detector efficiency is therefore intractable.

In equation 3.8, $\epsilon(q_i)$ is the convolution of the intrinsic efficiency and the geometric acceptance of the SALAD detector. It is usually referred to simply as the efficiency and is calculated using a Monte Carlo simulation of the detector. The technique is straightforward. First, events are generated which satisfy the kinematics for the desired reaction. Then the detector response to these events is simulated. Finally the *simulated* data is analyzed and the detector efficiency is calculated as the ratio of detected events

to generated events. Provided that the Monte Carlo simulation faithfully reproduces detector response, the calculated efficiency, $\epsilon(q_i)$, is accurate.

3.3.3.1 Input Distribution

We need to calculate the efficiency for SALAD to detect two protons in coincidence. The efficiency depends on the energies E_1 and E_2 of the two protons as well as their angles θ_1, θ_2, ϕ_1 and ϕ_2, in the SALAD coordinate system. If we integrate over ϕ_1 or ϕ_2, no information is lost, as long as the target and beam are not polarized. We can then specify the kinematics of the two protons with five variables:

$$\epsilon(q_i) = \epsilon(E_1, E_2, cos(\theta_1), cos(\theta_2), \Delta\phi).$$
(3.12)

Here, E_1 and E_2 are the kinetic energies of the protons. Choosing $cos(\theta_i)$ instead of θ_i ensures that equal width bins subtend equal solid angles. Having integrated over one of the phi angles, we choose to specify the remaining phi angle in terms of the smallest phi difference between the two protons, $\Delta\phi \equiv |\phi_1 - \phi_2|$. This demonstrates that the choice of variables is not unique; in fact we could have chosen any five independent variables which specify the kinematics of the two protons.

As stated in the introduction to this section, the event vertex position inside the target (particularly the the Z position) strongly affects the angular acceptance. The three solid targets will then have different efficiencies. $\epsilon(q_i)$ is calculated separately for each target, effectively adding a sixth variable.

The $^{12}C(\gamma,pp)X$ data are only semi-exclusive as the residual X may not be bound. Observed two-proton events may include events in which X consists of a residual nucleus plus one or more free protons or neutrons. Only if X = ^{10}Be in its ground state do we have complete kinematics. Each additional particle adds three more independent variables. By not specifying these variables, we are implicitly integrating over a distribution of energies and angles for the unseen particles.

When generating simulated data for the efficiency calculation then, it is important to include some 2p-1n and 2p-2n events with reasonable distributions of neutron energy and angle. The CERN library routine GENBOD [Ja75] was used to generate proper phase

59

space distributions for the three reaction channels listed above. Including additional neutrons beyond the 2p-2n case has little effect on the phase space distribution. The most dramatic difference among the three channels occurs when we compare the missing energy distributions, $E_{miss} = E_\gamma - E_1 - E_2$. Figure 3.19 a) shows the missing energy distribution for three-body (2p), four-body (2p-1n) and five-body (2p-2n) distributions. A fit was performed to the experimental data using these three curves. The best fit was obtained for the combination of :

- 13% 2p,

- 57% 2p-1n,

- 30% 2p-2n .

This mixture was used as the best estimate of the actual kinematic distribution. True, the addition of even simple physics inputs (a matrix element which is not constant) might bring the estimate closer to reality but the simple model chosen has the advantage of being easily reproduced in the future. The above phase space distribution reproduces the shape of the missing energy yield quite well, except at small missing energy values. Though the phase space distribution of $d\sigma / dT_m$ (solid line in fig. 3.19 b)) seems to drop to zero below $T_m = 40$ MeV, it is actually non-zero but very small down to $T_m = 30$ MeV. Hence, it is possible but unlikely that a large matrix element for the range 30 MeV $< T_m <$ 40 MeV, could bring the two distributions into better agreement.

The distribution is now binned in the five selected variables E_1, E_2, $\cos(\theta_1)$, $\cos(\theta_2)$ and $\Delta\phi$. The range of each variable was divided into ten bins, giving an energy bin width of 17 MeV, $\cos(\theta)$ width of 0.2 and an 18° wide $\Delta\phi$ bin. Detector resolutions permit a considerably smaller bin size than this. however the size of the resulting five dimensional matrix is the limiting factor. One hundred Monte Carlo events were generated for each of the 10^5 bins of the efficiency matrix. Within the bins these one hundred events were given a random distribution. The shape of the distribution is preserved by assigning an event weight. A separate matrix was generated for each of the three solid targets.
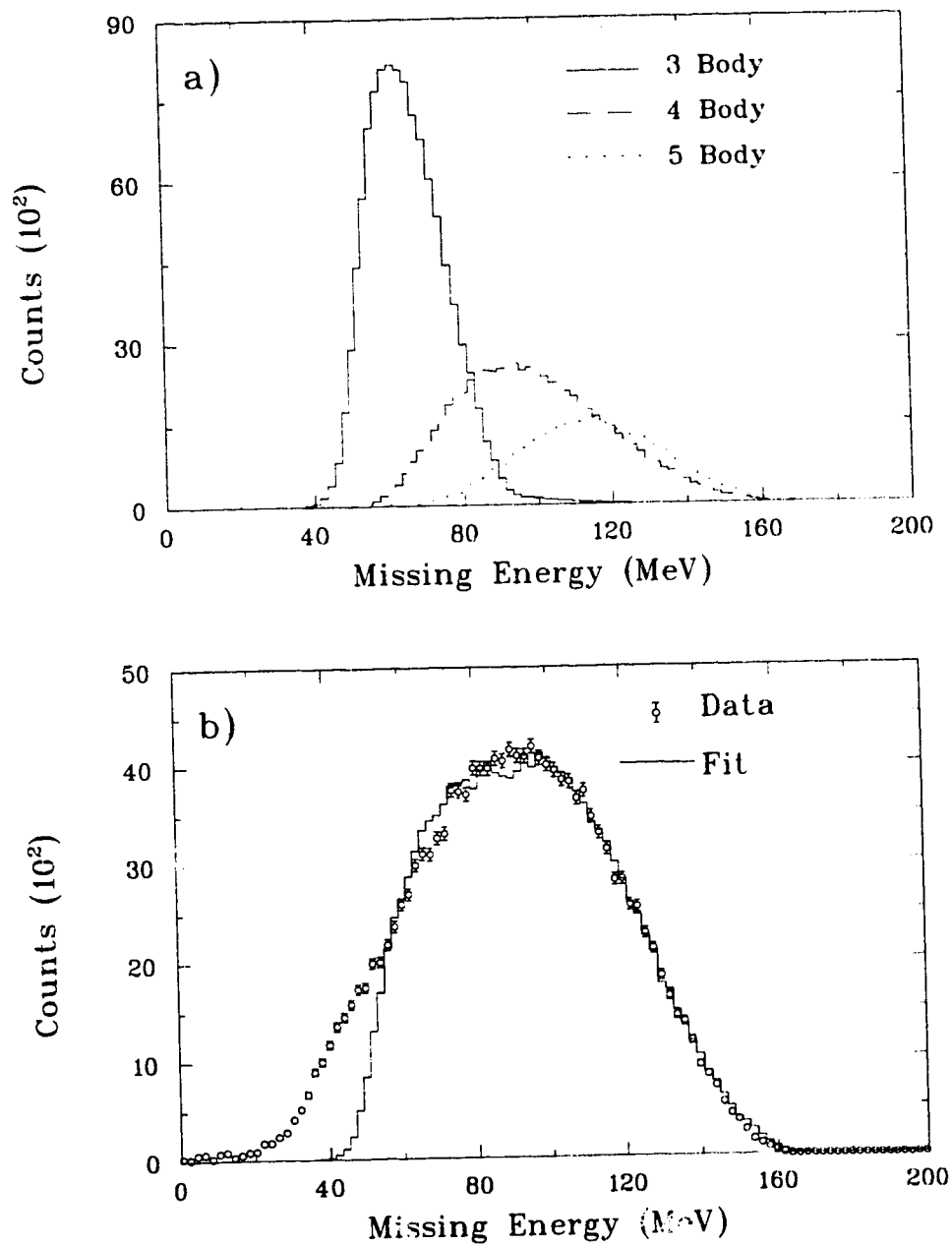
Figure 3.19: Figure a) shows the missing energy distributions for Monte Carlo simulations of 2p (solid line), 2p-1n (dashed line) and 2p-2n (dotted line) kinematics, normalized to the same number of generated events. Figure b) shows a fit of the above three distributions to the missing energy yield for 12C(γ,pp)X events.

61

3.3.3.2 Modeling Detector Response

The task of the Monte Carlo simulation is to take the events of the input distribution and by applying detector thresholds, efficiencies and smearing due to resolution, reproduce the yield seen in the actual SALAD. In order to do this it must correctly model the fundamental resolutions of the SALAD detector.

The tracking accuracy of the SALAD wire chambers is determined fundamentally by the Z position resolution of the individual wires. This Z resolution is determined from source calibration runs as described in section 2.4.2. The Monte Carlo uses a resolution which varies from $\sigma(Z) = 4$ mm at $Z = 0$ up to $\sigma(Z) = 9$ mm near the ends of the wire. This value has been adjusted to reproduce the observed tracking resolutions. The divergence of the photon beam is calculated from the collimator sizes and separations and is used to generate the radial distribution (X and Y coordinates) of event vertices.

The efficiency of the wire chambers is another important input to the Monte Carlo. The relative efficiency of a given wire can be determined by looking at how often it is present in valid tracks. We use three of the cylindrical wire chambers to define a valid track and determine which cell it intersects in the remaining chamber. The number of ADC hits present in this cell then determines the efficiency of the cell *relative* to its neighbouring cells. This calculation is repeated for each wire cell in each of the four chambers. It is then possible to combine the information in these relative efficiencies to extract *absolute* efficiencies for each of the 216 wires in SALAD. These absolute efficiencies are input to the Monte Carlo simulation and used to determine which wire chamber ADC's will fire for a given event. Bad wires which produce no signal or unreliable signals are given zero efficiency and are not used in the analysis.

The next step in the simulation is to model the calorimeter response. The energy deposited as a particle passes through each element of the detector is carefully calculated. The energy loss code and tables are the same ones used in the data analysis program where the process is reversed to reconstruct the particles vertex energy. Once the theoretical energy deposition has been calculated in both the E and Δ E scintillators, several corrections must be applied.

First, there is the possibility that a particle passing through a scintillator will un-
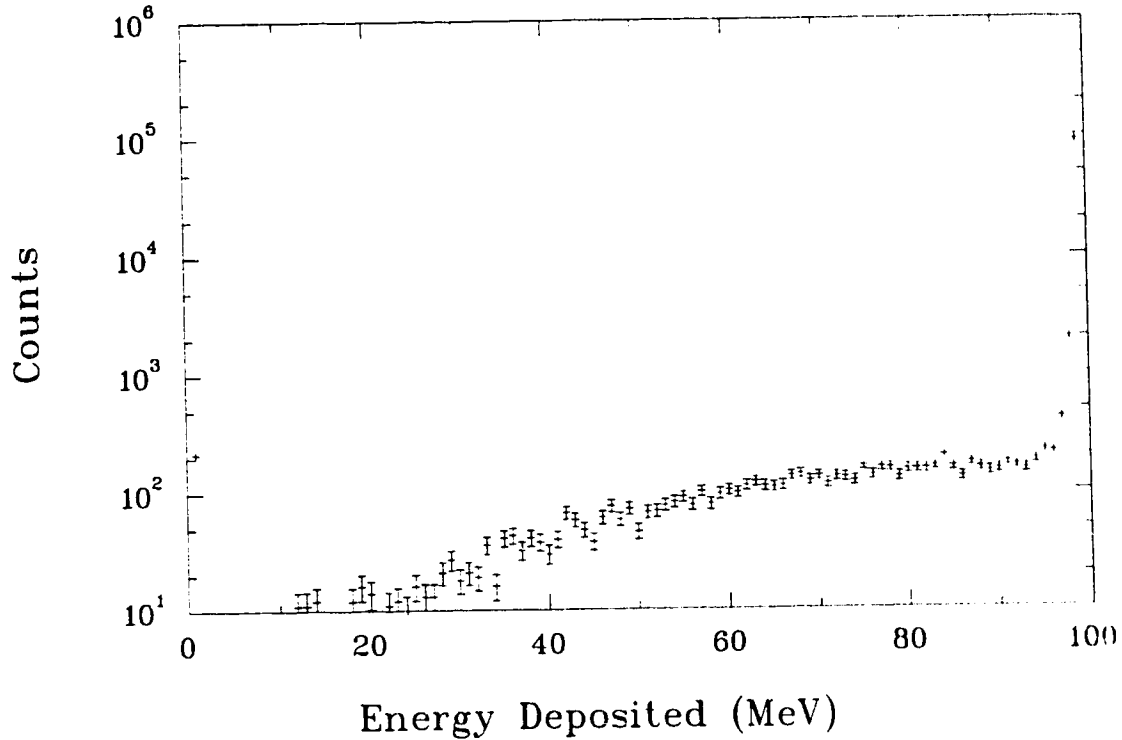
Figure 3.20: Distribution of observed energy deposition for a 100 MeV proton incident on a scintillator. The histogram shows the result of a GEANT simulation for 100,000 protons.

dergo a nuclear reaction. This process was discussed in section 2.4.3.1. The process has been modelled using a GEANT Monte Carlo simulation with the GHEISHA hadronic interactions package [Ca87]. The result of this simulation is a number of distributions which give the observed energy (after reaction losses) for protons of a given incident energy. Figure 3.20 shows such a distribution for protons with kinetic energy $E_p = 100$ MeV as they enter the scintillator. Note that only about 8% of the protons deposit less than 97% of their actual energy. A log scale was necessary to show the tail of protons which deposit less than their full energy. At $E_p = 150$ MeV the fraction of protons affected rises to approximately 20% . An energy loss is randomly selected according to these distributions and subtracted from the theoretical energy loss. The reaction loss correction is only applied to the E scintillators as particles stopping in the Δ E

scintillator are excluded from the analysis.

The next step is to simulate the light output of the scintillator for the given energy deposition. It is important to correct for saturation effects for low energy particles as described in section 2.4.3.1. Again the Monte Carlo simulation uses the same tables as the analysis code to convert energy deposition to scintillator light output. Using the known scintillator gains and the scintillator resolutions described in section 2.4.3.1, the phototube ADC outputs are calculated and stored.

Finally, the simulation tests whether each event satisfies the SALAD trigger conditions as outlined in section 2.11. Both a simple threshold on the ΔE ADC values and the sum threshold on the sum of E and ΔE ADC's for a telescope must be satisfied. The threshold value for each of the 24 telescopes and each of the 48 ΔE ADC's was determined from raw ADC plots and input to the Monte Carlo simulation. The Monte Carlo generates simulated SALAD wire chamber and scintillator hits and then writes out a simulated data file to read by the data analysis code. All generated events are written to the file but those which fail the threshold or acceptance tests have zeroed ADC values.

3.3.3.3 Efficiency Calculation

The Monte Carlo simulated data file is now read and analyzed using the exact same analysis code as for the real SALAD data. The only difference in the analysis is that all Monte Carlo events are assumed to be in coincidence with the photon tagger. The response of the focal plane detector is not modeled in the Monte Carlo simulation so no tagger TDC cut or random background subtraction is performed on the Monte Carlo data.

Once the analysis cuts have been applied, the detected $^{12}C(\gamma, pp)X$ events are binned according to the five kinematic variables of in a 10^5 element matrix. Likewise, all original events generated by the Monte Carlo simulation are binned in a 10^5 element matrix. The detector efficiency is simply the bin by bin ratio of detected events over generated events.

$$\epsilon(q_i) = \frac{Y_{DET}(q_i)}{Y_{GEN}(q_i)}. \tag{3.13}$$
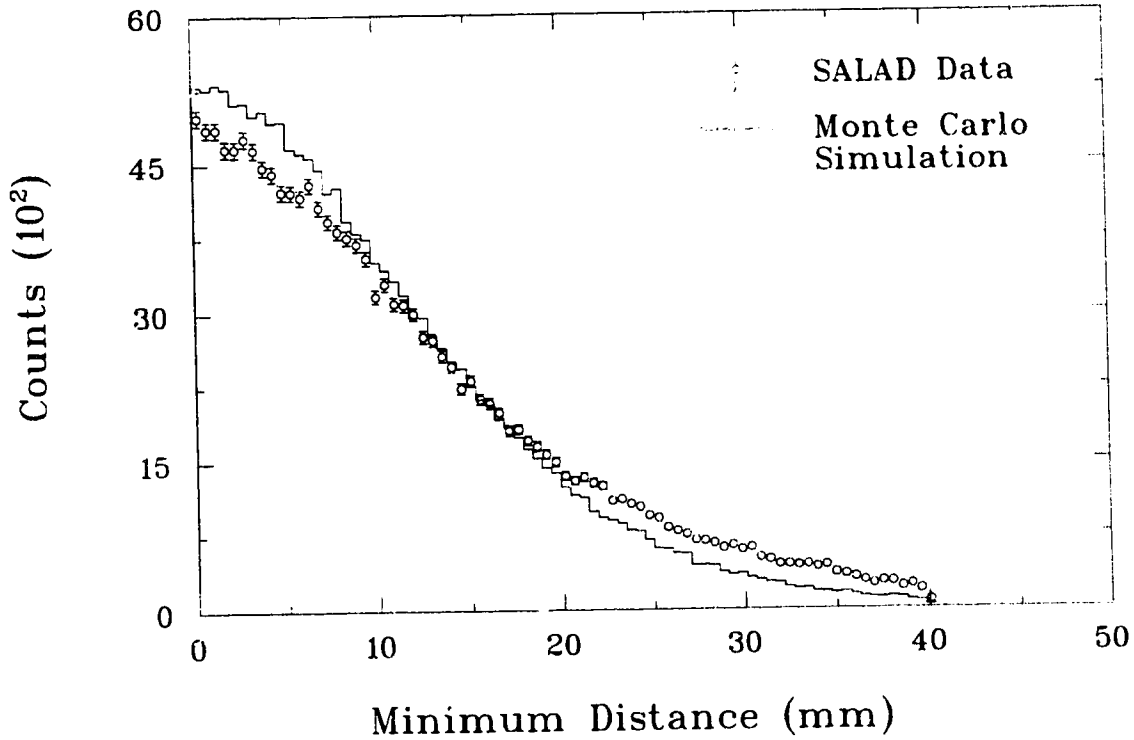
Figure 3.21: Comparison of minimum distance distribution for Monte Carlo and real data. The following cuts were used to select the 155,321 events displayed: identically 2 protons from a vertex, opening angle $< 150°$ and tagger TDC prompt events minus random background. The Monte Carlo simulated data has the same cuts and equal statistical errors.

The five-fold differential cross section is then calculated as

$$\frac{d^5\sigma}{dE_1 dE_2 dcos(\theta_1)dcos(\theta_2)d\Delta\phi} = \frac{N(E_1, E_2, cos(\theta_1), cos(\theta_2), \Delta\phi)}{N_I \; N_T \; \epsilon(E_1, E_2, cos(\theta_1), cos(\theta_2), \Delta\phi, Z_{targ}) \; (\Pi_j \Delta q_j)}.$$

In the following chapter we compare the differential cross section to a theoretical calculation.

The true test of the Monte Carlo simulation code is whether the simulated yield reproduces the observed yield of the SALAD detector. Figure 3.21 compares the minimum distance distributions for real data (experimental points) and the Monte Carlo simulation (histogram). Recall that the minimum distance is the distance of closest
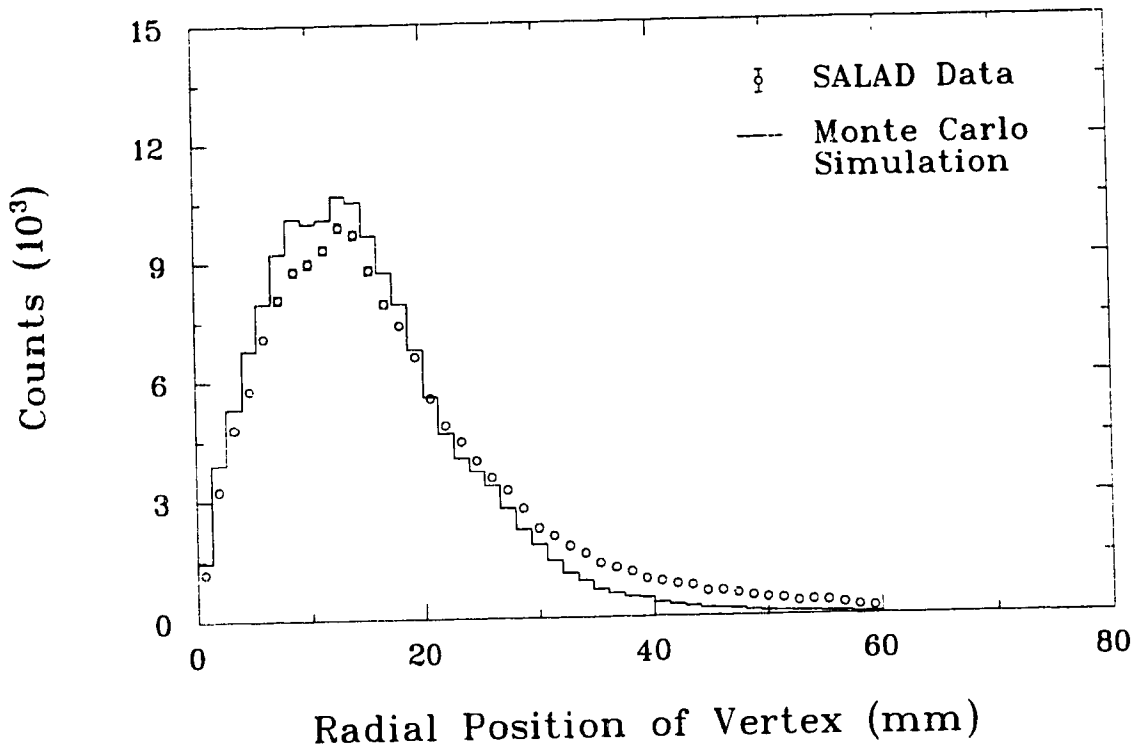
Figure 3.22: Comparison of radius of vertex distribution for Monte Carlo and real data. The same 155,321 events are shown as in figure 3.21.

approach of two tracks and is used to define an event vertex. The agreement between data and Monte Carlo is reasonable. Note that requiring a good vertex and identifying protons by PID cleans up the distribution considerably compared to the raw spectrum of figure 3.5. The discrepancy at large distances can be explained by a small electron background still present in the data. Background electrons are not modeled in the Monte Carlo simulation. Due to their small charge deposition in the wire chambers, the tracking resolution for electrons is somewhat worse than that for protons. Hence one would expect to find more electrons than protons at large values of minimum distance.

Figure 3.22 compares data to Monte Carlo simulation for the radial position of the event vertex. The width of of the distribution is well reproduced, giving confidence in the wire chamber resolutions and beam divergence input to the Monte Carlo. Again the large discrepancy at large radius values is probably due to backgrounds which are

present in the data but not in the Monte Carlo calculation.

It is more difficult to check the modeling of SALAD's energy resolution. There is no sharp feature in the energy spectrum since the experiment is not kinematically complete. It is interesting, however, to see how a complicated quantity like PID (linearized stopping power) is reproduced. Figure 3.12 shows the PID spectrum of two track events from a vertex, after a cut has been applied to reject electron-electron events. The Monte Carlo spectrum (solid line) contains only protons but it reproduces the shape and width of the proton peak at PID = 1.0 . The additional peaks in the data are due to pions at PID = 0.35 and poorly resolved deuterons at PID = 1.6. Any error in modelling scintillator energy resolutions would destroy this good agreement.

3.4 Systematic Errors

In calculating normalized cross sections according to

$$\frac{d\sigma}{dq_j}(q_i) = \frac{N(q_i)}{N_I \, N_T \, \epsilon(q_i) \, dq_j},\qquad (3.14)$$

we must quantify any systematic errors for which we cannot correct. Each term in the above equation contributes some degree of systematic error. The systematic errors in photon flux (N_I) and target density (N_T) were discussed in the first two subsections of this section. They are 2% and 1% respectively.

The yield, $N(q)$, is dominated by statistical error which is treated separately but also contains some significant systematic errors. Misidentification of particle type using PID was discussed in section 3.2.2 and contributes a 2.5% systematic error. Similarly there is a contamination of $^4\text{He}(\gamma,pp)X$ in the ^{12}C data set. A simple correction factor of 0.91 was calculated in section 3.2 3. If the angular distribution of the ^4He events is very different from the ^{12}C p-p events, they could introduce significant error. We estimate a systematic error of 2% due to ^4He background events.

The solid targets used pose a special problem to energy loss calculation. Though real events will occur at random depth throughout the target, the Z vertex position resolution is too poor to give any information. In analyzing the data, we must assume that all events originate in the centre of the solid target. For particles near $\theta = 90°$, this

Source of error	contribution
Tagging efficiency	2 %
Target density	1%
Particle identification	2.5%
^{4}He background	2%
Target E loss	2%
Tracking efficiency	5%
Total (i quadrature)	7%

Table 3.6: Contributions t systematic error

can cause errors of up to 20% in reconstructed vertex energy. This effect is accurately modeled in the Monte Carlo simulation, reproducing the sharp rise in energy threshold for protons near $\theta = 90°$. A systematic error of 2% is assigned for errors in modeling solid target energy loss.

Finally, the efficiency, $\epsilon(q_i)$ contributes to the systematic error. The failure of the Monte Carlo simulation to reproduce the minimum distance and radius of vertex distributions exactly (see figures 3.21 and 3.22) is likely the result of systematic error in modelling the tracking. $\epsilon(q_i)$ is sensitive to small changes in the wire chamber efficiencies. Even a small contamination of electrons in the data used to determine wire efficiencies will artificially depress the calculated efficiency. In a previous SALAD experiment a systematic error of 9.9% was assigned for tracking efficiency [Ko94]. At the time of this experiment only three of the four wire chambers were functioning, greatly increasing the uncertainty in determining wire efficiencies. For the present experiment, all four wire chambers were used and we estimate a systematic error of 5% is realistic.

Table 3.6 summarizes the contributions to systematic error. The errors are combined in quadrature to give a total systematic error of 7%.

Chapter 4

Results and Discussion

4.1 Description of Calculation

4.1.1 The Theoretical Model

Results from a recent calculation by R.C. Carrasco et al. [Ca94] are compared to the ^{12}C(γ,pp)X data. This particular theoretical treatment has the advantage of separability of the contributions from different reaction channels. In addition, final state interactions are accurately treated with a Monte Carlo technique which makes it easier to apply experimental energy thresholds to the calculated cross sections.

Calculating the ^{12}C(γ,pp)X cross section is complicated due to the many different reaction channels which can contribute. The data are inclusive with respect to undetected protons, neutrons, or other charged particles which were outside the detector acceptance or below threshold. In additic to direct absorption on two or more nucleons, pion photoproduction can also produce a two proton final state. A pion produced in the nucleus has a large probability of being scattered or absorbed, exciting more nucleons. In addition any nucleons produced are subject to rescattering which will alter their energy and angular distribution and may excite and emit other nucleons. A full quantum mechanical treatment of these processes is intractable.

traditional approach is the Monte Carlo intranuclear cascade calculation. Here reac on probabilities for photons, pions and nucleons are taken from ('ementary exper-

69

imental cross sections or simple parameterizations. Final state interactions are modeled by a Monte Carlo technique.

A new approach, described by Carrasco et al. [Car92] combines this Monte Carlo treatment of final state interactions with a true microscopic calculation of elementary processes. The most significant improvement is the inclusion of medium renormalization effects inside the nucleus. Carrasco [Car92] gives a full description of the microscopic calculation of the total photon absorption cross section. The approach is to construct the photon self-energy, $\Pi(k, \rho)$, in nuclear matter, where k is the photon energy and ρ the nuclear density. The inputs are the basic couplings of the γ, π and ρ to nucleons and Δ's. An effective spin-isospin interaction is built by adding up p-h and Δ-h contributions in a random phase approximation. The effect of π and ρ exchange is included. Short range correlations are included as explained further in section 4.4.4.

The local density approximation (LDA) is taken, $\rho \rightarrow \rho(r)$, such that σ_{total} can be calculated for any medium or heavy nucleus by simply supplying $\rho(r)$. The LDA ignores the finite range of the interaction but this is shown to be a valid approximation for the weak photonuclear coupling.

The total photonuclear cross section can then be obtained by integrating the imaginary part of the photon self energy

$$\sigma_A = -\int d^3r \frac{1}{k} Im\{\Pi(k, \rho(r))\} \tag{4.1}$$

The integral is evaluated using Cutkosky rules which allow a clear separation of contributions from the (γ, π), (γ, NN) and $(\gamma, 3N)$ absorption processes.

After the primary photon interaction, excited nucleons and pions are propagated as classical particles. At each Monte Carlo step, the reaction probability is evaluated and further nucleons may be excited via pion absorption, pion scattering or N-N scattering. The reaction probabilities are taken from a full quantum mechanical many-body calculation. The calculation for pions [Sa88] was tested against data [Car92a]. The NN rescattering potential is derived from a parameterization of the elastic NN differential cross section which is modified to include the important effects of Pauli blocking, Fermi motion and medium renormalization in the nucleus.

70

One limitation which is significant for the SALAD data is the nucleon energy threshold. The minimum proton energy threshold in SALAD is 28 MeV. The MC propagation of nucleons induces large uncertainty for low momentum particles [Sa88]. This imposes a minimum proton vertex energy for reliable FSI calculation. A previous calculation [Car92] imposes a cutoff energy of 40 MeV but these calculations have been modified to use a cutoff of 28 MeV, which is the minimum reasonable value [Ca93].

4.1.2 Comparison to Data

The above calculation produces the five-fold differential cross section,

$$d^5\sigma \equiv \frac{d^5\sigma}{dE_1 dE_2 dcos(\theta_1)dcos(\theta_2)d(\Delta\phi)} \tag{4.2}$$

Actually the calculated cross section would be a function of eight variables for a four-body final state, a function of eleven variables for a five-body final state and so on. Binning the results only in the five variables shown above is consistent with the experimental situation in which two protons are detected. We then obtain an inclusive differential cross section for $^{12}C(\gamma,pp)X$ which is integrated over any additional particles emitted and can be compared to the SALAD data.

Before comparing data and theory the results of the calculation must be modified to reflect the angular acceptance and the energy threshold of the SALAD detector. This is accomplished by setting the calculated cross section to zero in any bin where the efficiency of the SALAD detector, $\epsilon(E_1, E_2, cos(\theta_1), cos(\theta_2), \Delta\phi)$, is identically zero. In this way the theoretical calculation is limited to the same acceptance as the SALAD detector.

Finally the photon energy dependence of the data was investigated. The data were sorted into four bins with central photon energies of 192, 203, 213 and 223 MeV. Figure 4.1 shows the cross section differential with proton kinetic energy for the four different energy bins. There is no significant change in the shape of the distribution and only the expected increase in size with increasing photon energy. The other normalized one-fold and two-fold differential cross sections showed no significant variation with photon energy. Therefore the data have been summed over the full range of photon energies from $187\ \text{MeV} < E_\gamma < 227\ \text{MeV}$.

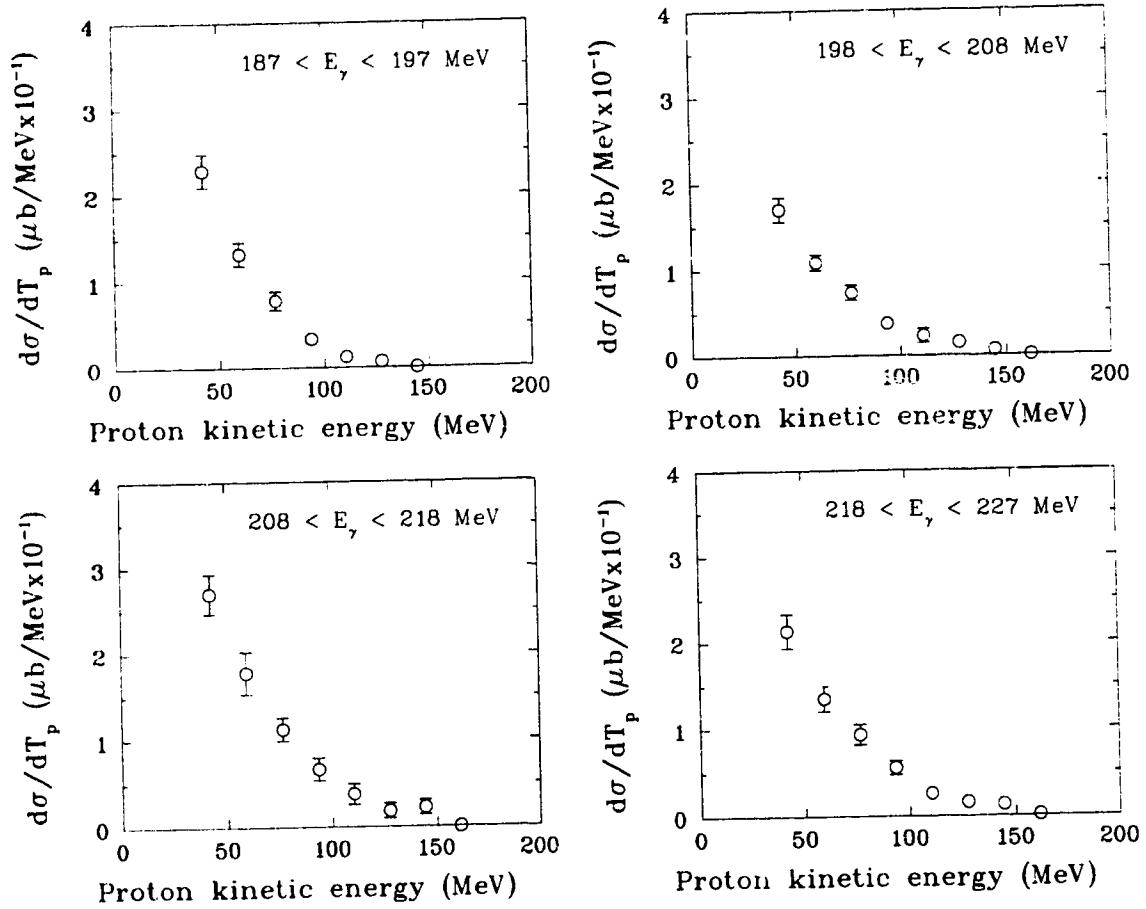Figure 4.1: Comparison of differential cross section as a function of proton kinetic energy for different ranges of photon energy. The four plots display a total yield of 140,244 events which have identically 2 protons from a vertex, opening angle $< 150°$ and $T_p > 34$ MeV. TDC random background has been subtracted. The error bars include statistical error plus the error in detector efficiency.

The error in $d\sigma/dT_p$ is the statistical error in the yield added in quadrature with the error in detector efficiency. An additional systematic error of 7% is described in section 3.4.

4.2 Comparison to Previous Experiments

There are only two previous experiments [Ka87, Ar80] which have measured two proton emission cross sections for this region of photon energy. Both of these experiments used discrete detectors in coplanar kinematics. The more recent experiment [Ka87] has a statistical error of 30% and limited overlap with SALAD measurements. Cuts were placed on the SALAD data to mimic the acceptance and energy thresholds of Kanazawa's experiment. The quantity which can be compared to the SALAD results is $d\sigma/d\Omega$ for $\theta_p = 30°$ with the requirement that a second proton be detected in coincidence. Kanazawa's result is $d\sigma/d\Omega = 3.1 \pm 0.9$ μb/sr while the SALAD result is $d\sigma/d\Omega = 3.5 \pm 0.4$ μb/sr, where the errors are statistical only. There is agreement but the size of the statistical error weakens the comparison.

The earlier experiment by Arends et al. [Ar80] has much smaller statistical error but integrates over a much larger range in photon energy, 200 MeV $< E_\gamma < 385$ MeV. In order to make a comparison to the Arends data [Ar80] the SALAD data must be extrapolated over a large range of photon energies. The behaviour of $d\sigma/dE_\gamma$ for $^{12}C(\gamma,pp)X$ over the Δ resonance region is quite difficult to predict. The systematic error in such an extrapolation is so large that a comparison is not worthwhile.

4.3 Comparison to Theory

4.3.1 One-dimensional Integrated Cross Sections

The difficulty in presenting a five-fold differential cross section is the inability to plot more than two dimensions at once. It is perhaps easiest to begin examining this quantity, $d^5\sigma$, by integrating over four variables to obtain one dimensional plots of $d\sigma/dX$ where X can be any variable describing the system.

73

Figure 4.2 a) shows $d\sigma/dT_p$, the differential cross section with respect to proton kinetic energy. It is immediately apparent that the calculation predicts a much higher cross section than the data for 18, MeV $< E_\gamma < 227$ MeV. Integrating the two curves one obtains a total cross section of 24.5 ±0.1 μbarns for the data and 95.8 ±0.1 μbarns for the calculation; a factor of 3.9 discrepancy. The minimum proton energy threshold for the SALAD detector is $T_p = 28$ MeV. To avoid sensitivity to the precise placement of the threshold, a software threshold has been applied at $T_p = 34$ MeV.

Figures 4.2 b), c) and d) show similar differential cross sections for cosine of proton angle (θ_p), cosine of the opening angle between the two protons (θ_{op}) and phi difference between the two protons ($\Delta\phi$). Though the difference in normalization is apparent, it is interesting to compare the shape of the data distribution to the calculation. In figure 4.3 a) through d), the same four cross sections from figure 4.2 are shown but the normalizations are matched by dividing the calculation by 3.9. The agreement is excellent for the angular distributions in $\cos(\theta_{op})$ and $\Delta\phi$. The dip in $d\sigma/\ d\Delta\phi$ near $\Delta\phi = 180°$ is caused by the cut, $\theta_{op} < 150°$, placed on the data. This acceptance limit has been applied to the calculation, which then reproduces the shape of the data distribution. The shapes of the $d\sigma/\ dT_p$ and $d\sigma/\ d\cos(\theta_p)$ in figures 4.3 a) and b), give reasonable agreement.

The good agreement obtained by scaling by a constant factor, points to a normalization error in the data. Other evidence weighs against this simple solution. Previous SALAD experiments have reproduced known cross sections using the same Monte Carlo method to calculate detector efficiency [Ko94]. Both the ^{3}He(γ,pd) and the well known D(γ,pn) cross sections are reproduced to within 10%.

The SALAD ^{12}C(γ,pp)X cross section agrees with a previous experiment [Ka87] (see section section 4.2) but large statistical errors make this agreement approximate and the comparison can only be made over a small fraction of phase space.

In order to gain insight into the mechanisms responsible for two proton emission, it is useful to calculate the missing energy,

$$T_M \equiv T_\gamma - T_p^1 - T_p^2 \qquad (4.3)$$

where T_γ is the photon kinetic energy and T_p^1 and T_p^2 are the kinetic energies of the two

74

Figure 4.2: Comparison of differential cross section data for $^{12}C(\gamma,pp)X$ from this experiment (open circles) and the calculation of Carrasco et al. [Ca94] (solid line histogram). Differential cross section is shown as a function of: proton kinetic energy (a), cosine of proton angle (b), cosine of opening angle (c) and phi difference (d).
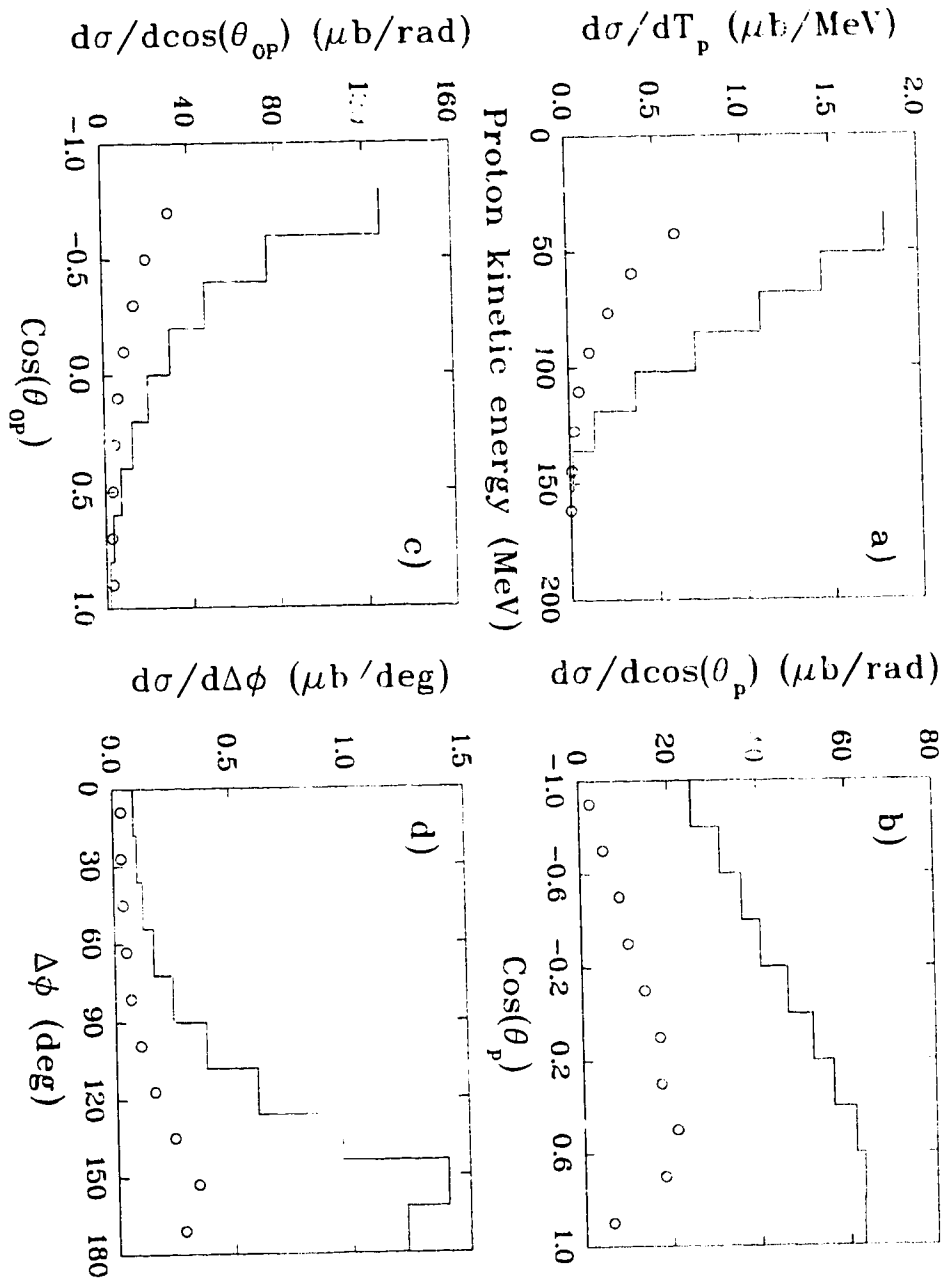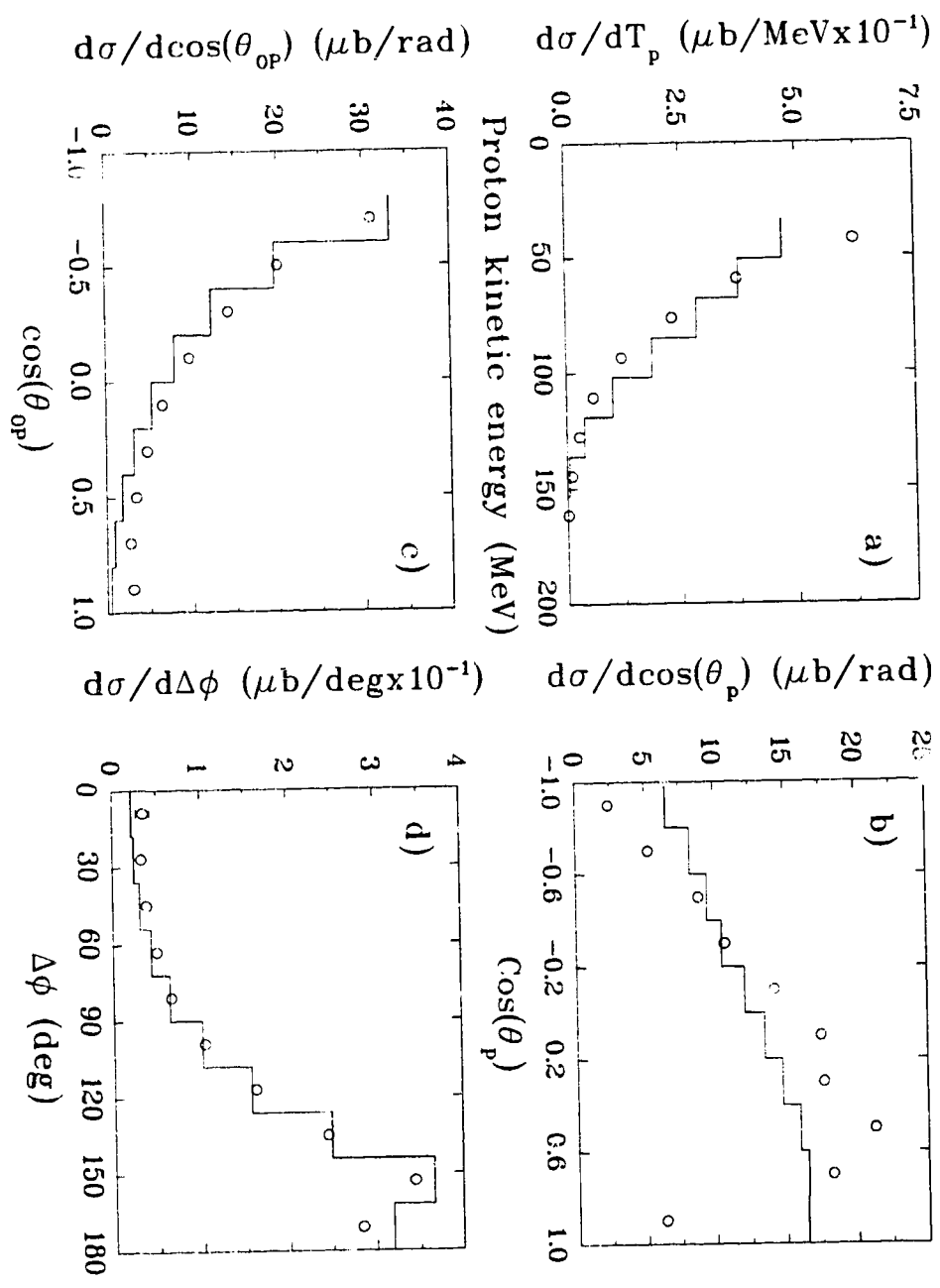
75

Figure 4.3: Comparison of differential cross section data for $^{12}C(\gamma,pp)X$ from this experiment (circles) and the calculation of Carrasco et al. [Car92] (solid line histogram) **normalized** to the same total cross section. The same four cross sections are displayed as in figure 4.2.

76

protons. Figure 4.4 compares the data to the calculated missing energy spectrum (solid line). It also shows the contributions to the cross section from each of the primary photon absorption processes: 1) 2N absorption (split into n-p and p-p channels), 2) 3N absorption and 3) pion production followed by reabsorption of the pion by 2 or 3 nucleons. Either directly or through rescattering, these three processes can lead to two protons being emitted with enough energy to be detected in SALAD. It is interesting to note that the shape of the missing energy spectrum is inconsistent with even a small contribution from direct p-p absorption. The other three mechanisms, n-p absorption, 3N absorption and pion production plus reabsorption, all reproduce the shape of the data distribution quite well.

Figure 4.5 shows the data compared to the calculation with the 2N absorption switched off (only 3N and pion production). Agreement is quite good for $d\sigma/dT_p$ and $d\sigma/dT_M$ but $d\sigma/dcos(\theta)$ is not well reproduced. In addition, it is not reasonable to abandon the 2N absorption mechanism when a large number of experiments clearly show the predominance of quasi-free p-n pairs in coplanar kinematics [Ga65, Sm67, Ar80, Ka87].

It is also evident from figure 4.4 that the shape of the $d\sigma/dT_M$ spectrum for n-p absorption also matches the shape of the data distribution. Figure 4.6 shows the same differential cross sections as in 4.5 but only n-p absorption events have been included in the calculation. Though the integrated cross section is still overpredicted by a factor of 2, the shape of the distributions is well reproduced. It appears the 2N absorption, 3N absorption and pion production mechanisms may be difficult to separate.

4.4 Identification of Primary Mechanisms

4.4.1 Neutron-Proton absorption

As discussed in section 1.3.1, three processes which are expected to contribute significantly to $^{12}C(\gamma,pp)X$ are:
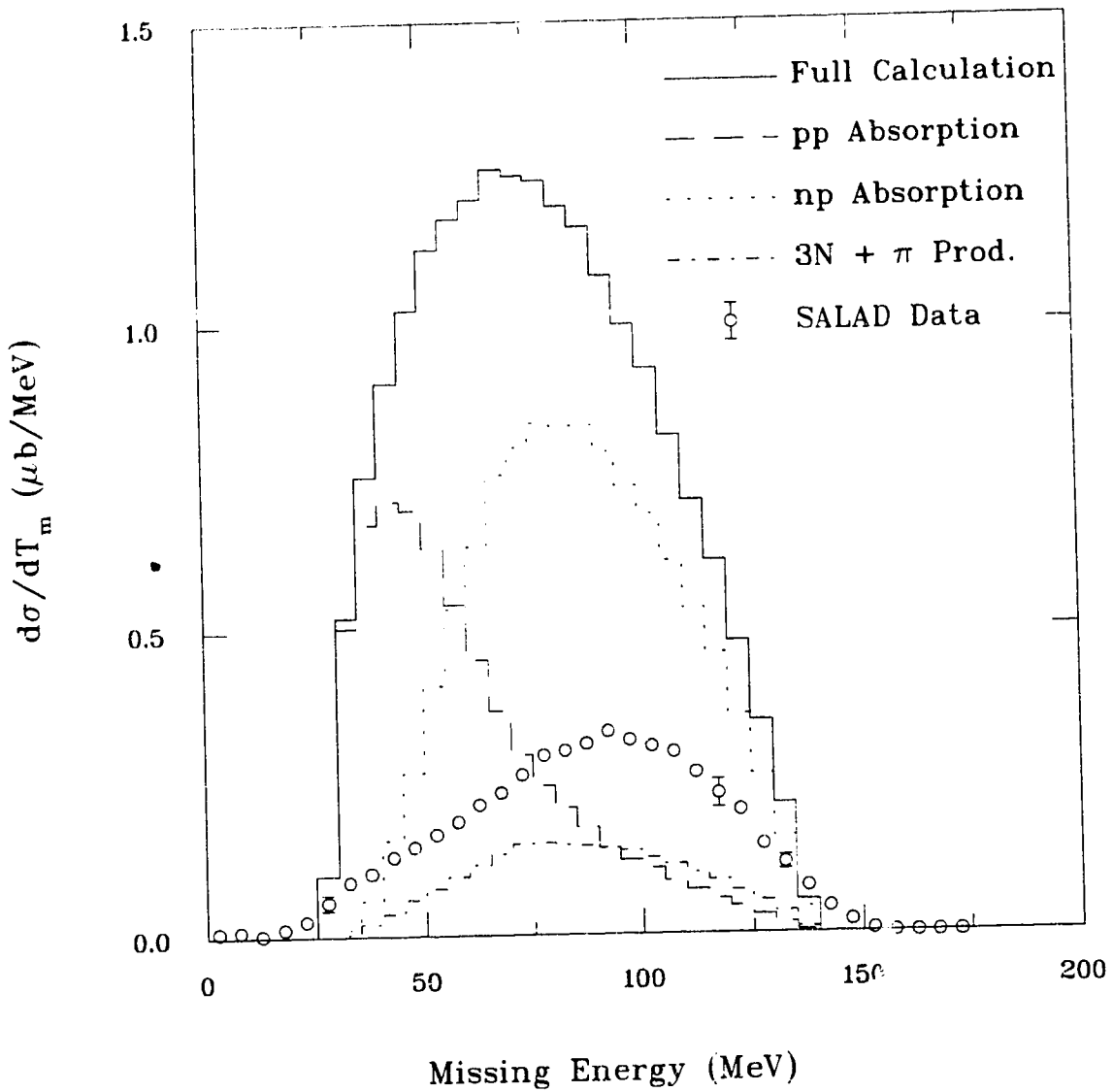
Figure 4.4: Comparison of differential cross section as a function of missing energy for data (circles), full calculation (solid line histogram), p-p absorption (dashed line histogram) and n-p absorption (dotted line histogram). The dot-dashed line histogram is the sum of the remaining mechanisms: quasi-free absorption on 3 nucleons and pion production followed by reabsorption of the pion by 2 or 3 nucleons.

78
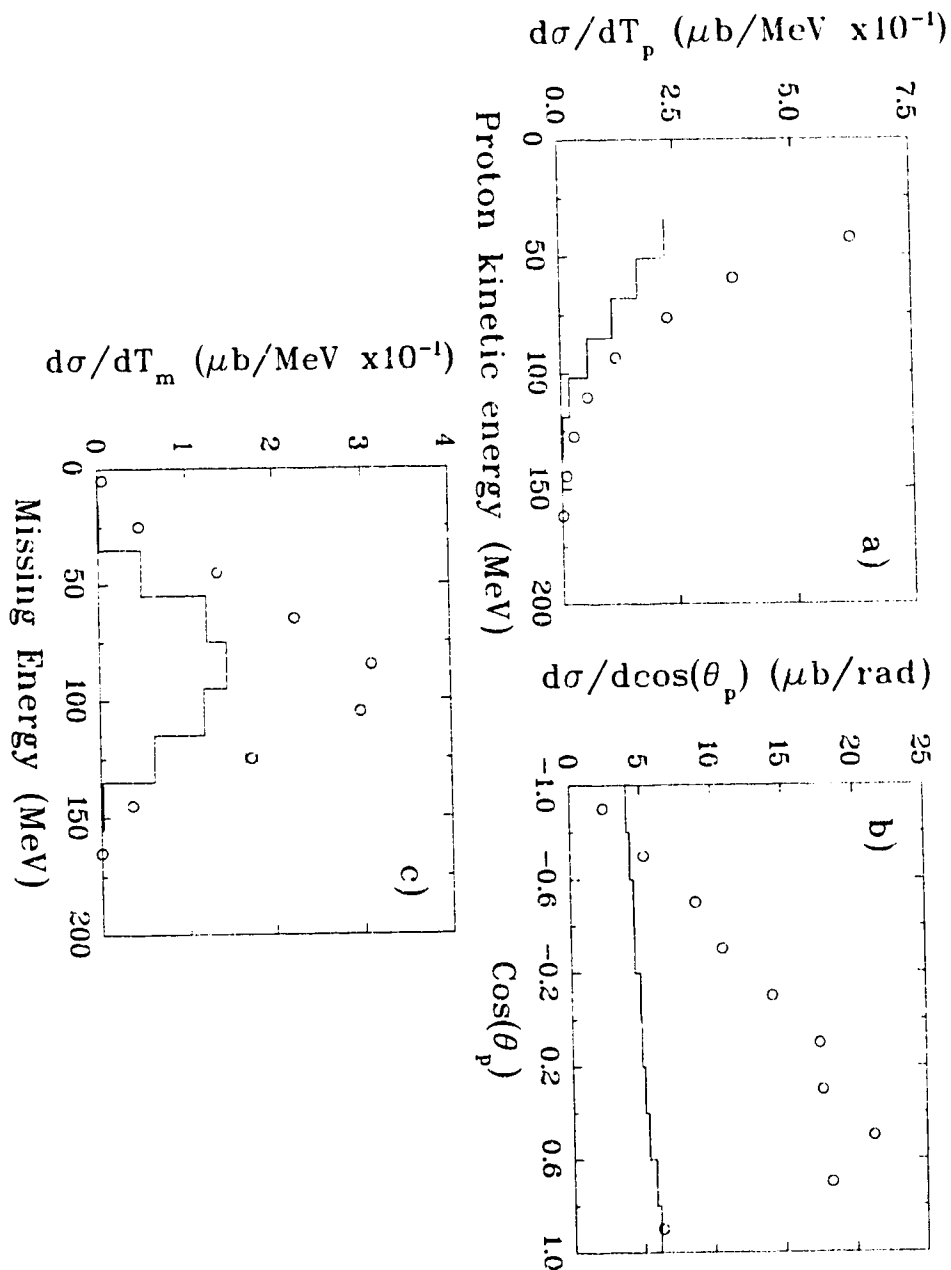
Figure 4.5: Differential cross section as a function of (a) Proton kinetic energy, (b) Cosine of proton angle and (c) Missing energy. The open circles are SALAD data and the solid line histogram shows the contribution to the calculation [Ca94] of three nucleon absorption and pion production mechanisms only.

79
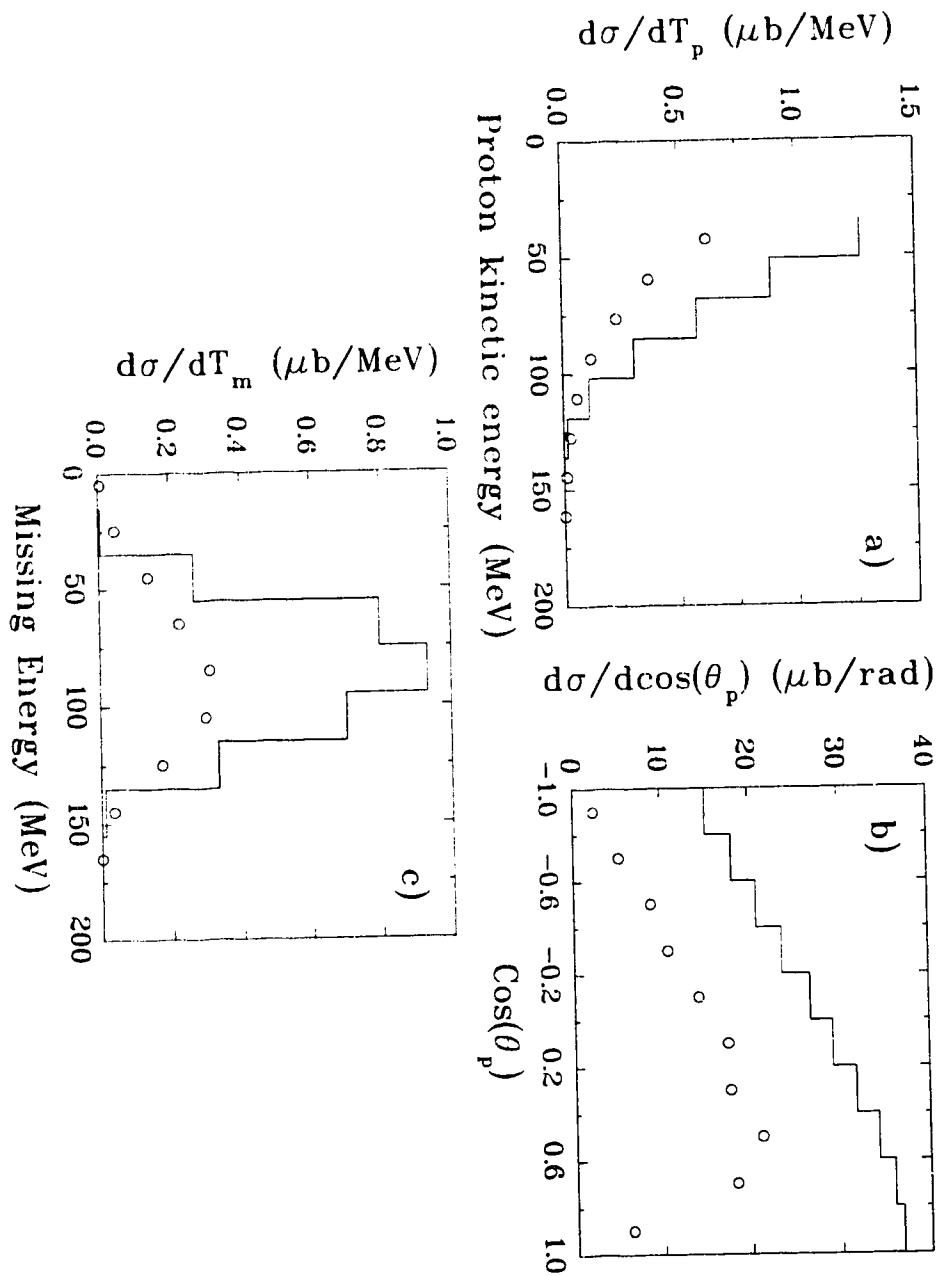
Figure 4.6: Differential cross section as a function of (a) Proton kinetic energy, (b) Cosine of proton angle and (c) Missing energy. The open circles are SALAD data and the solid line histogram shows the contribution to the calculation [Ca94] of the n-p absorption mechanism only.

80

1. A(γ ,np)X followed by nucleon-nucleon FSI,

2. Quadrupole absorption by p-p pairs,

3. Real pion production followed by π absorption on a 2N pair.

The first process is expected to be significant based on an earlier experiment [Ka87] which suggests that, in coplanar kinematics, absorption on n-p pairs is roughly ten times as likely as absorption on p-p pairs. Carrasco's calculation also assumes that the ratio of n-p to p-p absorption is approximately 9, averaged over all of phase space. In addition, an electron scattering experiment, [Ga92], establishes that the probability of nucleon rescattering in ^{12}C is $0.25 \pm .05$. Combining these two results, we expect two to three times as many events from

$$\gamma + 'pn' \to p_1 + n \qquad (4.4)$$

followed by,

$$n + p_2 \to n' + p_2', \qquad (4.5)$$

as from direct p-p absorption. If the momentum of the recoil nucleus is small, then $T_p^1 + T_n \simeq T_\gamma$, and even without detecting the neutron, the kinematics are overdetermined. For two body kinematics, we need only the photon energy and the angle, θ_p of the proton, to calculate T_p^{QD}, the expected proton energy for quasi-deuteron kinematics. By selecting the proton with the highest kinetic energy for T_p^{meas} the combinatoric background due to the 'other' proton, p_2', is reduced. The difference $(T_p^{QD} - T_p^{meas})$ is shown in figure 4.7. The calculation has been normalized to the same total cross section as the data.

Note that neither the data nor the calculation peak at $<\Delta T> = (T_p^{QD} - T_p^{meas}) = 0$, as might be expected. The centroid of the data distribution is $<\Delta T> = 18$ MeV, while centroid for the calculated peak is $<\Delta T> = 13$ MeV. Rescattering of the nucleons can alter the $<\Delta T>$ balance by reducing the observed proton kinetic energy. If this were the case, however approximately 75% of the primary protons would emerge unscathed and a peak at $<\Delta T> = 0$ would remain. A better explanation, perhaps, emerges
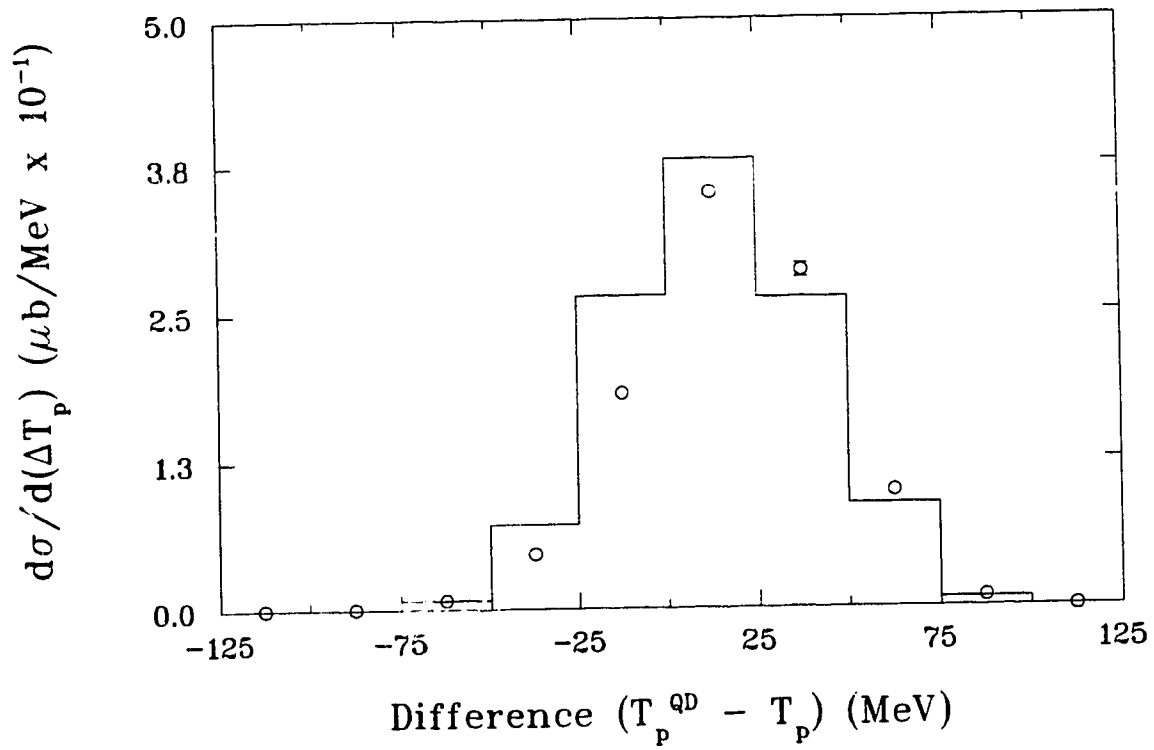
81

Figure 4.7: Comparison of differential cross section as a function of the difference between the greater measured proton energy and that expected from quasi-deuteron kinematics. Data are shown as open circles, the calculation as a solid line histogram.

when we examine the kinematics of the quasi-free n-p absorption more closely. The conservation of energy requires that,

$$E_\gamma = T_{p_1} + T_n + T_{Rec} + Q,$$ (4.6)

where T_{Rec}, the kinetic energy of the recoil nucleus (^{10}B) is negligible and $Q = 27.41$ MeV is the difference between final and initial masses. The Fermi energy of the absorbing nucleons does not appear since this internal degree of freedom is included in the overall mass of the nuclei. The problem arises with momentum conservation.

$$\mathbf{P}_\gamma = \mathbf{P}_{p_1} + \mathbf{P}_n + \mathbf{P}_{Rec}.$$ (4.7)

Though the kinetic energy of the recoil is small, its momentum may be large. In fact, for a quasi-free absorption, $\mathbf{P}_{Rec} = -\mathbf{P}_{12}^F$, the total Fermi momentum of the n-p pair which can be as large as 500 MeV/c in ^{12}C. Since the Fermi momentum, $\mathbf{P}_{12}^F$, is not known for a given event, it cannot be included in the calculation of T_p^{QD}. This omission may explain the shift from $<\Delta T> = 0$ in figure 4.7. This could easily be verified if the Fermi momentum of the nucleons could be set to zero in the calculation [Ca94]. In any case the agreement of data and theory is impressive, indicating that the distribution of Fermi momenta used in the calculation is realistic.

4.4.2 Proton-Proton Absorption

We would expect that quasi-free absorption on a p-p pair should produce a peak at a missing energy of 27 MeV which is the binding energy of two p-shell protons in ^{12}C. If we recall figure 4.4 , the calculation does indeed generate a p-p absorption peak (dashed line) but at 48 MeV. As in the previous n-p absorption, the Fermi motion of the absorbing nucleons may explain this shift in missing energy. Again, energy loss through rescattering cannot explain the shape of the p-p missing energy spectrum. The probability that neither proton rescatters is approximately $P = (1 - 0.25)^2 = 0.56$. This could reduce the missing energy for some events but 56% of p-p absorptions would suffer no rescattering and retain the proper missing energy.

Figure 4.4 also shows the predicted contribution from n-p absorption (dotted line) to $d\sigma/dT_m$. Remember that we require two protons in the final state, hence for n-p

absorption, at least one neutron is present. The share of kinetic energy taken away by this unseen neutron could explain why the n-p absorption distribution peaks 35 MeV higher in missing energy than the p-p absorption distribution. The calculation then suggests that the region of small missing energy, $T_M < 55$ MeV is dominated by quasi-free p-p absorption. The kinematic locus of a quasi-free p-p absorption might be apparent if we try to isolate the quasi-free kinematics.

Figure 4.8 shows the double differential cross section, $d^2\sigma/dT_p dcos(\theta_p)$. In figure 4.8 a), the coplanarity and low missing energy cuts should select mostly quasi-free p-p absorption events. Kinematic constraints on quasi-free absorption, limit the highest energy protons to small θ angles, while the low energy protons are at large angles. The expected locus would be a ridge running diagonally from the lower left to the top right corner of the plot. This ridge is evident in figure 4.8 a), though the missing energy cut removes many low energy protons, causing the ridge to increase in height from low to high proton energy. The sharp quasi two-body kinematic locus is also smeared by the Fermi momentum of the target nucleons within the carbon nucleus.

Figure 4.8 b) shows the data distribution for the same cuts. The statistical errors cannot be shown on the plot but they range from 10% to 30%. There is some evidence of the p-p absorption locus seen in the calculation. It is less distinct than in the calculated spectrum and it appears that other mechanisms are also present in this range of missing energy. Figure 4.9 shows the $d^2\sigma/dT_p dcos(\theta_p)$ distribution produced in the calculation by n-p absorption events only. The data distribution seems to combine features from both the n-p absorption shape (fig. 4.9) and the p-p absorption shape (fig. 4.8 a)), suggesting that both make important contributions to the $^{12}C(\gamma,pp)X$ cross section for this kinematic region. Though the calculation of Carrasco et al. is very good at isolating the contribution of a given mechanism, the final cross section it produces is an incoherent sum of all these mechanisms. If interference between the p-p and n-p absorption channels is important, this will be absent in Carrasco's calculated cross section.

To summarize, the shape of $d^2\sigma/dT_p dcos(\theta_p)$ for coplanar events with low missing energy, then suggests that p-p absorption is present but its contribution to the total

Figure 4.8: Double differential cross section, $d^2\sigma/dT_p dcos(\theta_p)$, for events with -25 < T_M < 55 MeV and coplanar protons, $\Delta\phi$ > 144°. Figure a) shows the calculation of Carrasco et al. and b) the data.
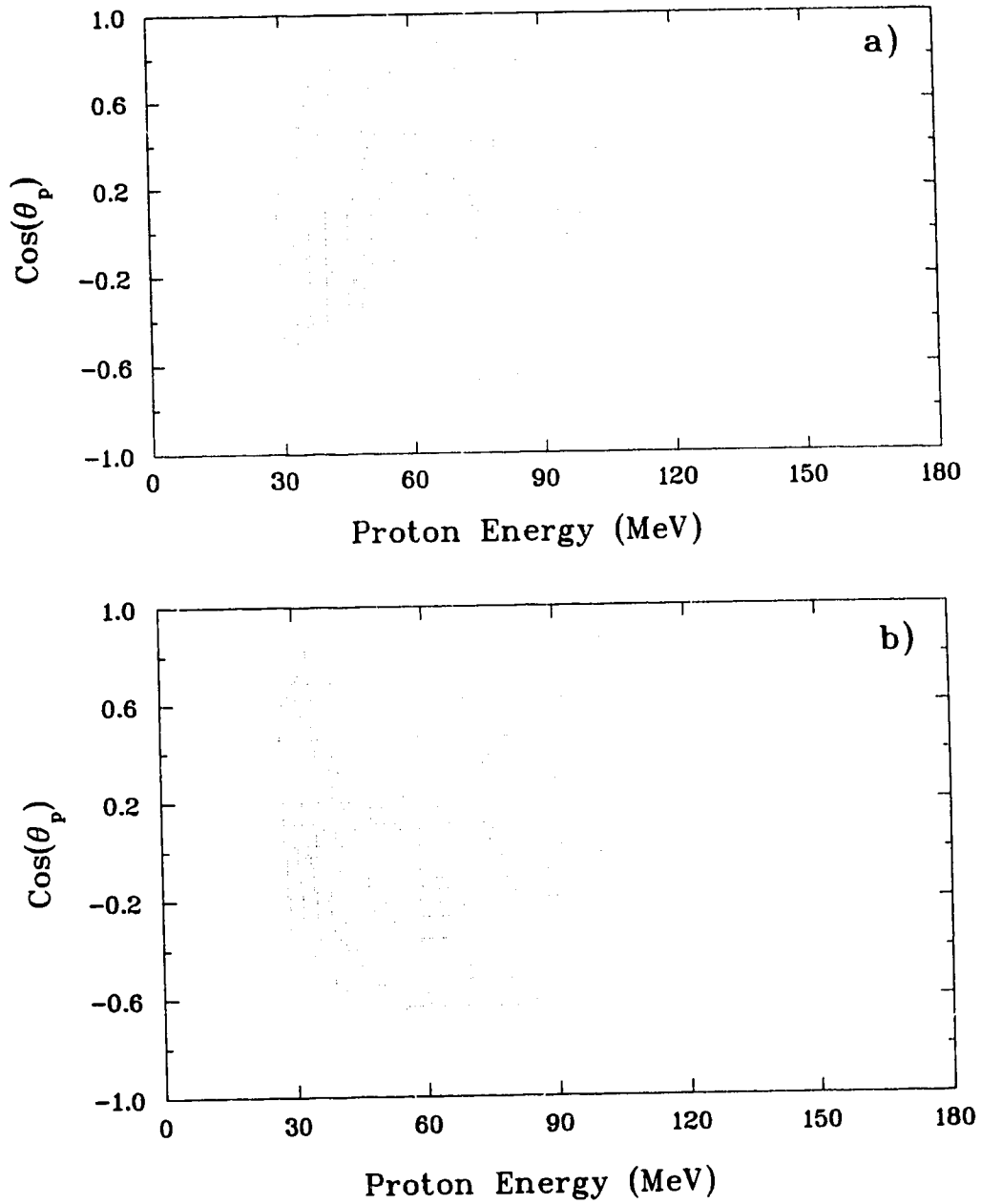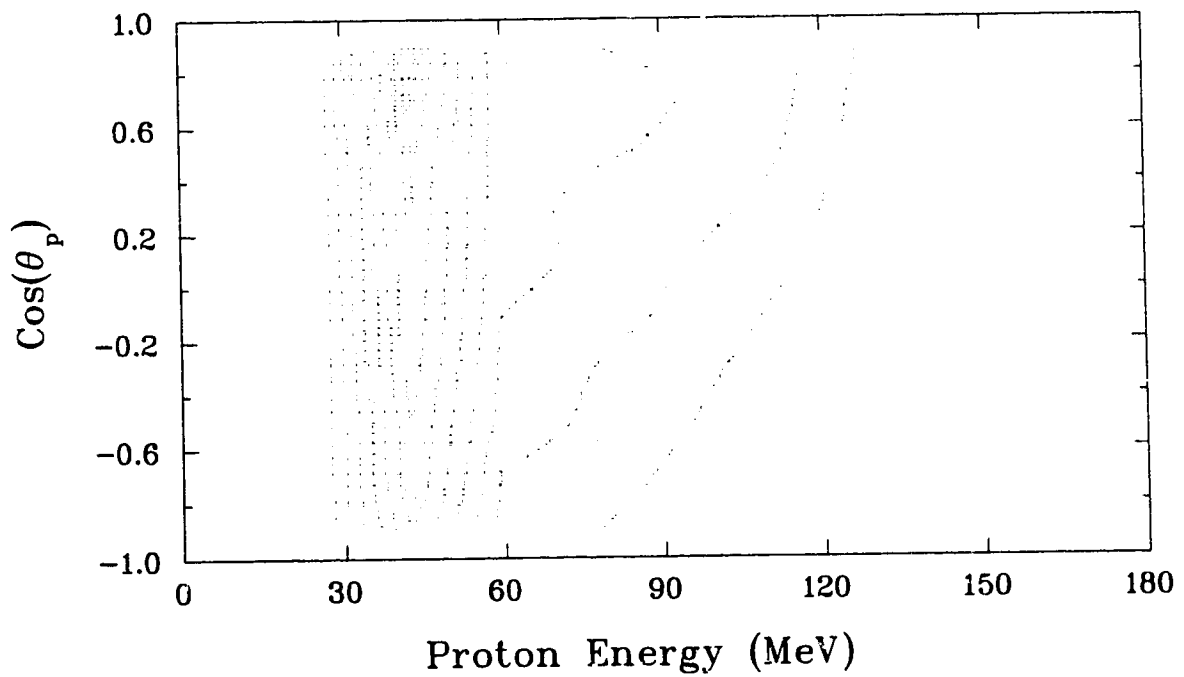
Figure 4.9: Double differential cross section, $d^2\sigma/dT_p dcos(\theta_p)$, for events with -25 $< T_M <$ 55 MeV and coplanar protons, $\Delta\phi >$ 144°. In the calculation of Carrasco et al., only events resulting from n-p photon absorption were considered.
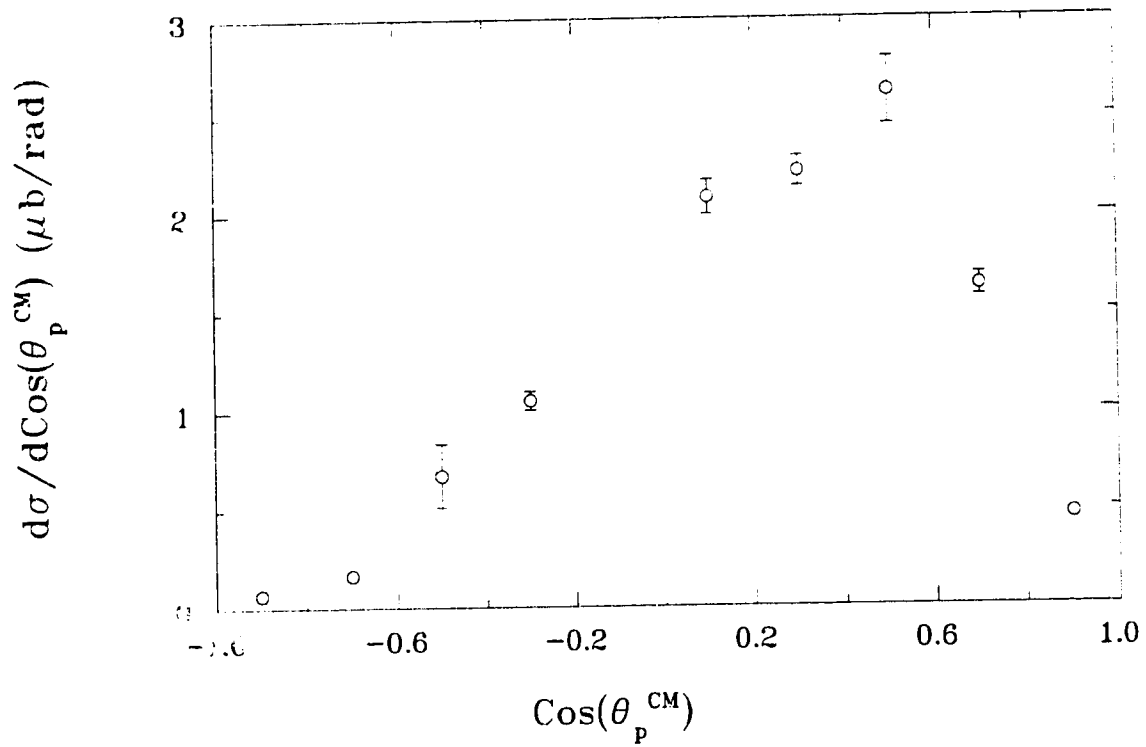
Figure 4.9: Differential cross section, $d\sigma/dcos(\theta_p^{CM})$, for events with $T_M < 55$ MeV and coplanar protons.

is smaller than predicted (see figure 4.4). If interference interference effects are not responsible for this suppression, then some other explanation must be found.

Finally we can integrate over proton energy to get the angular distribution, $d\sigma/dcos(\theta_p^{CM})$ for these coplanar events with low missing energy. Figure 4.10 shows the distribution in the p-p centre of mass frame, which, assuming an E2 absorption (see section 1.3.1), should show a quadrupole shape. A pure E2 distribution would show peaks at $Cos(\theta_p) = \pm\ 0.707$. No such peaks are evident in figure 4.10 but again, interference effects could greatly modify the proton angular distribution.

4.4.3 Pion photoproduction

The last primary photon absorption process to look for in the data is pion production.

$$\gamma + N \rightarrow \pi + N' \tag{4.8}$$

Producing the pion requires most of the 200 MeV photon energy and only 50 to 90 MeV of kinetic energy is left to be shared by the π and N'. To conserve momentum, the lighter pion receives most of the kinetic energy and the nucleon from the pion production vertex is rarely above the SALAD detector threshold. What does produce a signal in SALAD is the reabsorption of the π by two or more nucleons, which can lead to the emission of two high energy protons. If the two protons from a pion absorption are detected, the sum of their kinetic energies should equal a pion kinetic energy consistent with a pion of momentum equal to the sum of the proton momenta. It is safe to assume that the nucleon excited at the pion production vertex will be below threshold; then, only

$$\pi^+ + 'pn' \rightarrow p + p \quad and \quad \pi^\circ + 'pp' \rightarrow p + p \tag{4.9}$$

can produce two energetic protons to satisfy the trigger. As in 2N absorption, however, the unmeasured recoil momentum of the ^{9}Be nucleus,$\mathbf{P}_{Rec}$, complicates matters. If knew $\mathbf{P}_{Rec}$, we could calculate

$$M_{ex}^2 = (T_1 + T_2 + Q_{12})^2 - (\mathbf{P}_1 + \mathbf{P}_2 + \mathbf{P}_{Rec})^2, \tag{4.10}$$

which should equal the mass of the object exchanged between the primary photon absorption and the excitation of the two protons; assuming that this particle is on-shell. Figure 4.11 shows $d\sigma / dM_{ex}^2$ for both data and calculation. There is no evidence of a peak at the pion mass ($M_\pi^2 = 19.5 \times 10^3$ MeV^2/c^2), indicating either that the pion is off-shell or that the effect of $\mathbf{P}_{Rec}$ is large.

The calculation [Ca94] predicts that photon absorption via pion production should contribute only about 5% of the total ^{12}C(γ,pp)X cross section. Although the overall cross section varies slowly with photon energy, the pion production contribution grows quickly with increasing photon energy as the $\Delta(1232)$ resonance is excited. The Δ resonance peaks at 1232 MeV with a half width of 115 MeV. Therefore, a slight increase in photon energy would increase the importance of this process.
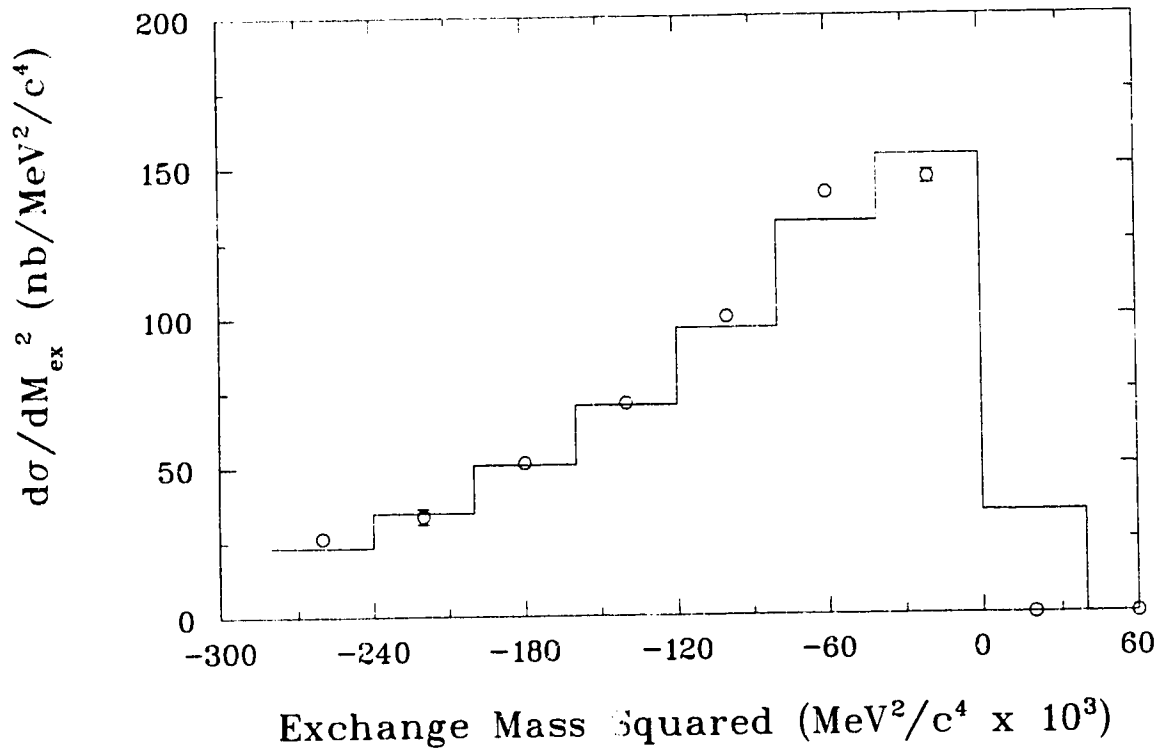
Figure 4.11: Differential cross section as a function of Exchange mass squared for SALAD data (open circles) and the calculation of Carrasco et al. [Ca94] (solid line histogram). Underflows have been suppressed and the calculation is normalized to the data.

4.4.4 Other Reaction Mechanisms

The failure of the previous three reaction mechanisms to account for all the features of the observed ^{12}C(γ,pp)X cross section suggests that more unusual mechanisms may be present. In section 1.3.1, some interesting mechanisms were suggested

Short range NN correlations are a modification to the short range nuclear potential. A recent paper by Boffi and Gia .ni: . [Bo91] suggests that the effect of such strong short range correlations would be to decrease the magnitude of the (γ,NN) cross section by a factor of up to 100, without significantly modifying the angular distribution. Even a much more modest decrease in the calculated cross section would greatly improve the agreement with the data.

Short range NN correlation effects are usually included by introducing a correlation function $f(r_{ij})$ which multiplies pairs of nucleon wave functions, $\Phi(i)$ $\Phi(j)$, in the Slater determinant which gives the total nuclear wave function. Carrasco et al. choose,

$$f(r_{ij}) = 1 - j_0(q_c r_{ij}),\qquad\qquad(4.11)$$

where r_{ij} is the separation of the two nucleons and q_c is an adjustable parameter taken to be equal to the mass of the ω meson ($q_c = 783$ MeV/c).

Simply varying q_c, modifies the nucleon-nucleon potential but ignores any effect on the Δ self energy or the π-N interaction. Still it should provide a useful test of the sensitivity of the calculation to short range N-N correlations. A large decrease in q_c, to 583 Mev/c, reduces the calculated ^{12}C(γ,pp)X cross section by only 3%. Hence it is unlikely that Carrasco's model can be brought into agreement with the present data by adjusting the strength of short range N-N correlations.

The onset of the Δ resonance in γN absorption occurs for photon energies of 180 MeV. The resonance peaks at $E_\gamma = 310$ MeV, hence the Δ resonance has little effect in the photon energy range of the present experiment, 187 MeV $< E_\gamma < 227$ MeV. Delta effects would be more easily seen in the ^{12}C(γ,pπ)X data which could also be extracted from the present SALAD data set.

The existence of three-body contributions to nuclear forces has not yet been clearly established. It is interesting that the shape of the missing energy distribution of

figure 4.4 is well described by the three-body photon absorption mechanism. Unfortunately the pion production plus reabsorption and the n-p absorption mechanisms pro... very similar missing energy distributions and any one of these processes on its own c... produce the data distribution. An explicit search for three-bo y correlations ... three fold coincidence data. A small number of $^{12}C(\gamma,3p)X$ events were f ... the present data but the lack of neutron detection excludes the majority of 3N ... s.

If quasi-free absorption on n-p and p-p pairs is the dominant mechanism for photon absorption then perhaps kinematic cuts could exclude them making subtler mechanisms more evident. By selecting events with large missing energy ($T_M > 55$ MeV) and non-coplanar protons ($\Delta\phi < 144°$), the quasi-free contribution should be greatly reduced. Figure 4.12 compares the data to the calculation for $d\sigma/dT_p$ and $d\sigma/d\cos(\theta_p)$. These are remarkably similar to the distributions of figure 4.2 where no cuts were applied. This supports the hypothesis that quasi-free absorption mechanisms are somehow suppressed and contribute only a small amount to the total $^{12}C(\gamma,pp)X$ cross section.
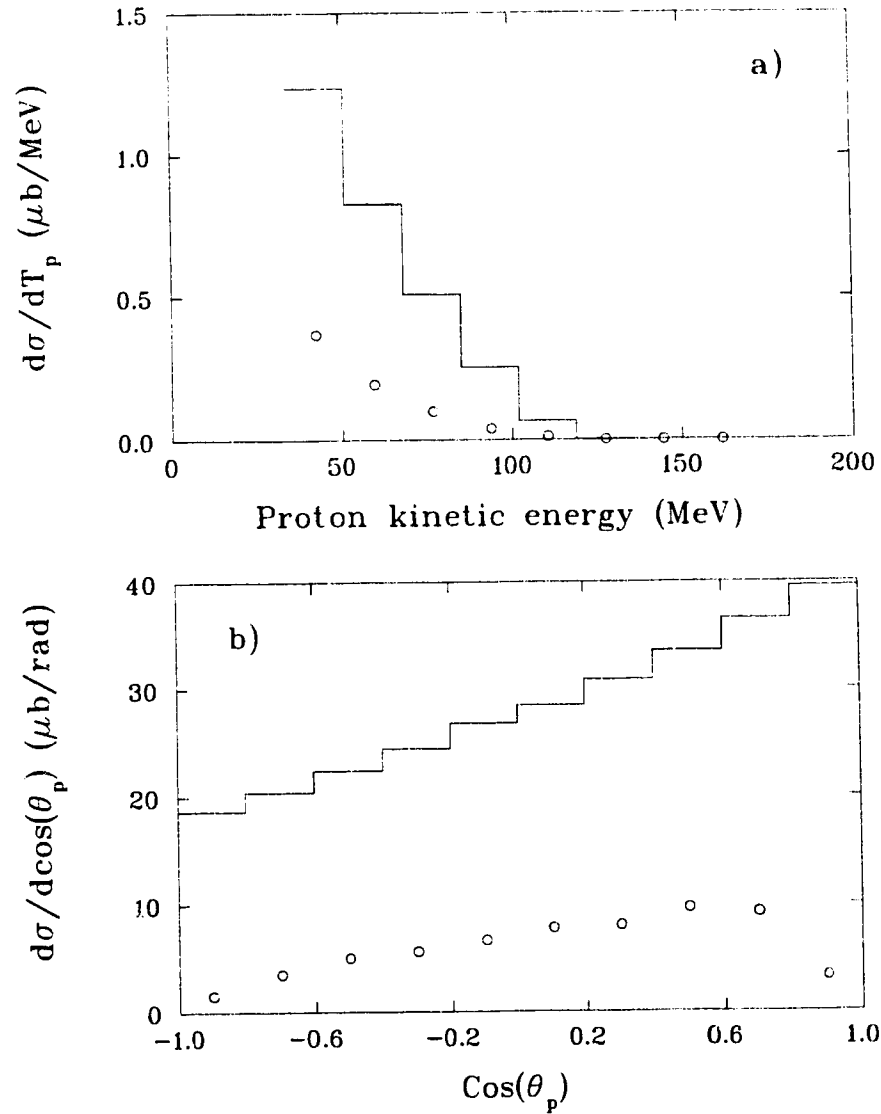
91

Figure 4.12: Comparison of differential cross section data and theory for $^{12}C(\gamma,pp)X$ excluding for events with $T_M > 55$ MeV and $\Delta\phi < 144°$. Data are shown as open circles, the calculation as a solid line histogram.

Chapter 5

Summary and Conclusions

The most striking disagreement between theory and experiment is in the size of the total cross section for $^{12}C(\gamma,pp)X$ for the range of photon energies 187 MeV $< E_\gamma < 227$ MeV. The calculation produces $\sigma_{tot} = 95.8 \pm 0.1$ μb, while the data give $\sigma_{tot} = 24.5 \pm 0.1$ μb; a difference in normalization of 3.9. There are many possible explanations for this disagreement.

In general, a simple model, such as the impulse approximation, overestimates the cross section. Refining the model invariably lowers the cross section as interference effects and final state interactions are added. The model of Carrasco et al. already represents a refinement of earlier intra-nuclear cascade methods but perhaps future refinements may decrease its predicted total cross section.

An attempt at explaining the difference in total cross section by adjusting the strength of short range NN correlations was unsuccessful. A crude attempt at modifying the calculation showed little sensitivity of the total cross section to short range correlations. Still, given the large effect predicted by Boffi and Giannini [Bo91], it may prove worthwhile to modify the calculation of Carrasco et al. [Ca94] to give a more exact treatment of NN correlation effects. The calculation would have to be extensively modified to include correlations in a consistent manner.

There is evidence in the comparisons of chapter 4 that the calculation has difficulty reproducing missing energy distributions. In figure 4.4, the calculated missing energy

distribution peaks 25 MeV lower than the data distribution. The sim;lest way to improve agreement is to strongly suppress the p-p absorption m   There is no conclusive evidence in the data of quasi-free p-p absorption. Th l   ic ...ns in figure 4.8 is faint at best and there is no evidence of a quad   m he angu. r distribution of quasi-free events. This absence of p-   on   e significant. Even though the calculation assumes that the primary   of p absorp   is nine times (isospin) more likely than p-p absorption, after th r cat ring requir l it the n-p case, n-p and p-p absorption make approximately equal contril tion   the alculated cross section (see figure 4.4).

One possible explanation for the absence of p-p absorption e its in t. data is that the cut on large opening angle events ($\theta_{op} > 150$ °) removes a large numb r of the p-p events. This cut is of course reproduced in the calculated cro.. ection but i s effect relies heavily on the accuracy of the proton angular distribution.

The suppression of p-p absorption hinders prospects of studying two-body, short range correlations. On the other hand it increases the chances of finding observable effects from three-body correlations or more unusual processes. The large acceptance of the SALAD detector makes it ideal for such triple coincidence measurements.

The strong peak corresponding to quasi-deuteron absorption in figure 4.7 suggests that n-p absorption is present. A cut on the quantity ($T_p^{QD} - T_p^{meas}$) could help to isolate the contribution of n-p absorption which must be quantified before subtler processes are investigated. Unfortunately, the shift in peak position suggests that the Fermi momentum of the absorbing nucleons strongly modifies the kinematics of the quasi-free absorption. An accurate distribution of Fermi momenta is crucial to any calculation of photon absorption at these energies. The Fermi momentum distribution used by Carrasco et al. is quite successful at reproducing the smearing of quasi-free absorption kinematics for photon and pion absorption.

The calculation of Carrasco et al. [Ca94] has proven very useful in understanding the $^{12}C(\gamma,pp)X$ data. The ease with which detector thresholds and acceptance can be applied to the calculation and its ability to easily separate contributions from different reaction mechanisms are particularly useful. To improve agreement with data, some

94

mechanism must be found to suppress the quasi-free p-p absorption contribution. Even then, the remaining contributions would produce too large a cross section. Once the magnitude of the $^{12}C(\gamma,pp)X$ cross section is reproduced, the calculation would then allow the investigation of three-body nuclear forces or the study of the Δ-N interaction.

The results of this experiment also suggest possible improvements to future experiments. The addition of neutron detection would be beneficial in two ways. First, overdetermined kinematics would reduce systematic errors in the analysis. Second, a search for three-body correlations would be greatly aided by including all possible 3N final states.

Finally, an increase in photon energy of 50 to 100 MeV would be beneficial. The sensitivity to detector thresholds would be reduced by placing more of the observable cross section above threshold. A change in energy would also, however, change the mechanisms involved. The contribution of resonant pion production would be greatly increased at higher photon energies.

Bibliography

[Al80]   N.A. Alekseev et al., Nuc. Instr. & Methods **177** (1980) 385.

[An90]   P.S. Anan'in et al., Sov. J. Nucl. Phys. **52** (1990) 205.

[Ar80]   J. Arends et al., Z. Phys. **A298** (1980) 103.

[Ar90]   H. Arenhövel and M. Sanzone, *Photodisintegration of the Deuteron, a Review*, MKPH-T-90-9, Mainz internal report, 1990.

[Ar72]   P.E. Argan el al., Phys. Rev. Lett. **29** (1972) 1191.

[Ba88]   G. Backenstoss et al., Phys. Rev. Lett. **61** (1988) 923.

[Ba89]   G. Backenstoss et al., Phys. Lett. **B222** (1989) 7.

[Bo89]   L. Boato and M.M. Giannini, J. Phys. **G15** (1989) 1605.

[Bo91]   S. Boffi and M.M. Giannini, Nuc. Phys. **A533** (1991) 441.

[Br75]   S. Brehin et al., Nuc. Instr. & Methods **123** (1975) 225.

[Ca86]   California Fine Wire Company, 338 South Fourth Street, Grover Beach, California - 93933.

[Ca87]   F. Carminati, *GEANT User's Guide*, CERN Program Library documentation, Q123, 1987.

[Cai92]   E.B. Cairns et al., Nuc. Instr. & Methods **A321** (1992) 109.

[Car92]   R.C. Carasco and E. Oset, Nuc. Phys. **A536** (1992) 445.

[Car92a] R.C. Carasco, E. Oset and L.L. Salcedo, Nuc. Phys. **A541** (1992) 585.

[Ca93] R.C. Carrasco, private communications.

[Ca94] R.C. Carasco, M.J. Vicente Vacas and E. Oset, Nuc. Phys. **A570** (1994) 701.

[Da89] L.O. Dallin, Proc. of the 1989 IEEE Particle Acc. Conf., 1 (1989).

[EK80] J.M. Eisenberg and D.S. Koltun, *Theory of Meson Interactions with Nuclei*, John Wiley and Sons, 1980.

[Em92] T. Emura et al., Phys. Lett. **B286** (1992) 229.

[Fa81] S. Fantoni et al., Phys. Rev. Lett. **B104** (1981) 89.

[FH74] H. Fraunfelder and E.M. Henley, *Subatomic Physics*, Prentice-Hall Inc, 1974. in particular section 12.6, p339-341.

[Ga65] J. Garvey et al., Nucl. Phys. **70** (1965) 241.

[Ga92] G. Garino et al., Phys. Rev. **C45** (1992) 45.

[Gl89] I.V. Glavanakov, Sov. J. Nucl. Phys. **49** (1989) 58.

[Go58] K. Gottfried, Nucl. Phys. **5** (1958) 557.

[Ja75] F. James, *CERN Program Library* documentation, W515, 1975.

[Jo84] Catalog of **Johnston Industrial Plastics**,1984, 4716 91 Ave, Edmonton, Alberta, tel (403) 465 0431

[Jo93] J. I. Johanssen, *Relativistic Treatment of Pion Photoproduction on Nuclei*, Ph.D. thesis, U. of Alberta, 1993.

[Ka87] M. Kanazawa et al., Phys. Rev. **C35** (1987) 35.

[Ko94] N.R. Kolb et al., Phys. Rev. **C49** (1994) 2586.

[La89] P.P. Langill, *A Large Acceptance Detector for Photonuclear Reactions*, M.Sc. thesis, U. of Alberta, 1989.

[Le51] J.S. Levinger. Phys. Rev. 84 (1951) 43.

[Lu91] *LUCID User's Guide*, Version 1.2, November 1991, Saskatchewan Accelerator Laboratory.

[Ma88] M. Matoba, *Radiation Detectors and Their Uses*, KEK Report 88-5.

[Me69] D.F. Measday and C. Richard-Serre, *Loss of Protons by Nuclear Interactions in Various Materials*, CERN Report 69-17, June 1969.

[Na81] A. Nadasen et al., Phys. Rev. C23 (1981) 1023.

[Os87] E. Oset and L.L. Salcedo, Nucl. Phys. A468 (1987) 631.

[Ph92] L.D. Pham et al., Phys. Rev. C46 (1992) 621.

[Qu93] M.A.F. Quraan. *Coincidence Measurements of Relative Cross Sections for* $D(\gamma, pp\pi^-)$ *in the Region of the* Δ *Resonance*, M.Sc. thesis, U. of Alberta, 1993.

[Sa88] L.L. Salcedo et al., Nuc. Phys. A484 (1988) 557.

[Sc80] J.P. Schiffer et al., Nuc. Phys. A335 (1980) 339.

[Sm67] I.L. Smith et al., Nuc. Phys. B1 (1967) 483.

[Vo93] J.M. Vogt et al., Nuc. Instr. & Methods A324 (1993) 198.

[We90] H.J. Weyer, Phys. Rep. 195 (1990) 295.

[Wr5°' G.T. Wright, Phys. Rev. 91 (1953) 1282.

Glossary of Abbreviations and Acronyms

The following commonly used acronyms and abbreviations appear in this thesis.

ADC: Analog to Digital Converter

CERN: Centre Europeen pour la Recherche Nucleaire (European Centre for Nuclear Research), Geneva.

EROS: Electron Ring of Saskatchewan at SAL

dE/dx: Rate of energy loss (stopping power) of a particle (MeV/cm).

FSI: Final state interactions.

GEANT: A group of standard subroutines from the CERN Library for constructing Monte Carlo simulations of nuclear/particle physics detectors.

GENBOD: CERN library routine for the generation of N-body phase space distributions.

GHEISHA: a subset of the GEANT program library which models hadronic interactions.

INC: Intra-Nuclear Cascade model of nuclear reactions.

LDA: Local Density Approximation.

LUCID: Data acquisition and analysis system written at SAL.

OPE: One-Pion Exchange potential. A nucleon-nucleon potential derived from from field theory of pions.

PID: Particle Identification variable. A linearization of stopping power information.

PMT: Photomultiplier Tube

SAL: Saskatchewan Accelerator Laboratory, Saskatoon, Saskatchewan.

SALAD: Saskatchewan-Alberta Large Acceptance Detector.

TDC: Time to Digital Converter

TRIUMF: Tri-University Meson Facility, Vancouver, British Columbia.